LBNL-41810

ERNEST ORLANDO LAWRENCE BERKELEY NATIONAL LABORATORY

Advanced Far Infrared Blocked Impurity Band Detectors Based on Germanium Liquid Phase Epitaxy

Christopher S. Olsen

Engineering Division

May 1998

Ph.D. Thesis

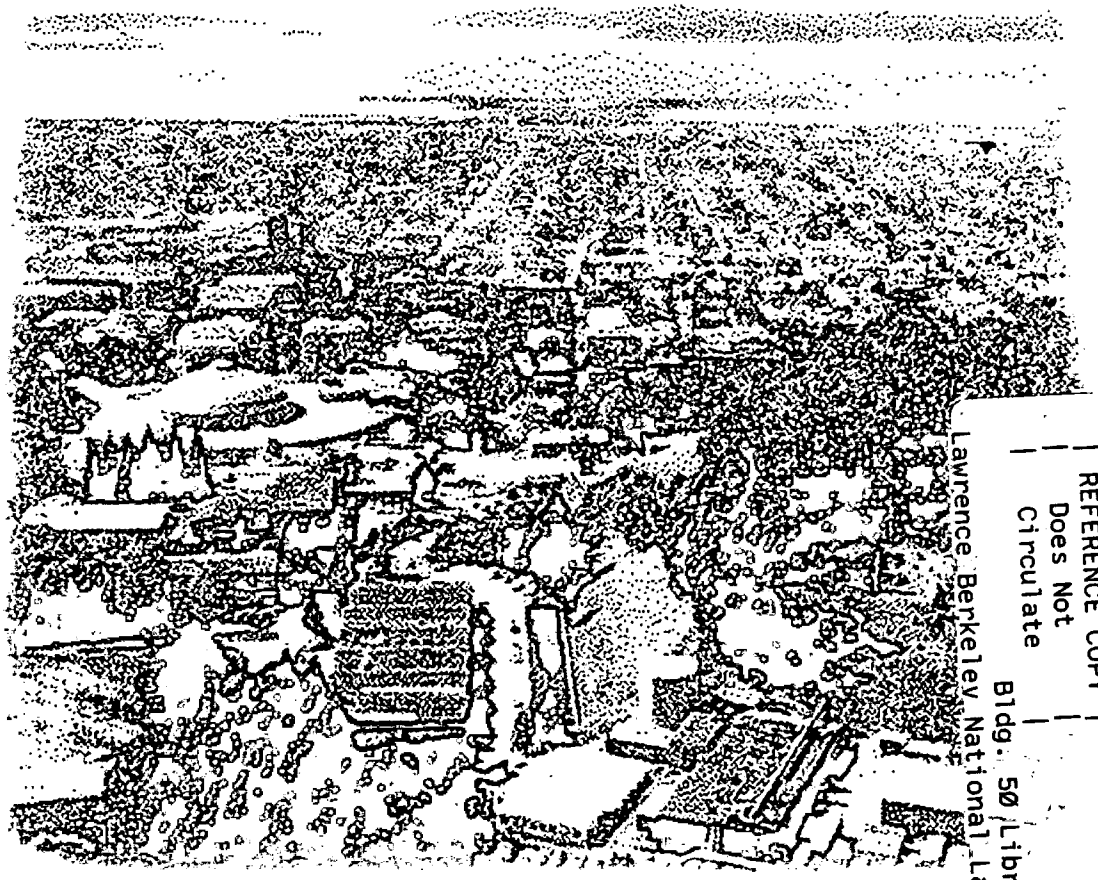

REFERENCE COPY
Does Not
Circulate

Bldg. 50 Library - Ref.
Lawrence Berkeley National Laboratory

Copy 1

LBNL-41810

DISCLAIMER

This document was prepared as an account of work sponsored by the United States Government. While this document is believed to contain correct information, neither the United States Government nor any agency thereof, nor the Regents of the University of California, nor any of their employees, makes any warranty, express or implied, or assumes any legal responsibility for the accuracy, completeness, or usefulness of any information, apparatus, product, or process disclosed, or represents that its use would not infringe privately owned rights. Reference herein to any specific commercial product, process, or service by its trade name, trademark, manufacturer, or otherwise, does not necessarily constitute or imply its endorsement, recommendation, or favoring by the United States Government or any agency thereof, or the Regents of the University of California. The views and opinions of authors expressed herein do not necessarily state or reflect those of the United States Government or any agency thereof or the Regents of the University of California.

LBNL-41810

Advanced Far Infrared Blocked Impurity Band Detectors based on Germanium Liquid Phase Epitaxy

Christopher Sean Olsen

Engineering Division
Ernest Orlando Lawrence Berkeley National Laboratory
1 Cyclotron Road
Berkeley, California 94720

and

Materials Science and Mineral Engineering Department
University of California
Berkeley, California 94720

Ph.D. Thesis

May 1998

This work was supported by U.S. NASA Contract W17605 and A59513CBVC through interagency agreement with the U.S. Department of Energy under Contract No. DE-AC03-76SF00098.

Advanced Far Infrared Blocked Impurity Band Detectors based on Germanium Liquid Phase Epitaxy

by

Christopher Sean Olsen

B. S. (University of California, Los Angeles) 1991
M. S. (University of California, Berkeley) 1994

A dissertation submitted in partial satisfaction of the

requirements for the degree of

Doctor of Philosophy

in

Engineering-Materials Science & Mineral Engineering

in the

GRADUATE DIVISION

of the

UNIVERSITY OF CALIFORNIA, BERKELEY

Committee in charge:
Professor Eugene E. Haller
Professor Daryl Chrzan
Professor Paul McEuen

Spring 1998

Abstract

Advanced Far Infrared Blocked Impurity Band Detectors based on

Germanium Liquid Phase Epitaxy

by

Christopher Sean Olsen

Doctor of Philosophy in Engineering - Materials Science & Mineral Engineering

University of California, Berkeley

Professor Eugene E. Haller

Germanium Blocked Impurity Band (BIB) detectors have been fabricated using Liquid Phase Epitaxy (LPE) to grow the high purity blocking layer and the heavily doped infrared absorbing layer, the major components of these devices. To achieve the necessary properties of both epilayers, very low structural and electrical defect concentrations are required. We have developed a high purity LPE process which can be used for the growth of high purity as well as purely doped Ge epilayers. We chose the low melting point, high purity metal lead (Pb) which has a negligible solubility in solid Ge and does not form electronic levels in the band gap of Ge. We have identified the residual impurities Bi, P, and Sb in the Ge epilayers and have determined that the Pb solvent is the source. We have purified the Pb by approximately one order of magnitude using distillation. The highest purity Ge epilayers were grown with net-electrical impurity concentrations of $5x10^{13}$ cm^{-3}. BIB detectors fabricated with just the purely doped absorbing layer grown on high purity substrates with LPE have shown responsivities as high as 1 A/W. The detectors exhibit an extended wavelength cutoff when compared to standard Ge:Ga photoconductors (165 μm

vs. 120 μm) and show the expected asymmetric current-voltage characteristic. Optimizing of doping and layer thickness have lead to improvements in absolute responsivity, Noise Equivalent Power (NEP), and dark current.

Acknowledgement

I would like to dedicate this dissertation to my wife for all her love and support through the trials of the Ph.D. program. I would like to especially thank Prof. Nancy Haegel for the experiences that brought me to Berkeley. I am especially grateful to my advisor Prof. Eugene Haller for his support and advice in so many ways. I would also like to thank Prof. Daryl Chrzan and Prof. Paul McEuen for spending the time to critique my dissertation.

I am grateful to have had such a powerful experience with other graduate students here at Berkeley. Kristin Duxstad, Dawnelle Wynne, Bill Knowlton and Oscar Dubon have been good friends and peers to interact with intellectually. I am indebted to Jeff Beeman for his support throughout the years, helpful advice on my projects, and stimulating discussions in the lab. I would also like to acknowledge Bill Hansen, who always had an idea of how to solve challenging problems. I would like to thank David Hom for his help, wit, and sarcasm.

I would like to thank my family for their influence in my life. I am grateful for my friends and this community who have raised me emotionally and intellectually.

This work was supported by US NASA Contract W17605 and A59513CBVC through interagency agreement with the US Department of Energy Contract DE-AC03-76SF00098.

Table of Contents

1. Introduction 1
    1.1 Motivation for Far Infrared Detector Development 1
    1.2 Photoconductors 3
        1.2.1 Principles of Operation 3
        1.2.2 Figures of Merit 6
        1.2.3 Present Technology 12
    1.3 Blocked Impurity Band Detectors 14
        1.3.1 Blocked Impurity Band Detectors: Structure & Operation 14
        1.3.2 State of the Art of Silicon Blocked Impurity Band Detectors 18
        1.3.3 Ge Blocked Impurity Band Detectors 21
        1.3.4 Review of Past Ge BIB Detector Efforts 26

2. Germanium Liquid Phase Epitaxy 28
    2.1 Introduction 28
        2.1.1 Background 28
        2.1.2 LPE Growth Processes 30
        2.1.3 Convection in the Solvent 36
        2.1.4 Segregation of Impurities 38
        2.1.5 Tipping Method 40
    2.2 Review of Ge LPE Research 42
    2.3 Growth Procedures 43
    2.4 Epilayer Characterization 48

3. Epitaxial Growth Experiments with Pb solvent 50
    3.1 Structural Properties of Ge epilayers 50
    3.2 Electrical and Optical Properties 52
    3.3 Pb Purification for Ge LPE growth 61
        3.3.1 Vaporization and Oxidation 61
        3.3.2 Zone Refining 62
        3.3.3 Distillation 65
    3.4 Impurity Segregation Study 69
    3.5 Master Doping Alloy 70

4. BIB Detector Fabrication and Characterization 72
    4.1 Fabrication 72
    4.2 Characterization 73
    4.3 Performance 73
    4.4 Optimization 83
    4.5 Future Studies 87
5. Summary and Conclusions 87

6. Appendices 89
Appendix A: Hall effect 89
Appendix B: Fourier Transform Far Infrared Spectroscopy..... 93
Appendix C: Photothermal Ionization Spectroscopy 96
Appendix D: Epilayer Growth Results 98
Appendix E: Spectral Response and Responsivity Measurements..... 107
Appendix F: N-type Alloy Contact..... 109
Appendix G: Electric Field in a BIB Detector 111
7. References 113

1. Introduction
1.1 Motivation for Far Infrared Detector Development

For astronomers and astrophysicists the far infrared (IR) spectral range from 50 to 400 cm^{-1} holds a great wealth of information about many aspects of the universe. In this range one can observe characteristic IR radiation emitted by excited atomic or molecular species which offers information about the radiating species (e.g. molecular structure) as well as the temperature and density of these species. IR data can provide insight into the mechanisms of star formation, physics of interstellar media, nature of the galactic center, early evolution of galaxies, and properties of primitive solar system material.(Pilbratt 1994) To view and image distant objects emitting in the infrared, telescopes must be fitted with special infrared detectors. Imaging of large objects in the universe is achieved by scanning a simple detector over the area of interest or more efficiently by using a two dimensional (2D) array of detectors which can record a 2D image.

The IR sky is much brighter than the visible sky, but because of severe absorption in the atmosphere the IR radiation does not reach the ground. Since the earth and atmosphere are warm (300K), they emit in this same IR range. As the earth's atmosphere completely absorbs all the radiation around 100 cm^{-1} (12 meV), IR telescopes must either be positioned at very high altitudes, on airplanes, or launched as satellites into space to allow efficient IR detection. Some telescopes such as the Keck I & II on Mauna Kea in Hawaii are land-based at an altitude close to 14,000 feet, where some IR penetrates the residual atmosphere. By putting a telescope into an earth orbit, the atmosphere can be avoided entirely. The Infrared Astronomical Satellite (IRAS) was the first such IR telescope in space. It was launched in 1983 and it lead to the discovery of thousands of

new infrared sources.(Rieke, et al. 1986) The quality of the data collected by IRAS was partly limited by the performance of the IR detectors. The discoveries, however, were spectacular and have encouraged further space telescope missions. The Infrared Space Observatory (ISO), launched in November of 1996 by the European Space Agency (ESA), has been the most recent mission to observe the IR universe in more detail. ISO carries a Long Wavelength Spectrometer (LWS) that is sensitive from 43 to 197 μm. This whole spectral range is covered with 3 types of Ge photoconductive detectors, Ge:Be, Ge:Ga, and stressed Ge:Ga. ESA is also planning the Far Infrared and Submillimetre Space Telescope (FIRST) to operate from 85 to 600 μm to be launched in 2006. NASA is planning the launch of the Space Infrared Telescope Facility (SIRTF) in December of 2001. The Multiband Imaging Photometer for SIRTF project (MIPS) has been supplied with Ge:Ga photoconductors by our research group. SIRTF has three arrays for detecting IR signals at 24, 70, and 160 μm. For 70 μm detection, a 32x32 Ge:Ga arrays have been chosen, and at 160 μm, a 2x20 stressed Ge:Ga detector array will be used. All of these space missions require that IR detectors are low noise and have very low dark currents, because of the very low photon background in space. For the Stratospheric Observatory for Infrared Astronomy (SOFIA) a second generation airplane based telescope, IR backgrounds will be relatively high and detector noise and dark current requirements will not be as stringent as for low background missions. These past and future space telescope missions have strongly stimulated research into improving far infrared detectors.

1.2 Photoconductors

1.2.1 Principles of Operation

One class of semiconductor IR detectors operates in the photoconductive mode. These devices absorb photons which in turn produce either phonons or free charge carriers (electrons or holes). These carriers can then be detected by measuring the change in conductivity they induce in the material. There exist two types of photoconductors: Intrinsic photoconductors which are undoped, and extrinsic photoconductors which are doped with a specific impurity. Intrinsic photoconductors operate by the excitation of an electron from the valence band to the conduction band, leaving behind a mobile hole in the valence band. To make this transition, the electron must receive enough energy to get excited across the band gap, therefore only photons with energies greater than the band gap of the semiconductor are detected. Most semiconductor band gap energies range from 0.3 eV (near IR, example: InSb, $Hg_xCd_{1-x}Te$) to 3 eV (blue light, example: ZnSe, GaN). $Hg_xCd_{1-x}Te$ detectors can operate from the near to the mid infrared (1.57 to 0.073 eV) depending on the composition of the alloy (x). The low energy limit for $Hg_xCd_{1-x}Te$ intrinsic photoconductors and photodiodes is due to difficulty controlling the alloy composition at the microscopic level. Therefore, detection in the far IR cannot be obtained with intrinsic photoconductors.

Extrinsic photoconductors function through the photoexcitation of an electron (hole) bound at a donor (acceptor) into the conduction (valence) band. The shallow or "hydrogenic" impurity ionization energy, E, is the energy difference between the 1s-like ground state of the impurity and the band edge. The ionization energy of shallow

impurities is much smaller than the band gap, thus such impurity ionization can be used to detect photons of much longer wavelengths, λ. The relationships between E, λ, and ν are given in equation 1.1.

$$\lambda(\mu m) = \frac{10^4}{\nu(cm^{-1})} = \frac{1.24}{E(eV)} \tag{1.1}$$

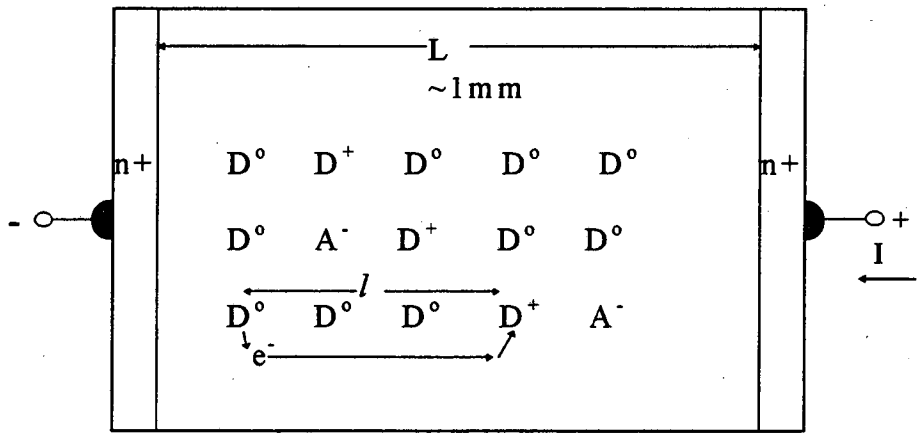

Fig. 1.1 Schematic of extrinsic photoconductor

Since shallow impurity ionization energies are typically in the tens of meV range, very low operating temperatures must be used to provide frozen-out neutral donors (acceptors) for photoionization. After a neutral donor, D^o, is photoionized, the free electron moves in the conduction band under the applied electric field. The moving electron generates a displacement current I in the external circuit. The contribution of the electron to the total signal current will depend on the distance l it travels in the photoconductor of width L before it returns to another ionized donor, shown in Fig 1.1. The fraction traveled l/L is called the photoconductive (PC) gain G. G can vary from values much smaller than unity to way above one. In the latter case, Ohmic contacts must reinject the charge carrier

leaving the photoconductive volume. The ionized donor will eventually be neutralized by recombination with another electron.

The concentration of ionized donors at low temperatures will be equal to the concentration of acceptors $N_{D^+} = N_{A^-}$, due to compensation. A high concentration of ionized donors will lead to small values of l causing the free electron contribution to the conductivity to be small. Indeed the lifetime of a photoionized electron is proportional to $1/N_{D^+} \approx 1/N_{A^-}$.

$$\tau = \frac{1}{\sigma_c v N_{A^-}} \tag{1.2}$$

The free carrier velocity v and the capture cross section σ_c determine the rate of recombination. The photocurrent is measured with a low noise, electronic amplifier circuit. Degenerately doped (Ohmic) contacts are needed to form a small energy barrier for electrons to enter and exit the device at low temperatures.

Photoconductivity is a dynamic process of carriers being generated and recombining at charged impurity sites. The rate equation for the free carrier concentration n is

$$\frac{dn}{dt} = g - \frac{n}{\tau} \tag{1.3}$$

where g is the generation rate due to an external photon source, t is time, and τ is the carrier lifetime. The solution of equation 1.3 for a step increase (decrease) Δn_{rise} of the generation rate Δg is

$$\Delta n_{rise} = \Delta g\,[1 - \tau \exp(-t/\tau)] \tag{1.4}$$

$$\Delta n_{decay} = \Delta g\, \tau \exp(-t/\tau) \tag{1.5}$$

an exponential rise (decay) of the photosignal (Figure 1.2) which strongly depends on the lifetime τ.

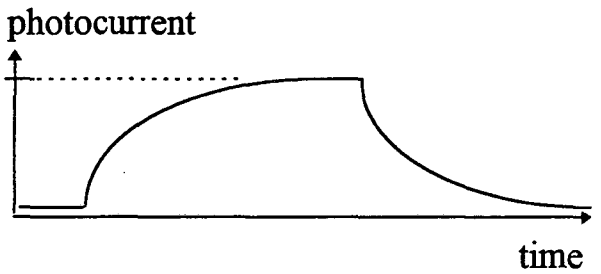

Fig. 1.2. Response of photoconductor to a square pulse of external radiation.

In the following section, specific parameters and figures of merit needed to quantitatively characterize photoconductors will be discussed.

1.2.2 Figures of Merit

Several figures of merit are required to fully characterize a photoconductor. They include responsivity, responsive quantum efficiency, spectral response, noise equivalent power (NEP), and detective quantum efficiency.

To develop a model for photoconductive response, the PC gain is now re-expressed as the ratio of the free carrier lifetime, τ, over the transit time, t, shown in equation 1.6. The transit time is the drift velocity, v_{drift}, divided by the device length, L. The drift velocity is the mobility, μ, times the applied bias voltage V divided by L. We now can write:

$$G = \frac{\tau}{t} = \tau\mu\frac{V}{L^2} \tag{1.6}$$

The PC gain must be determined indirectly with measurable parameters.

Responsivity (R) is the ratio of the photoconductive signal current and the incident photon power, measured in Amperes per Watt. A high responsivity is desirable to overcome electronic noise, especially when detecting small signals. The responsivity, R, is affected by many parameters and it strongly depends on wavelength. The responsivity is given by the following equation.

$$R = \frac{e}{h\nu} G\eta \tag{1.7}$$

In the above equation, e is the electron charge, h is Planck's constant, ν is the frequency of incident photons and η is the responsive quantum efficiency. Using the equation 1.2 and 1.6, the responsivity can be rewritten

$$R = \frac{eV}{h\nu L^2} \eta\tau\mu = \frac{eV}{h\nu L^2} \frac{1}{\sigma_c \nu (N_A^- + n)} \eta\mu \tag{1.8}$$

For in-depth treatments of responsivity, the reader is referred to review articles by Bratt 1977, Haegel 1983, and Haller 1985.

Responsive quantum efficiency η is defined as the ratio of the flux of photons absorbed, J_a, to the flux of photons incident, J, upon the device and is given by the following equation,

$$\eta = \frac{J_a}{J} = \left\{ \frac{(1-r)[1-\exp(-\alpha L)]}{1-r[\exp(-\alpha L)]} \right\} \tag{1.9}$$

where r is reflectivity and α is the linear absorption coefficient of the material. The linear absorption coefficient is equal to the dopant ionization cross section σ times the doping concentration N_D. The ionization cross section for shallow dopants in Ge is approximately 10^{-14} cm^2.(Wang, et al. 1986)

The reflectivity (r) is given by the following equation:

$$r = \frac{(n_o - n_1)^2}{(n_o + n_1)^2} \tag{1.10}$$

where n_o is the index of refraction of the medium that the light is traveling from and n_1 is the index of refraction of the medium that the light is traveling into. For a photon traveling from vacuum (n = 1) into Ge (n = 4), the reflectivity at one interface is 9/25 or 0.36. The reflectivity at the front surface can be minimized by applying anti-reflection coatings and back surfaces can be implanted or metalized to raise the reflectivity. In the work described in this thesis, reflectivity has not been modified by such measures.

Another important figure of merit of a detector is its spectral response, which is the relative strength of the photoconductivity signal at different wavelengths. The spectral response dictates in what wavelength range a detector can be used optimally. The photoconductive response for a detector doped with shallow, hydrogenic centers rises rapidly to a maximum when the photon has sufficient energy to raise the electron from the ground state to the conduction band edge and higher. At the band edge the density of states is zero and no transition can occur. However, the density of states rises rapidly and the transition probability follows $E^{1/2}$. Because of its large spatial dimensions the ground state wavefunction has a rather small extension in k-space. The rapidly falling off wavefunction leads to a drop of the spectral response proportional to $(h\nu - E_{ground\ state})^{2/3}$.

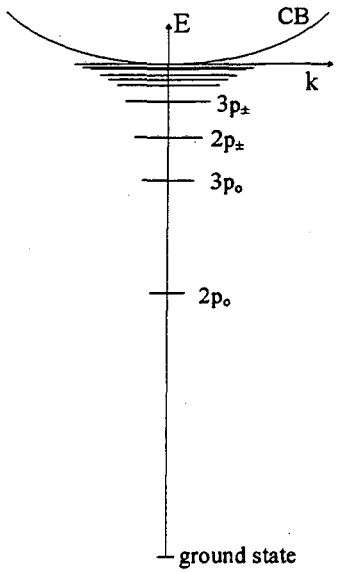

Fig. 1.3. Energy vs. k-space for a hydrogenic center exhibiting excited states.

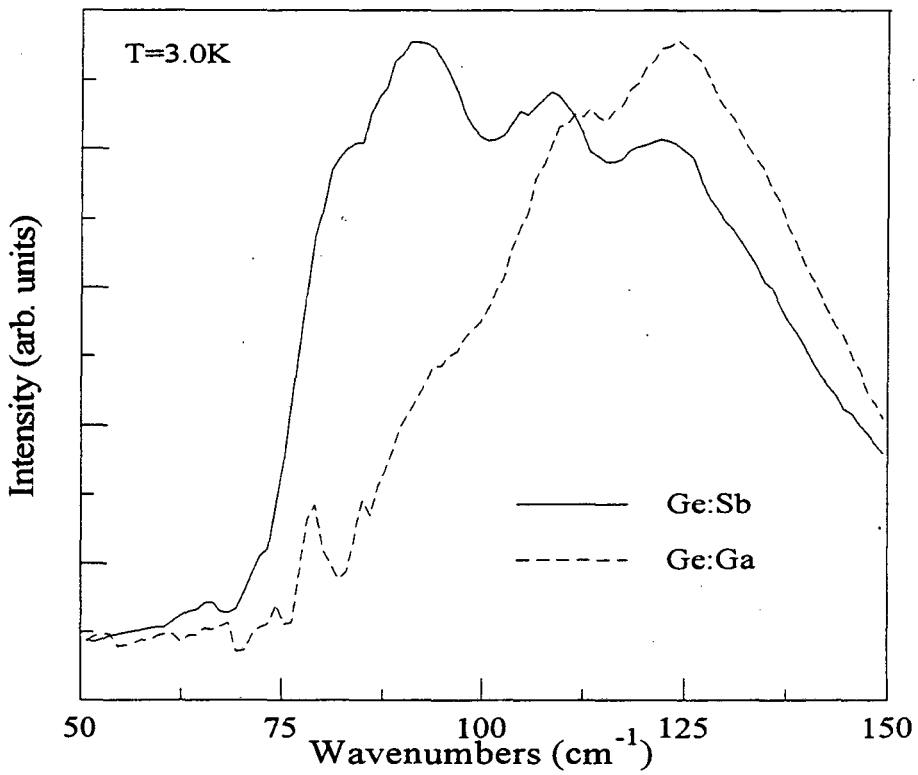

Figure 1.4. Photoconductivity spectral response of Ge:Ga and Ge:Sb. (Beeman, et. al. 1996) Decrease in response starting at 125 cm^{-1} is due to the FTIR instrument response and IR filters.

An additional parameter used to characterize photoconductive detectors is the Noise Equivalent Power (NEP). NEP is defined as the photon power required to produce a signal to noise ratio of one per unit bandwidth.

$$NEP = \frac{P}{S/N} \tag{1.11}$$

In the above equation P is the signal power (W), S is the signal current (A), and N is the background noise current (A/√Hz).(Haegel 1983) For satellite missions, a detector should have low NEP and high quantum efficiency. NEP values as low as 10^{-16} W/√Hz to 10^{-18} W/√Hz are typical for the best far IR Ge:Ga photoconductors in very low background applications. Ideally, the detector performance should be background noise limited. The background noise originates from the fluctuations in the photon stream, which is unavoidable. NEP_{BLIP} is the noise equivalent power of a given incident photon stream or the Background Limited Incident Photons (BLIP). The fluctuations induce noise in the detector and the NEP is given as

$$NEP_{BLIP} = 2\sqrt{Ph\nu} \tag{1.12}$$

where P is the signal power and hν is the photon energy.(Haegel 1983)

The detective quantum efficiency (DQE) is a useful figure of merit for the sensitivity of the photoconductor. It is given by:

$$DQE = \left(\frac{NEP_{BLIP}}{NEP_{measured}}\right) \tag{1.13}$$

The DQE measures how much noisier a detector responds compared to the theoretical noise limit.

In addition to the photon generated noise there are a number of electronic noise sources. These additional noise sources can originate from the detector or the amplifier electronics.

Johnson-Nyquist noise is due to the random thermal motion of charge carriers in a conductive material of resistance R_Ω. At the frequencies of relevance to our detectors, Johnson-Nyquist noise is "white", i.e., frequency independent.

$$V_{JN}df = \sqrt{4kTR_\Omega}df \tag{1.14}$$

In the above equation, k is the Boltzman constant T is the temperature.

Some electrical devices exhibit excess noise at low frequencies, which is called 1/f noise. The physical mechanisms leading to 1/f noise are attributed to the modulation of the conductivity inducing surface states, metal-semiconductor contacts, and charge trapping and detrapping at deep levels in depletion layers. If reliable Ohmic contacts are used for photoconductors, 1/f noise can be minimized.

Generation-recombination noise is due to the random thermal generation of free carriers in the photoconductor and their subsequent recombination. This random change in free carriers modulates the conductivity and results in current fluctuations.(van Vliet 1967) At low operating temperatures, thermal carrier generation is low and the resultant noise is due to the fluctuations in the recombination of photoionized carriers in the photoconductor. This mechanism results in a dispersion of the gain, due to varying transit times, but tends not to be a dominant noise source in IR photoconductors.

In low temperature photoconductors, the governing noise source is either photon or the Johnson noise associated with the feedback resistor in the amplifier electronics or

possibly the resistance of the detector. For a 10^{10} Ω feedback resistor at T=2 K the associated Johnson noise is ~1μV/√Hz. The observed noise background for our photoconductors and amplifier circuit is ~2μV/√Hz.

For space missions, very low photon backgrounds result in low NEP_{BLIP} values. To reach an NEP value close to NEP_{BLIP} requires both detector and amplifier noise be very small. Large responsivities help improve the detector NEP to achieve background limited performance. Airplane based telescopes such as the Stratospheric Observatory for Infrared Astronomy (SOFIA) and high altitude based telescopes such as the Keck I & II on Mauna Kea in Hawaii, have relatively high photon backgrounds and therefore high NEP_{BLIP}. The high NEP_{BLIP} limits the achievable sensitivity, therefore detector and amplifier noise requirements do not have to be as stringent as for low background conditions.

1.2.3 Present Technology

Germanium extrinsic photoconductors are well suited for far IR detection, because they have impurity ionization energies ranging from 10 meV (80 cm^{-1}) to 100 meV (800 cm^{-1}). (Bratt 1977) Germanium detectors doped with shallow gallium acceptors (Ge:Ga) respond from 83 cm^{-1} to 250 cm^{-1}. Ge:Ga detectors are operated near T = 3.0 K to minimize the dark current. The highest quantum efficiencies observed for Ge:Ga are ~10% while Ge:Be detectors can reach values as high as 50%.(Haegel 1983) The responsivity for Ge:Ga is typically 3 A/W at near 100 cm^{-1} for concentrations $[Ga]=2x10^{14}$ cm^{-3} and $N_D=10^{12}$ cm^{-3} and near 15 A/W for Ge:Be detectors at ≅100 cm^{-1}.(Haegel 1983) The quantum efficiency and responsivity of Ge:Be detectors are larger because greater

electric fields can be applied to Ge:Be before impact ionization occurs.(Sclar, et al. 1953) This effect has been observed by other researchers.(Bratt 1977) Germanium detectors doped with shallow antimony donors (Ge:Sb) respond from 80 cm^{-1} to 250 cm^{-1} with similar responsivity and noise levels as Ge:Ga detectors due to the similar ionization energies.(Beeman, et al. 1996)

Silicon is better suited for mid IR detection because its shallow dopant binding energies are between 4 to 6 times larger than in Ge.(Sclar 1976) In contrast hydrogenic donors such as silicon and sulfur in GaAs have ionization energies as small as 6 meV (Ozeki 1977) that can be used to detect photons with wavenumbers as low as ~ 40 cm^{-1}.

Because of the large Bohr radius of shallow donors in GaAs, dopant concentrations must be kept between $5x10^{13}$ and $1x10^{14}$ cm^{-3} to prevent hopping conduction which increases the dark current unacceptably. These impurity concentrations are not achievable in bulk GaAs, but Liquid Phase Epitaxy (LPE) GaAs is currently under development for IR photoconductors.(Wynne 1996) Using a dopant concentration of 10^{14} cm^{-3} and an optical ionization cross section of $3.3x10^{-14}$ cm^2, (Stillman, et al. 1977) the linear absorption coefficient is around 3.3 cm^{-1} for 6 meV photons. Due to the weak absorption, rather thick GaAs epilayers must be grown (≥0.5 mm) to achieve a quantum efficiency of over 10%.

The response of Germanium doped with shallow acceptors can be extended with uniaxial stress out to ~50 cm^{-1}. Application of large uniaxial stress to p-type Ge lowers the acceptor binding energy to ~ 6 meV(48 cm^{-1}).(Haller 1979) Ge:Ga photoconductors which are exposed to a large uniaxial stress have good sensitivity from 50 to 100 cm^{-1}, but

the mechanical stressing apparatus poses difficulties for fabricating detector arrays. Stressed detectors are fragile and are bulkier with the mechanical stressing rig. They are also subject to fracture during rocket launches. These drawbacks are some of the limitations that have motivated research in the area of germanium blocked impurity band (BIB) detectors. Advantages of BIB detectors over other conventional detectors will be discussed in the following section.

1.3 Blocked Impurity Band Detectors

1.3.1 Blocked Impurity Band Detectors: Structure and Operation

The Blocked Impurity Band (BIB) detector concept was proposed by Petroff and Stapelbroek in 1980 at Rockwell International Science Center. This detector was developed to reduce high energy radiation interaction. Cosmic radiation hits lead to large concentrations of electron-hole pairs which can dramatically change detector responsivity over significant time spans and which can easily overload the highly sensitive amplifier electronics.

A BIB detectors consists of a two layer structure: a heavily doped (IR absorbing) region and a thin, pure (blocking) layer. The two regions are sandwiched between two degenerately doped contacts.(Figure 1.5) The absorbing region typically is 10 to 100 μm thick while the blocking region is much thinner, 2 to 5 μm.

The application of a positive voltage bias on the blocking layer side of a BIB detector creates a depletion layer analogous but not equal to a depletion layer in a p-n junction. In a p-n junction the depletion layer is devoid of free carriers (electrons and holes) and contains locally fixed ionized acceptors and donors.

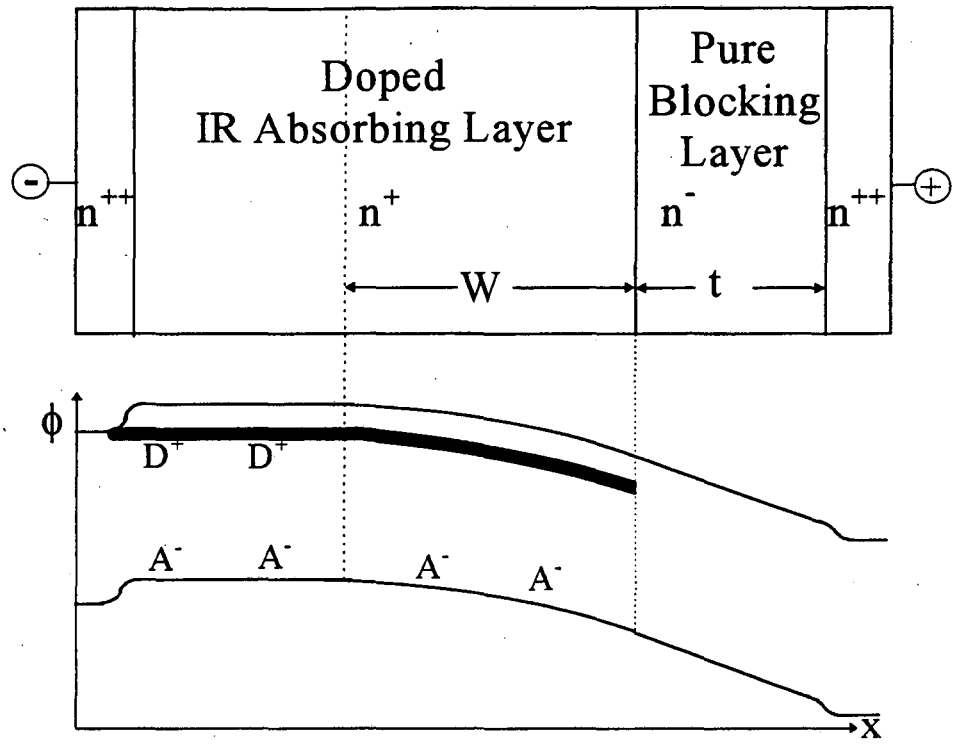

Fig. 1.5 (top) Schematic of components of n-type BIB detector (bottom) Energy band diagram of n-type BIB under reverse bias.

Unlike in a p-n junction the depletion layer in a n-type BIB is devoid of ionized donors. Hopping conduction in the impurity band allows positively charged donor states (not the donors) to move to the negatively biased contact via electrons moving through the banded impurity states. The detector is at low temperature ($T \leq 2$ K) such that electrons are frozen out onto the impurity band. The width of the depletion layer W depends on the minority dopant concentration N_a in the IR absorbing layer, the blocking layer thickness t, and the applied voltage V_a.(Petroff and Stapelbroek 1984)

$$W = \sqrt{\left[\frac{2\varepsilon\varepsilon_o(V_a - V_{bi})}{eN_a} + t^2\right]} - t \qquad (1.15)$$

In the above equation, $\varepsilon\varepsilon_o$ is the dielectric constant and V_{bi} is the built in voltage. The built-in voltage is due to the dopant difference at the IR absorbing layer and pure blocking layer interface. Typically, V_{bi} can be neglected because the applied bias is much larger ($V_a >> V_{bi}$). Photon excited charge carriers are only collected from the depleted region W of the IR absorbing layer. Therefore W has to be sufficiently large to absorb a significant fraction of the incoming IR photons.

When the bias is first applied, electrons are injected from the negatively biased contact into the doped layer. A n-type BIB detector is shown with a positive bias on the blocking layer side in Fig. 1.5. The electrons travel through the impurity level and are captured by the ionized donors. Thus, the positive donor states, not the actual impurities, are swept out towards the negatively biased contact. The space charge remaining in the depletion layer is given by ionized acceptors.

When a photon excites an electron inside the depletion layer into the conduction band, this free carrier drifts in the electric field through the depletion layer and the blocking layer in the conduction band to the positively charged contact. The positive donor state D^+ created in this ionization event propagates via hopping of electrons from neighboring neutral donors all the way to the negative electrode. Independent of the location of the photoionization event, a total of one charge crosses the total distance of the depletion layer plus blocking layer. The collection of both the electron and the ionized donor state results in unity photoconductive gain, which is one of the advantages of BIB detectors over conventional photoconductors. This gain is defined by the ratio of the mean free path of the charge produced in an ionization event and the interelectrode

distance. Unity gain, in contrast to gain distribution found for standard photoconductors, leads to lower electronic generation-recombination noise.

The IR absorbing layer is doped to a much higher concentration (~10^{16} cm^{-3} majority shallow impurities, ~10^{12} cm^{-3} minority impurities) than conventional photoconductors (~10^{14} cm^{-3} majority shallow impurities, ~10^{12} cm^{-3} minority impurities). At these high concentrations, the dopant bound carrier wavefunctions begin to overlap leading to broadening of the dopant energy levels. The hopping conduction occurs between the impurities, which would lead to large dark currents if the blocking layer were not present. To suppress a hopping conduction current, the concentration in the blocking layer must be below 10^{13} to 10^{14} cm^{-3} in Ge.

The increase in the width of the impurity energy band with dopant concentration leads to a decrease in the effective ionization energy. For shallow levels in Ge, a decrease in the ionization energy begins to occur near $5x10^{15}$ cm^{-3} and at doping concentrations above ~$3x10^{17}$ cm^{-3} the donor (acceptor) dopant band has merged with the conduction (valence) band, leading to metallic conduction.(Debye and Conwell 1954) For shallow levels in Si, the ionization energy starts to decrease around $1x10^{17}$ cm^{-3} and above doping concentrations of $3x10^{18}$ cm^{-3} the conduction is metallic.(Petroff and Stapelbroek 1985). This decrease in ionization energy provides a photoconductive response at extended wavelengths, a desirable property for many photodetector applications.

Reduction of cosmic radiation absorption was the driving force for BIB detector development. The high doping concentration provides increased absorbance requiring a thinner layer for efficient photon absorption. The resulting reduction in total detector

volume of about 100 compared to standard photoconductors decreases the rate of cosmic radiation "hits" during device operation. All of these advantages were realized during the development of Si BIB detectors.

1.3.2 State of the Art of Silicon Blocked Impurity Band Detectors

The BIB detector was first developed in Silicon doped with As and Sb and showed response to 28 and 40 μm respectively. During the development of the Si BIB, Petroff and Stapelbroek published papers modeling the behavior of these BIB detectors. They developed models for the activation process of carrier transport through the impurity band of the IR absorbing layer. Petroff and Stapelbroek calculated an activation energy E_A (eV) for impurity band conduction.(Mott and Twose 1971)

$$E_A = 1.46\left(\frac{e^2}{4\pi\varepsilon\varepsilon_o}\right)\left(N_D^{1/3} - 1.35N_A^{1/3}\right) \tag{1.16}$$

N_D is the majority donor concentration (cm^{-3}), N_A the minority acceptor concentration (cm^{-3}), $\varepsilon\varepsilon_o$ is the dielectric constant, and e the electron charge. Equation 1.16 was found to yield activation energies between 2.5 and 4 meV for Ge BIB detectors which agrees with hopping conduction data for Ge.(Shklovski and Efros 1984)

For an ionization event in the depletion layer a positive donor state D^+ is created and propagates via hopping of electrons from neighboring neutral donors all the way to the negative electrode. The frequency response of the detectors was calculated using the rate limiting step to be the collection of the ionized donors traveling in the impurity band. The positive ionized donor state has a lower mobility μ_{D+} compared to the photoexcited

electron in the conduction band with mobility μ_n. Equation 1.17 is the characteristic time τ_D for collection of the D^+ states.(Petroff and Stapelbroek 1985)

$$\tau_D = \frac{\varepsilon\varepsilon_o}{e(\mu_D+)N_A}\left[1+\frac{N_A}{N_D}\exp(\frac{E_A}{kT})\right] \tag{1.17}$$

T is temperature in K and k is the Boltzman constant. When a photon excites an electron inside the depletion layer into the conduction band, this free carrier drifts in the electric field through the depletion layer and the blocking layer in the conduction band to the positive contact. The collection time τ_e for the electrons is $\sim 10^3$ shorter than τ_D.

$$\tau_e = \frac{\varepsilon\varepsilon_o}{e\mu_n N_A} \tag{1.18}$$

These response times were used to calculate the frequency dependent gain. The dc gain is unity, unless recombination of the D^+ states and photogenerated electrons becomes significant. At high photon background conditions the collection efficiency falls off because of this recombination process.

To calculate the spectral response, a Gaussian distribution was used for the density of states of the donor impurity band as depicted in Fig. 1.6. The absorption coefficient α is calculated from

$$\alpha = \sigma_o N_D \sqrt{2\pi} B \int_0^{E(\lambda)} \exp(-[E - E_I]/2B^2)dE \tag{1.19}$$

$$\text{where } B = (0.001eV + 5x10^{-21}(eVcm^3)N_D)/\sqrt{2} \tag{1.20}$$

$$\text{and } E_I = E_D - \sqrt{2}B \tag{1.21}$$

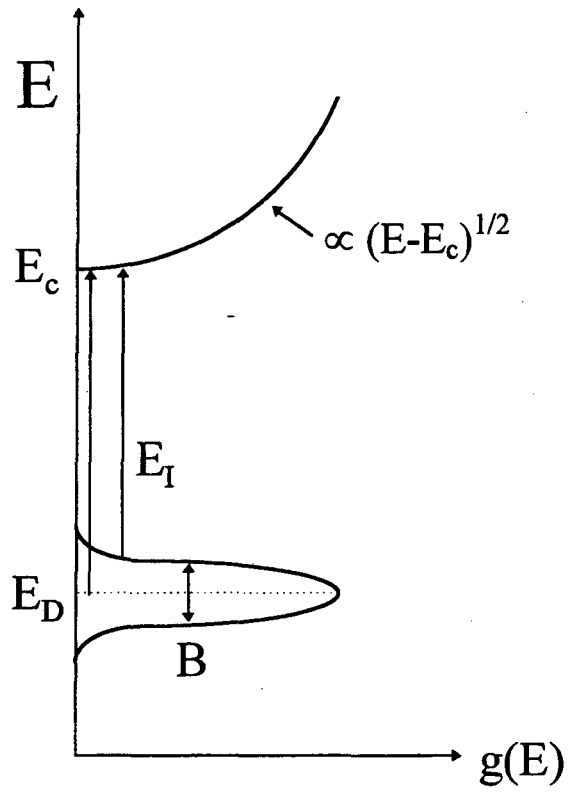

Fig. 1.6. Energy vs. density of states for a donor impurity band.

where σ_o is photon absorption cross section, N_D is the doping concentration, B is the dopant impurity's width in energy at half of the maximum density of states, E_D is the ionization energy of a neutral donor, and E_I is a reduced average photo-ionization energy. Due to the complex behavior of the metal to insulator transition in semiconductors, the exact behavior of broadening of the impurity level in not known. Petroff and Stapelbroek presented the width dependence being proportional to N_D in equation 1.20, but gave no theoretical support. The N_D prefactor is only applicable for Si in this relationship for B due to the specific metal to insulator transition. Another theory developed by Shklovskii and Efros (1984) for hopping conduction finds B proportional to $N_D^{1/12}$ to be discussed later.

Development of Si BIB detectors has had technological advantages over Ge BIB detectors for several reasons. Si has deeper impurities such as P with E_c-45 meV as opposed to E_c-11 meV in Ge. Due to deeper impurities, hopping and banding conduction occurs at higher concentrations. Therefore the maximum allowed concentration for the blocking layer is higher in Si (10^{14} cm^{-3}) compared to Ge (10^{13} cm^{-3}). Also Si CVD is technologically much more advanced compared to Ge CVD. Si BIB detectors doped with As & Sb have been successfully developed using CVD.(Reynolds, et al. 1992; Huffman, et al. 1992)

1.3.3 Ge Blocked Impurity Band Detectors

Properly operating Ge BIB detectors should be competitive with stressed photoconductors in the 6 meV (50 cm^{-1}) to 11 meV (90 cm^{-1}) photon energy range, because the photoionization threshold of shallow dopants in the heavily doped absorbing layer is extended to lower energies due to dopant-dopant interactions. The effective ionization energy drops to 6 meV (50 cm^{-1}) for a shallow donor concentration near 10^{16} cm^{-3}.

The width of the absorbing region W has to be sufficiently large to capture a significant fraction of the incoming IR photons. Using equation 1.9, the quantum efficiency has been plotted against the absorption coefficient α times the absorption length W for a BIB detector. The quantum efficiency plateaus at 0.64 due to the reflectivity of 0.36 at the entrance surface. Using a photoionization coefficient of 10^{-14} cm^2 and an absorbing layer concentration of $2x10^{16}$ cm^{-3}, an αW of 2 can be achieved with a depletion width of 100 μm. Depletion widths of 10 to 100 μm require that minority concentrations

are of the order of 10^{12} cm^{-3} or less in the doped layer. Figure 1.8 shows the relationship of depletion vs. bias in Ge using equation 1.15 for a blocking layer thickness of 10 μm.

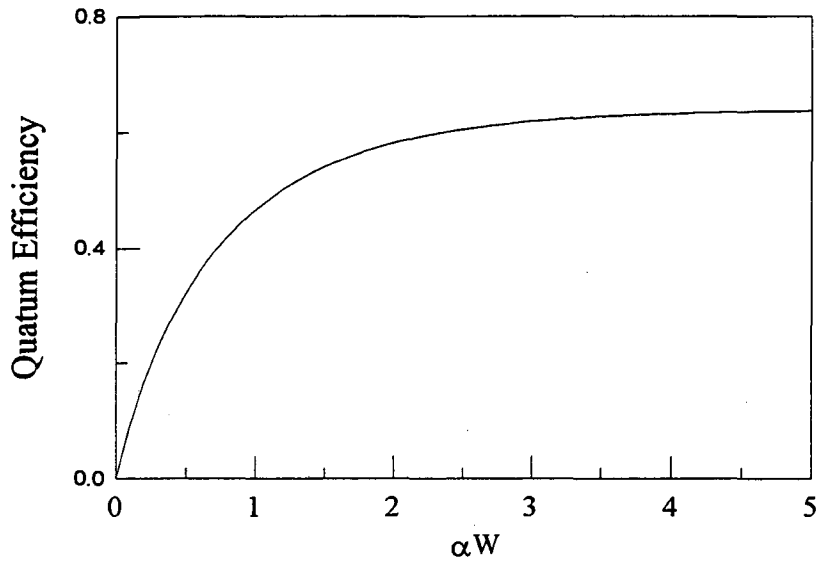

Fig. 1.7. Quantum efficiency vs. absorption coefficient times absorption length W of a Ge BIB detector.

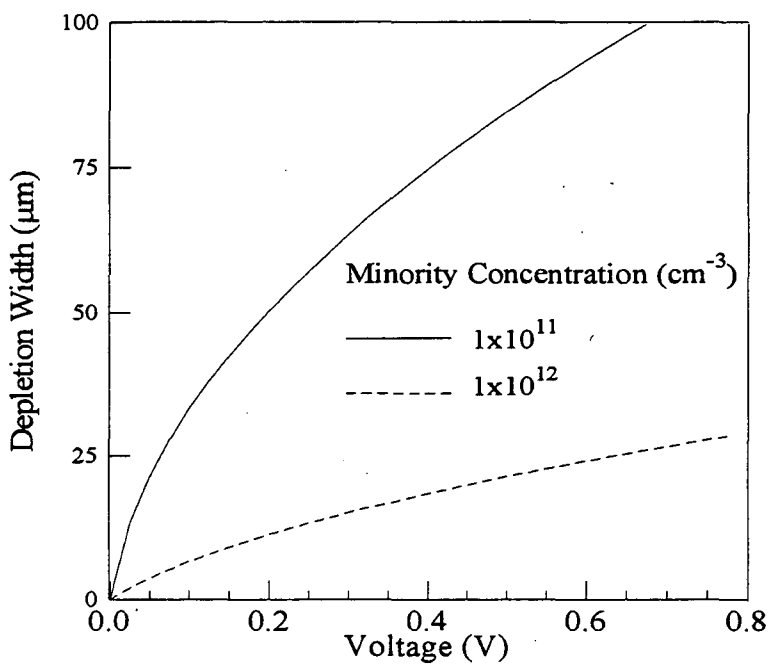

Fig.1.8. Depletion Width of Ge BIB detector as a function of minority concentrations for a blocking layer thickness of 10 μm.

Using equation 1.17, the frequency response of a Ge BIB detector was calculated. For the simulation shown in Fig. 1.9, the following parameters were used.

Parameter	Value
μ_{D+}	1 cm^2/Vs
N_D	$3x10^{16}$ cm^{-3}
N_A	10^{12} to 10^{13} cm^{-3}
E_A	2 meV

Table 1.1 Parameters for frequency response simulation.

The activation energy E_A was determined from hopping conduction transport in n-type Ge. (Shklovski and Efros 1984)

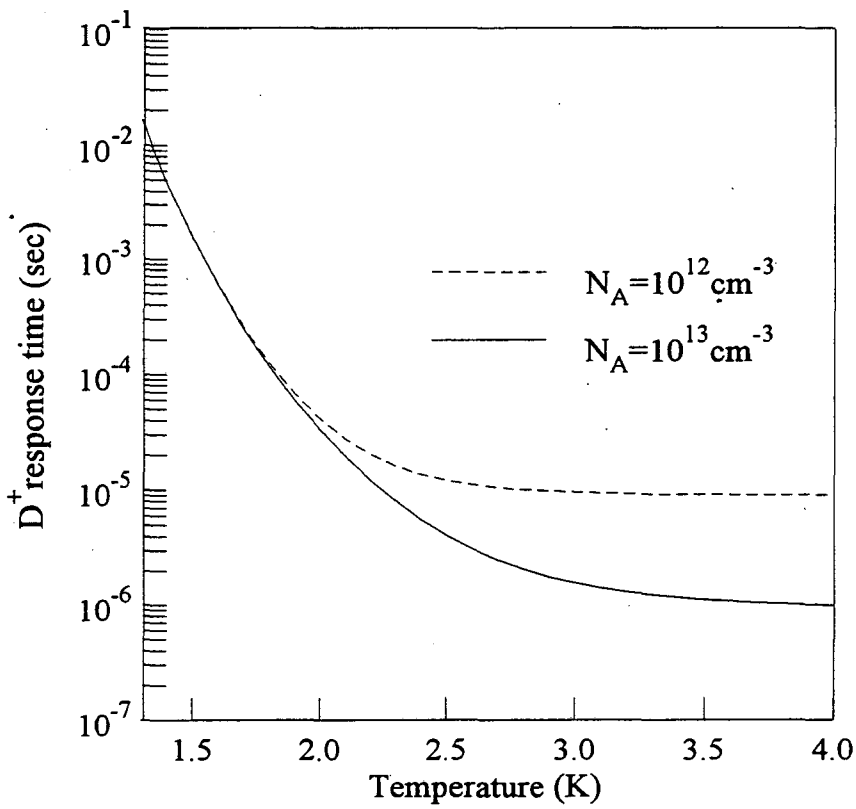

Fig. 1.9. Device response time for two minority dopant concentrations.

Ge BIB detectors have to be operated between 1.3 to 2.0 K to reduce the dark current to acceptable levels. At 1.3 K the frequency response is approximately 100 Hz, unless it is limited by some other mechanism such as the RC response.

The spectral response of a Ge:Sb BIB detector (Fig. 1.10) was calculated using equation 1.19. The energy width B in equation 1.20 was modified to correct for the difference in metal to insulator transition between Si and Ge. The prefactor in front of the N_D was increased by 10.

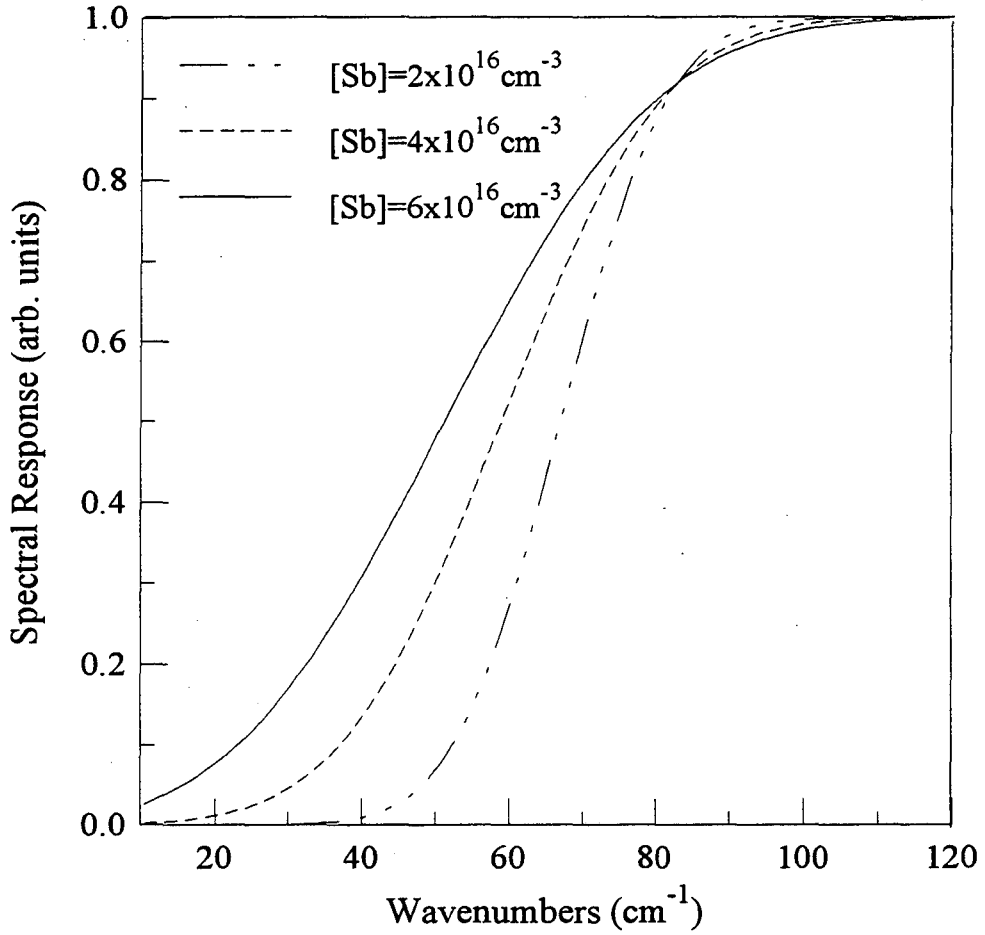

Fig. 1.10. Theoretical spectral response of a Ge:Sb BIB detector using $B \propto N_D$.

Parameter	Value
N_A	$5x10^{11}$ cm^{-3}
N_D	2 to $6x10^{16}$ cm^{-3}
ε	16
E_D	10.3 meV

Table 1.2 Parameters used in calculating theoretical spectral response.

The parameters used in this model are given in Table 1.2. Because the energy broadening given by Petroff and Stapelbroek may over estimate the relationship to N_D, another model was used that was developed for hopping conduction under low compensation.(Shklovski and Efros 1984; Pasquier, et al. 1994)

$$B = 0.43\left(\frac{N_A}{N_D}\right)^{1/4}\gamma \quad \text{where } \gamma = 0.99\frac{e^2 N_D^{1/3}}{\varepsilon\varepsilon_o} \tag{1.22}$$

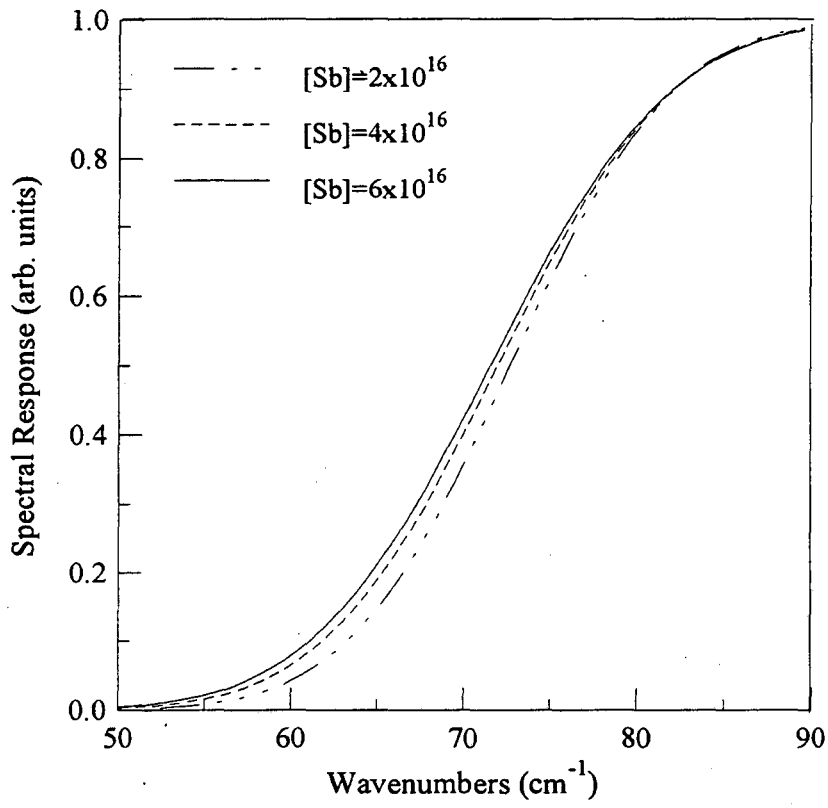

Fig.1.11. Theoretical spectral response of Ge:Sb BIB detector using $B \propto N_D^{1/12}$.

The spectral response in Fig. 1.11, underestimates the broadening of the impurity wavefunction due to an increase in the dopant concentration with B proportional to $N_D^{1/12}$. Determining the dependence on N_D is experimentally difficult, but properly working BIB detectors may be useful in determining which of the two theoretical models is correct.

1.3.4 Review of Past Ge BIB Detector Efforts

Several attempts have been made to fabricate Ge BIB detectors using CVD. Rossington's work (1988) suffered from gas phase nucleation and inhomogeneties across the wafer. In addition, epilayers tended to be impure due to the reactive gases. Earlier attempts focused on using GeH_4, because of lower reaction temperatures, but safety issues prompted the use of $GeCl_4$. The higher temperatures required to crack $GeCl_4$ precursors caused substrate dopant out-diffusion which resulted in a dopant gradient at the epi-substrate interface, where a sharp interface is preferred. Lutz (1991) showed that oxygen contamination occurs at the epi-substrate interface at a concentration of 10^{18} cm^{-3}.

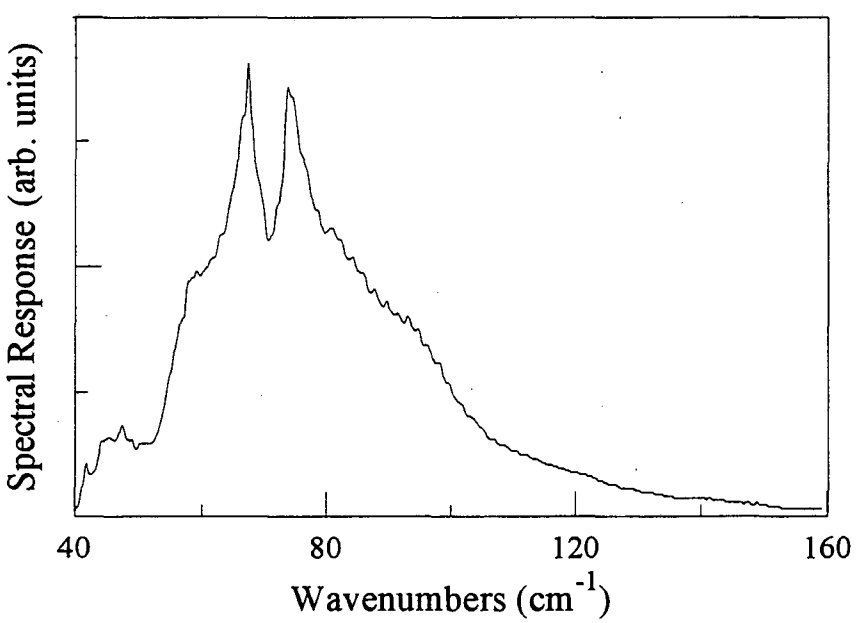

Fig. 1.12. Spectral response of Ge:Ga BIB detector 3A1 at 1.7K.
(Watson and Huffman 1988)

Watson and Huffman (1988) were able to produce detectors that responded to 50 cm^{-1}, Fig. 1.12, but other figures of merit, such as dark current were very high and these detector results were not reproducible. Boron ion implantation into high-purity Ge was also used to form the infrared absorbing layer, but removing the substrate to leave a few μm thin blocking layer was extremely difficult, and defects in the implanted infrared absorbing layer could not be removed completely. (Wu 1993; Olsen 1994) Wu did have some success with extending the spectral response as shown in Fig. 1.13, but the response was not reproduced in other devices.

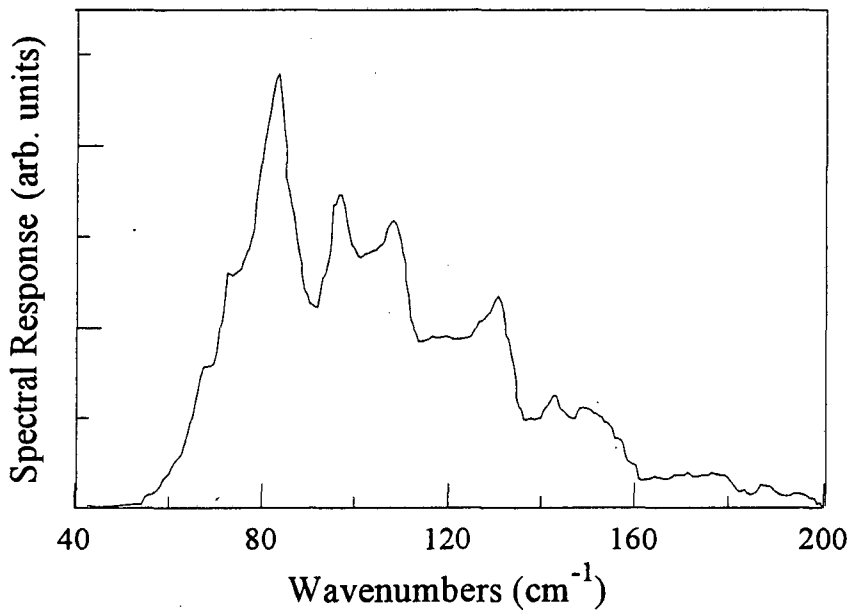

Fig. 1.13. Spectral response of boron-implanted Ge BIB detector.(Wu, et al. 1991)

All these attempts to fabricate BIB detectors were successful to a degree, but still were not satisfactory and reproducible. These partial successes prompted the exploration of yet another epitaxial technique, Liquid Phase Epitaxy (LPE), to produce BIB detectors.

2. Germanium Liquid Phase Epitaxy

2.1 Introduction

2.1.1 Background

The Liquid Phase Epitaxy (LPE) technique utilizes the controlled precipitation of a dissolved material (solute) onto a substrate by lowering the solvent temperature below the liquidus temperature. The supersaturation in the solvent drives the growth onto low energy surfaces, typically the substrate. Homogenous nucleation in the melt requires a greater surface energy to form a nucleation site. The epitaxial growth restores the composition of the solvent to the liquidus curve. Precipitation of Ge from the Pb occurs on the Pb rich side of the phase diagram shown in Fig. 2.1.

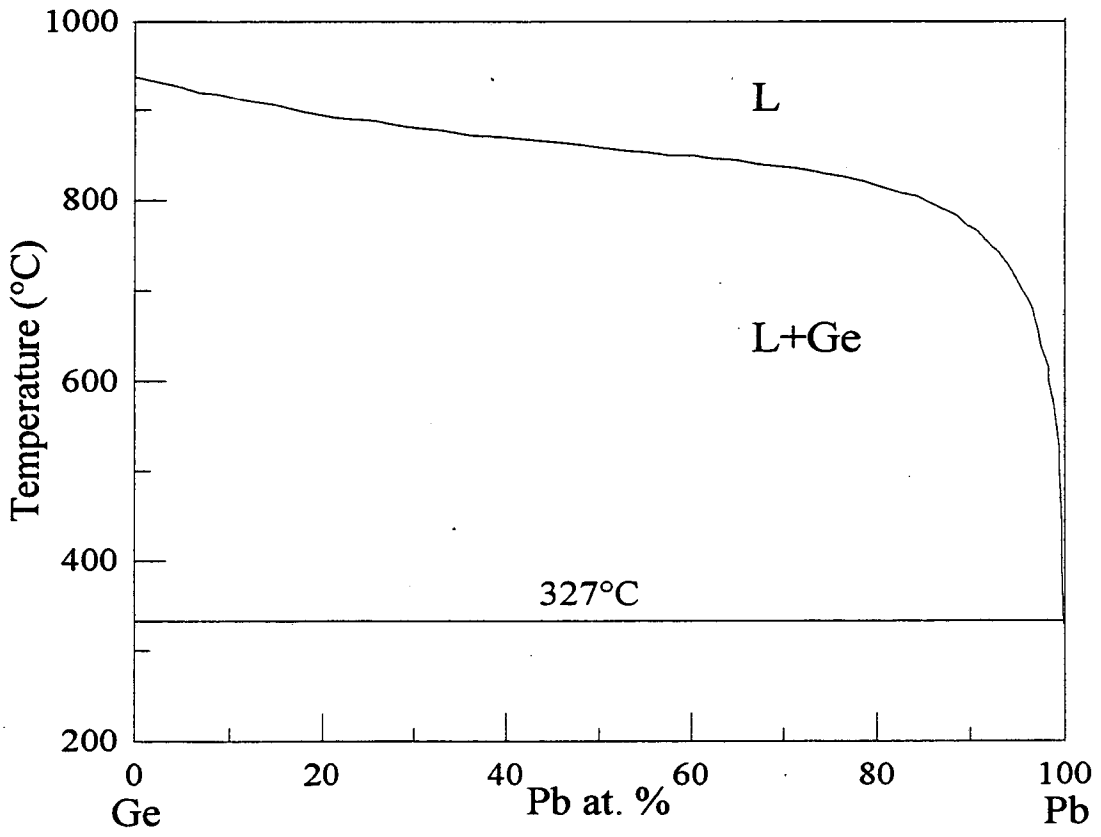

Fig. 2.1. Ge-Pb phase diagram.(Olesinski & Abbaschian 1984)

In order to perform efficient and reproducible liquid phase epitaxial growth of Ge with a Pb solvent, it is important to inspect the Ge-Pb phase diagram at low concentrations of Ge. Two groups have measured this section of the phase diagram and their data are plotted in Fig. 2.2. Thurmond and Kowalchik (1960) measured Ge concentrations in Pb liquid from a temperature of 628°C to 785°C, while later on Immorlica and Luddington (1981) determined the phase diagram over a wider temperature range from 400°C to 700°C. Estimates of the Ge concentration in Pb for this research are also included in Fig. 2.2.

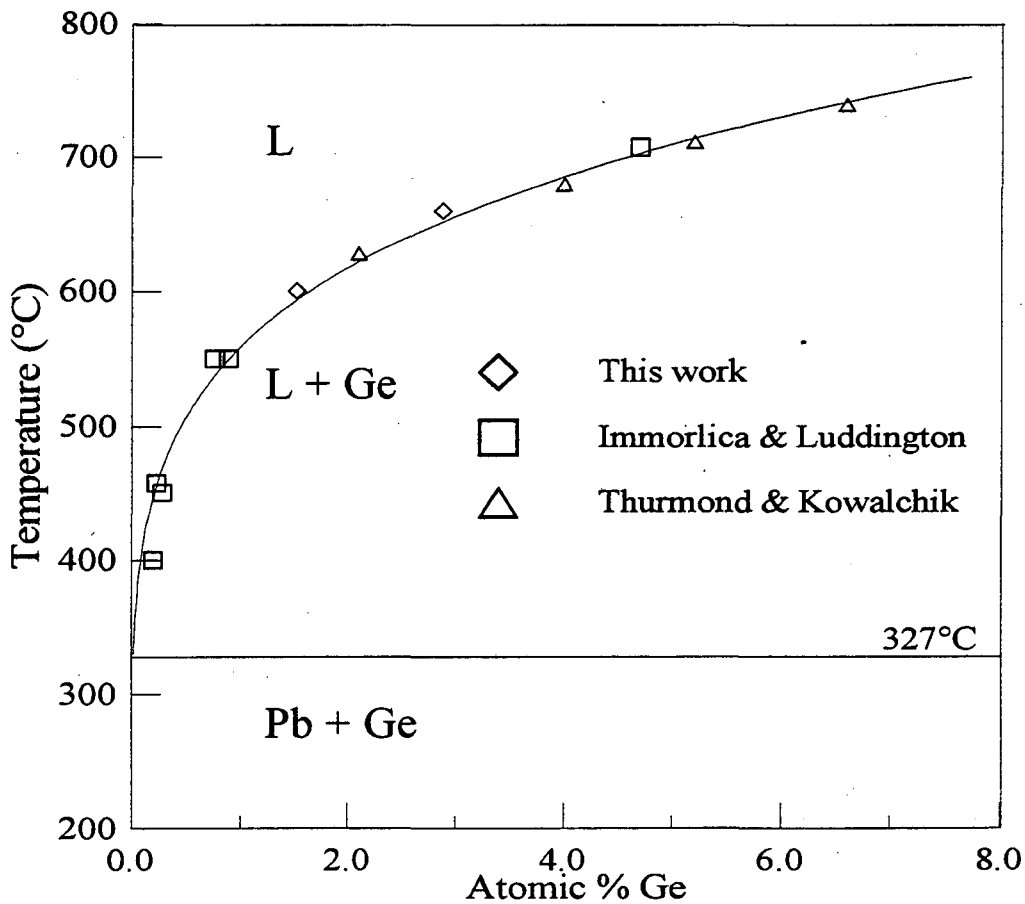

Fig. 2.2. Phase Diagram of Ge-Pb on the Pb rich side. (L = liquid phase, L + Ge = liquid phase plus solid Ge, Pb + Ge = solid Pb & Ge).

The composition was determined by holding the dissolution temperature constant and increasing the amount of Pb until the Ge solute charge had dissolved completely. The solubility data can be described by an exponential relationship:

$$X_S = X_O \exp(\frac{-\Delta H}{RT}) \tag{2.1}$$

with X_o = pre-exponential constant, X_s = atom fraction solubility, ΔH = enthalpy of the system, and R = universal gas constant.

Authors	X_o	ΔH
Immorlica & Luddington	172	67.5 kJ/mol
Thurmond & Kowalchik	2.19×10^3	86.7 kJ/mol
Best fit for all data	380	72.7 kJ/mol

Table 2.1 Solubility parameters for Ge-Pb system at low Ge concentration.

The dissolution of 2.5% Ge in Pb at 650°C allows thick epilayers of Ge to be grown from Pb solutions. The solubility data is summarized in Table 2.1 for the Pb-Ge system at low Ge concentrations.

Because of the solvent mediated surface transport, LPE allows growth to occur at lower temperatures than Molecular Beam Epitaxy (MBE) and Chemical Vapor Deposition (CVD). At these lower temperatures, less impurities are generated by the growth chamber materials. Despite these advantages, very limited research on Ge LPE and no systematic studies on high purity Ge LPE have been performed.

2.1.2 LPE Growth Processes

Lateral microscopic growth occurs on viscinal surface steps on low index planes. Viscinal surface steps are present when a substrate is slightly misoriented from the low

index plane. This lateral microscopic growth results in perpendicular macroscopic growth in the surface normal direction shown in Fig. 2.3.

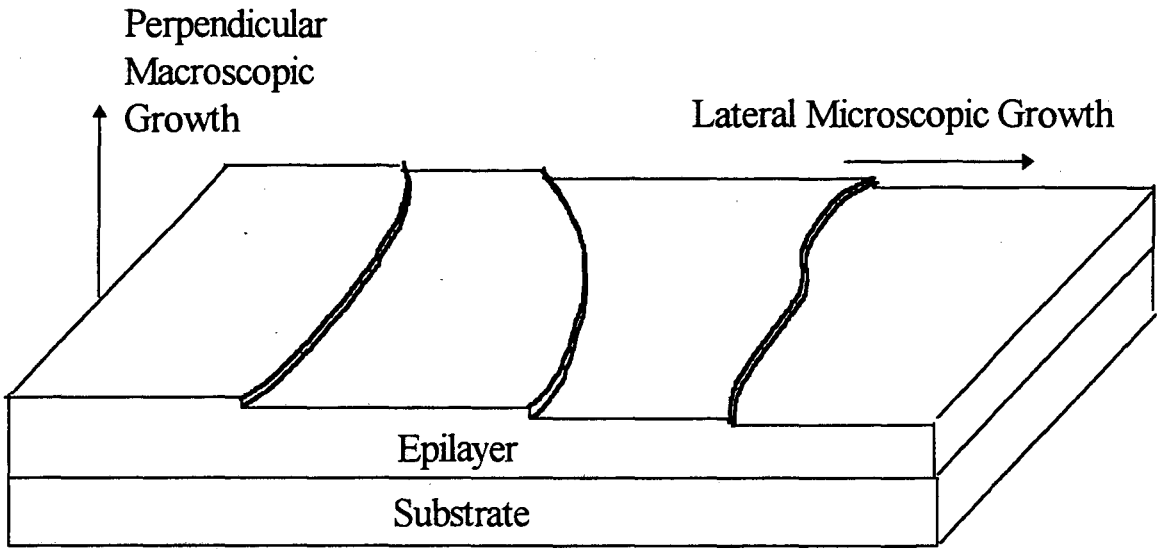

Fig. 2.3. Terrace growth mechanism resulting in perpendicular macroscopic growth.

An example of this growth morphology is shown in Fig. 2.4.

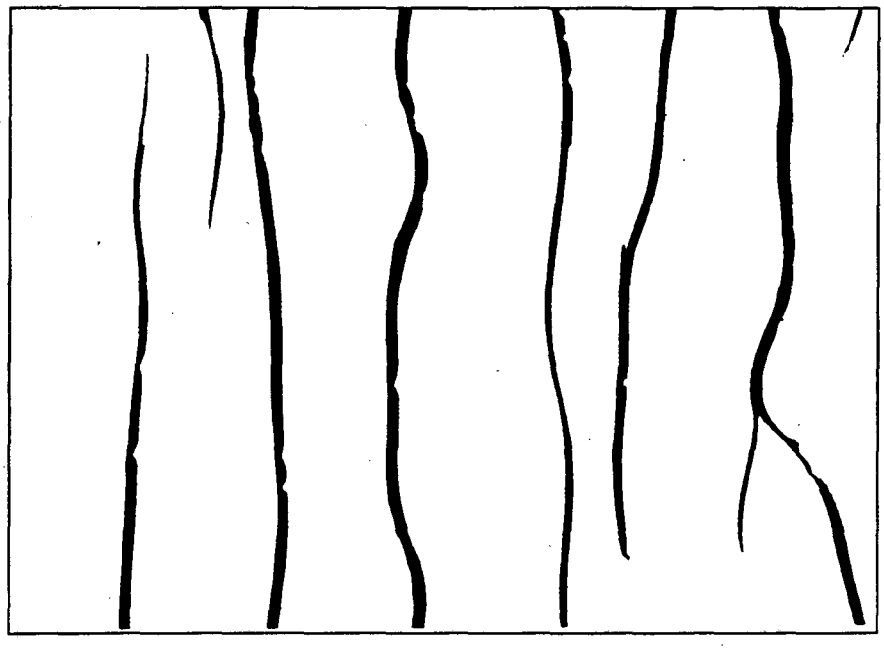

Fig. 2.4. Surface morphology of LPE #277 at x225 magnification with a 0.47°C/min. cooling rate.

This surface morphology can be observed to change with a greater cooling rate.

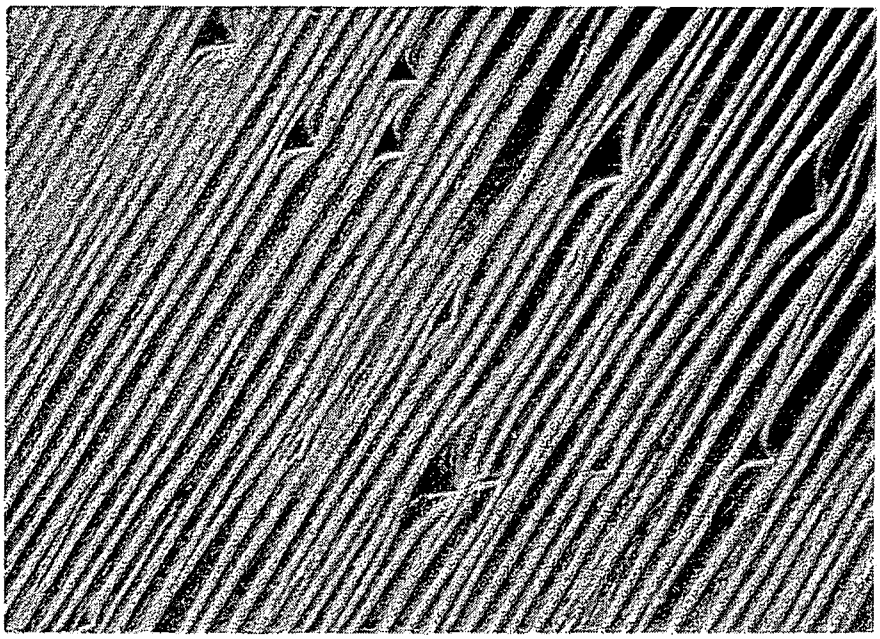

Fig. 2.5. Surface morphology of LPE #108 at x225 magnification with 1.25°C/min. cooling rate.

The distance between steps on the surface increases for slower cooling rates, because the steps have time to coalesce. The step coalescence increases the average step height such that they become macroscopic. At this point the large flat regions between the steps are called terraces.(Bauser 1984)

For Ge LPE growth, perpendicular macroscopic growth was observed for (111) oriented substrates. For (100) oriented substrates, the low (111) surface energy resulted in a flat top pyramid type of surface morphology, shown in Fig. 2.6.

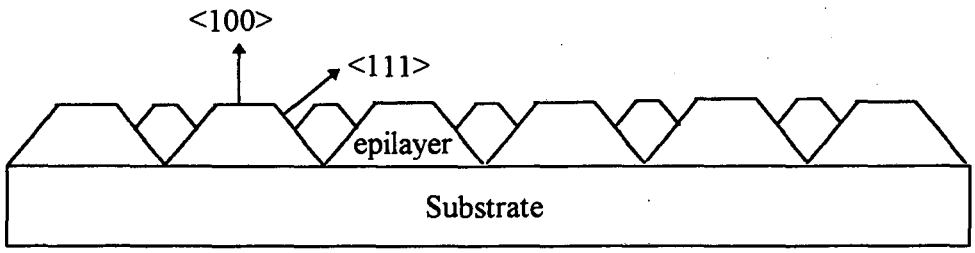

Fig. 2.6. Surface morphology of Ge LPE on (100) oriented substrates.

The (100) morphology lacks the planar quality needed for fabricating BIB detectors, so all growths were performed on (111) oriented Ge substrates.

E. Bauser (1985) performed detailed studies of the growth mechanisms and resulting morphology for LPE in the GaAs system. Bauser showed how the growth morphology depends on the substrate orientation.(Figure 2.7)

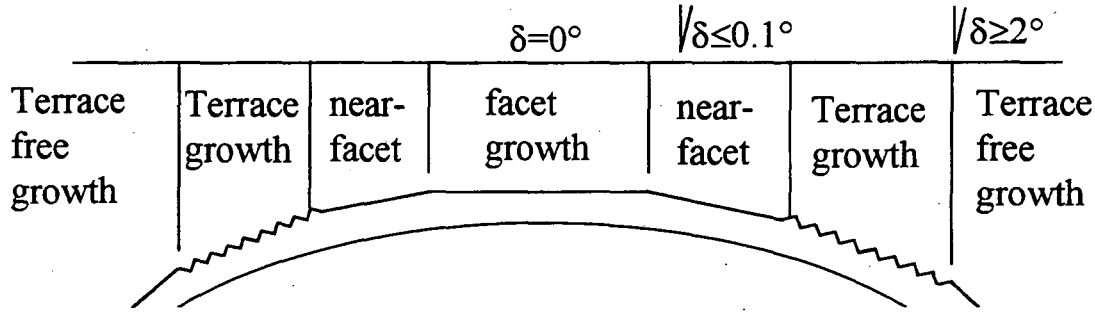

Fig. 2.7. Schematic cross section of spherical substrate with LPE epilayer grown on top. δ is the misorientation of the substrate. (Bauser 1985)

Bauser used a spherical substrate with a radius of 1 meter to obtain all the morphology dependencies in one epilayer growth. Bauser also showed that for facet growth at δ=0°, dislocations are required to provided growth steps. With dislocation free substrates, the facet growth is extremely suppressed.(Bauser 1994)

The growth rate of LPE has been shown in many material systems to be limited by the diffusion in the melt.(Tiller 1968) Maintaining low cooling rates is essential if thick films are desired. The Ge must diffuse through the solvent layer of thickness δ that is depleted of Ge at the melt-substrate interface.(Figure 2.9)

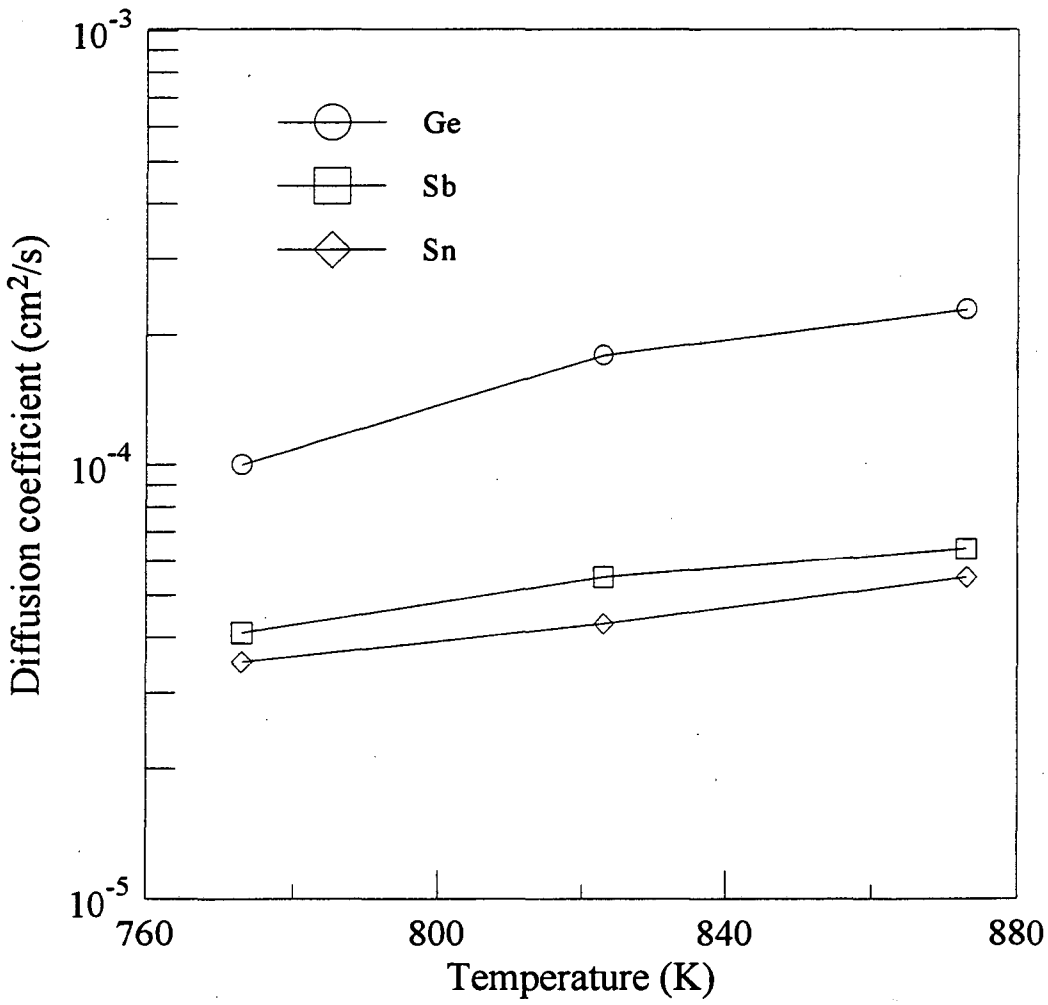

Fig. 2.8. Diffusion of metals in Pb liquid.
(Roy and Chhabra 1995; Immorlica and Ludington 1981)

The diffusivity of Ge in Pb can be extrapolated to be $3x10^{-4}$ cm^2/s at 650°C. Other elements have similar diffusivities near Ge in Figure 2.8.

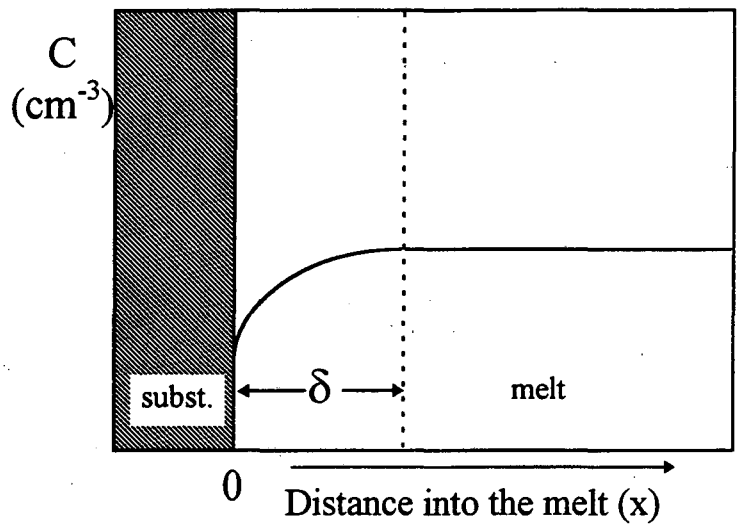

Fig. 2.9. Schematic of concentration gradient at surface of substrate.

Simple models for LPE have been developed for calculating epilayer growth rates and thickness.(Hsieh 1974) Most of these apply to step cooling used to induce the supercooling. An equation for short growth times has been developed ($Dt/L^2 < 1$). D is the diffusion coefficient, t is time, and L is solution thickness. The epilayer thickness, H, is given by

$$H = \frac{2}{C_s m}\sqrt{\frac{D}{\pi}}\left(\Delta T t^{1/2} + \alpha t^{3/2}\right) \tag{2.2}$$

where C_s is the concentration of solute in the solid, m is the slope of the liquidus curve, α is the cooling rate, and ΔT is the temperature difference of the supersaturation of the solution.

For long times ($Dt/L^2 >> 1$) equation 2.2 no longer applies. Researchers have observed for long ramp-cooling experiments that precipitates form on the surface of the solvent. This work used long ramp-cooling to obtain thick (50 to 100 μm) epilayers. Ge

precipitates which compete as growth sites with the substrate were present on the surface of the Pb solvent after growth runs.

2.1.3 Convection in the Solvent

The cooling rate during LPE is kept low (<1°C/min.) to prevent thermal convection of the solvent and constitutional supercooling, which disrupts planar growth. Associated with the concentration gradient, dC/dx in the melt shown in Fig. 2.9, there is a temperature gradient, G_L=dT/dx, which is related by the slope of the liquidus dT/dC. (Minden 1970)

$$\frac{dT}{dx} = \frac{dC}{dx}\frac{dT}{dC} \tag{2.3}$$

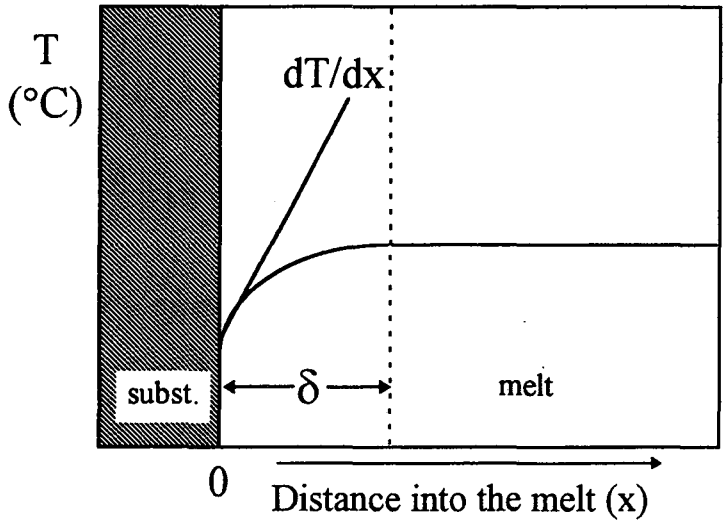

Fig. 2.10. Schematic of temperature gradient in the melt at the substrate.

Convection cells across the substrate can disrupt the growth front and produce irregular growth. Convection can be prevented by keeping the temperature gradient sufficiently under a critical value for a given W, the solution thickness.(Tiller 1967) The critical gradient G_C is given by

$$G_C = \frac{R_C \alpha \nu}{W^4 g \beta} \tag{2.4}$$

Lord Rayleigh (1916) showed that an instability occurs for a fluid heated from below at a critical transition value or Rayleigh number R_C is 1700±100. The instability occurs due to a stratification of density which results from heating and thermal expansion.

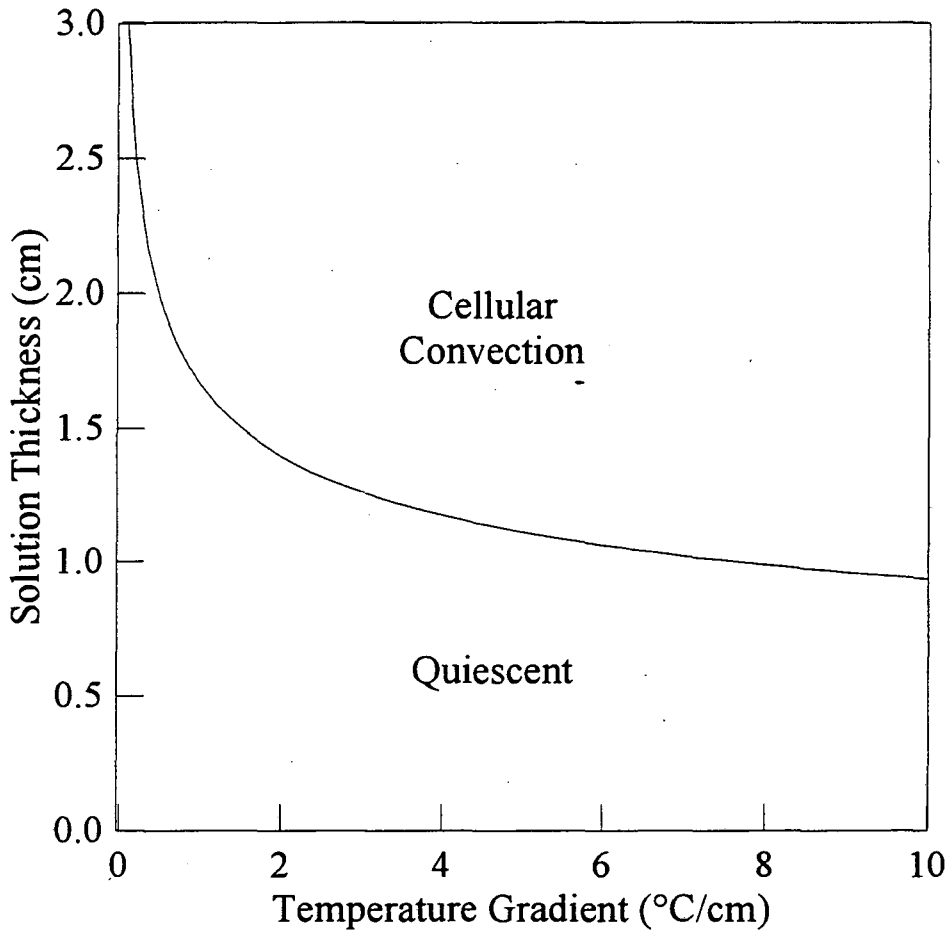

Fig. 2.11. Criteria for onset of cellular convection in the growth solution.

Equation 2.4 shows that convection depends on gravity g and properties of the Pb solvent such as the thermal diffusivity α, the viscosity ν, and the volume expansion coefficient β. These properties are summarized in Table 2.2.

Property	Pb value
α	0.11 cm^2/s
ν	0.0012 cm^2/s
β	$3x10^{-5}$ K^{-1}

Table 2.2. Physical properties of Pb at 650°C.

Using the above equation 2.4 and a solution thickness of 8 mm appropriate for Ge growth conditions, the boundary between a convective and quiescent solution occurs at a temperature gradient of 24 °C per cm. This large a gradient is very unlikely to occur and therefore we conclude that the Ge LPE growth in our system progresses under quiescent solution conditions.

LPE growth occurs under extremely low temperature gradients such that the process is very near equilibrium conditions. This leads to very low thermal stresses (Astles 1990) and low dislocation densities.(Kumer and Takagi 1977)

2.1.4 Segregation of Impurities

LPE of high purity group IV semiconductors requires a solvent that does not by itself contaminate (dope) the epitaxial layer and can be obtained with sufficient purity. Growth of III-V compounds containing In or Ga is straightforward because group III elements can be used as the solvent. LPE of doped GaAs from Ga solvent is a standard commercial process for inexpensively fabricating Light Emitting Diodes (LEDs). A potentially good solvent for Ge LPE is Pb. As a group IV element Pb does not dope Ge. It can be obtained in rather pure form, but further purification is necessary. The Pb solubility in solid Ge is low and does not lead to precipates, strain, or increased dislocations.

LPE has specific advantages over other techniques such as Molecular Beam Epitaxy (MBE) and Chemical Vapor Deposition (CVD). During the LPE process, most impurities are incorporated in the solid at a concentration which is lower than in the liquid. This segregation effect is significantly less pronounced in gas to solid interfaces as they exist in CVD. An approximation was developed for estimating segregation coefficients depending on the saturated impurity concentration in the solvent.(Rosenburg and Riveros 1974) For an impurity A the segregation coefficient between the solid Ge and the Pb solvent is given by equation 2.5 where $X(A_{Ge})$ is the mole fraction of impurity A in Ge.

$$k_{eff} = \frac{X(A_{Ge}) / X(Ge_{Ge})}{X(A_{Pb}) / X(Ge_{Pb})} \approx \frac{X^{Sat}_{GePb}}{X^{Sat}_{APb}} \tag{2.5}$$

The implications are that if A dissolves well in the Pb solvent, it will not incorporate into the Ge solid, which is intuitive. The more surprising result is that segregation coefficients will be smaller for a more dilute system $X(Ge_{Pb})$. For impurities that dissolve completely in Pb, the segregation coefficients will be less than 2% at 650°C. By using phase diagram information for the saturated impurity A concentration in Pb, $X^{sat}(A_{Pb})$, segregation coefficients can be determined. Of the group V and III elements As, Sb, Bi, and In lie approximately near 1% at 650°C. The temperature dependence of this relationship is shown in Fig. 2.12 for some group III and V dopants. Only Ga and Al deviate to higher values, 2.5% and 80% respectively near 650°C. There exists very little information about the interactions of Pb with B or P.

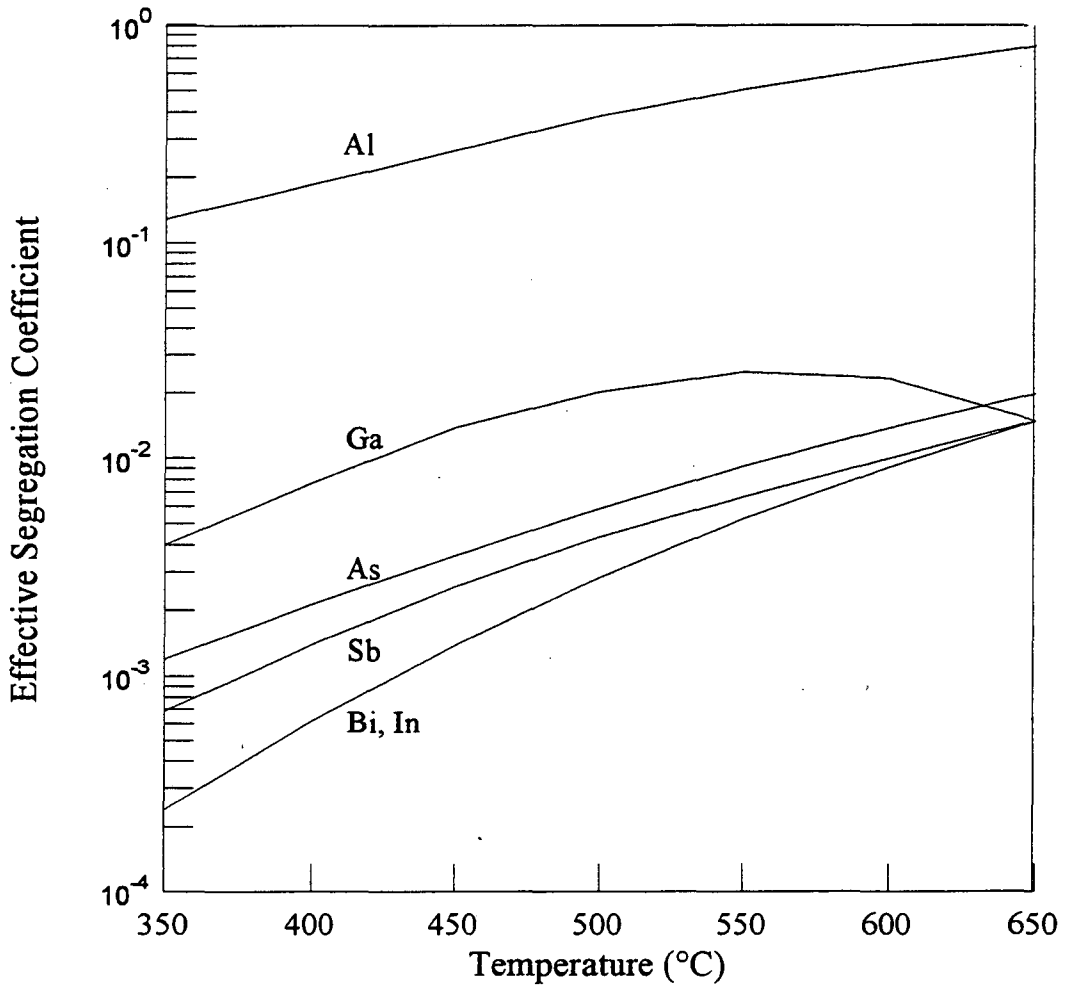

Fig. 2.12. Calculated effective segregation coefficients for Pb-Ge system.

2.1.5 Tipping Method

The LPE tipping method was chosen to be most appropriate for high purity growth. LPE of semiconductors has been performed with a number of different approaches. Researchers have used the sliding boat and dipping methods for introducing the saturated solvent to initiate growth. The sliding boat technique has been known to scratch substrate surfaces.(Saul and Roccasecca 1973) For tipping, the growth cycle is initiated and terminated by tipping the solvent on and off of the substrate. A cross

sectional schematic of the crucible design and tipping process is shown in Fig. 2.13 and 2.14 respectively

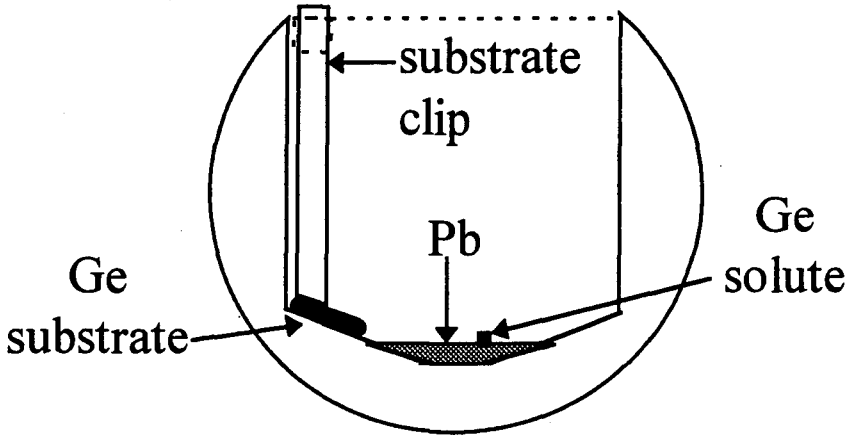

Fig. 2.13. Schematic cross section of graphite crucible with Pb solvent.

A graphite clip holds the substrate in place during the tipping procedures and protects approximately 10% of the substrate for later determining the epilayer thickness. The Ge solute charge is dissolved while the solution is not in contact with the substrate (Figure 2.14 left) and growth is initiated by tipping the crucible 80 to 90° counter clockwise to pour the solvent onto the substrate.(Figure 2.14 right)

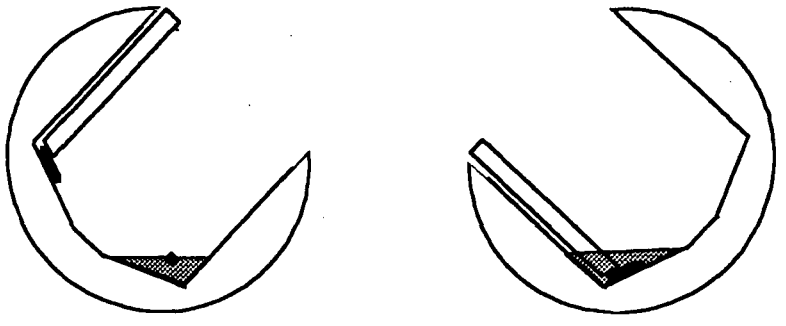

Fig. 2.14. (left) Dissolution of Ge solute charge. (right) Initiation of epitaxial growth.

2.2 Review of Ge LPE Research

Some of the first transistors and diodes were made by alloying Ge and Si with a molten metal such as In for p-type doping.(Hall 1952) H. Nelson (1963) explored the Ge LPE system for manufacturing tunnel diodes and GaAs LPE for lasers. Nelson showed that LPE could produce single crystal films with very low dislocation densities. Characterization of the epilayers was limited to the dislocation density, Laue X-ray, and resistivity measurements. Immorlica and Luddington (1981) grew Ge epilayers from a Pb solvent on GaAs substrates, but residual impurity concentrations were above 10^{17} cm^{-3}. Growth of Ge on GaAs substrates will always be impure, because the Ge-Pb solution is not in equilibrium when it comes in contact with the substrate; thus the substrate will be dissolved generating copious quantities of Ga and As, both shallow dopants. Other researcher have also limited their work to fabricating doped p-n junctions. Germanium has been grown from Ga, In, Al, Au, Sn, As, Sb, Pb, Cd, Bi, and combinations of their alloys.(Keck and Broder 1953; John 1958; Spitzer, et al. 1961; Kijima, et al. 1970) Most of these metals are dopants in Ge and are not compatible with high-purity growth.

Until this work, LPE had not been used for high purity elemental semiconductor growth, because the solute incorporates into the epilayer. Researchers have grown Si out of Ga or In solutions resulting in moderate to heavy doping. (Konuma, et al. 1993) Bi, a shallow donor in Ge, was hypothesized to have a low solid solubility (10^{13} to 10^{14} cm^{-3}) in Ge below 650°C extrapolated from higher temperature solubility data.(Hall 1952) Ge LPE growth was attempted with high purity Bi solvents, but free electron concentrations were always in the 10^{16} cm^{-3} for films grown at a temperature 650°C, so this solvent was

discontinued in this work. Both Sn and Pb are isoelectronic with Ge, but Sn is incorporated into the epilayer at $2x10^{20}$ cm^{-3}, which causes a lattice parameter increase and strain.(Trumbore 1956) Pb is the ideal choice, because of its low solubility in the Ge epilayer at growth temperatures of 650°C. Very little solubility data exists on Pb in Ge. Only one solubility value has been measured from a crystal that was grown by a thermal gradient across a Pb solution. The solubility at 805°C was $3.9x10^{17}$ cm^{-3}.(Trumbore 1960) The solubility was extrapolated to lower temperatures with the segregation coefficient of $1.7x10^{-4}$.(Trumbore 1960) At 650°C, the solubility is estimated to be $6x10^{16}$ cm^{-3}. Neither Secondary Ion Mass Spectroscopy (SIMS) nor X-ray fluorescence techniques were able to detect any Pb in a Ge epilayer film grown for this work. The SIMS measurement was limited due to the lack of a calibrated standard of Pb in Ge. The X-ray fluorescence had an approximate detection limit of 10^{17} cm^{-3}, so the Pb concentration was determined to be below this. Pb in a matrix of Ge is difficult to observe, because of the $L\alpha$(Pb) fluorescence line at 10.55 keV falls in-between the $K\alpha$(Ge) line at 9.88 keV and $K\beta$(Ge) at 10.98 keV.(Culity 1978)

2.3 Growth Procedures

LPE epitaxial growth has been performed in the Pb-Ge system. Preliminary research was done in a silica tube furnace with a graphite crucible and purged with a N_2 + 4% H_2 reducing atmosphere. For the control of oxygen contamination and purity, a silica growth chamber with a vacuum system was designed and built specifically for Ge LPE. The new growth chamber was designed and fabricated by the author. The system allows tipping of the solution without any rotating or sliding seals. All materials in the growth

chamber were chosen to be compatible with pure Ge and to be able to achieve impurity concentrations in the parts per billion range. The silica tube and associated vacuum system all rotate together along the silica tube axis. A schematic of the LPE growth system is shown in Fig. 2.15.

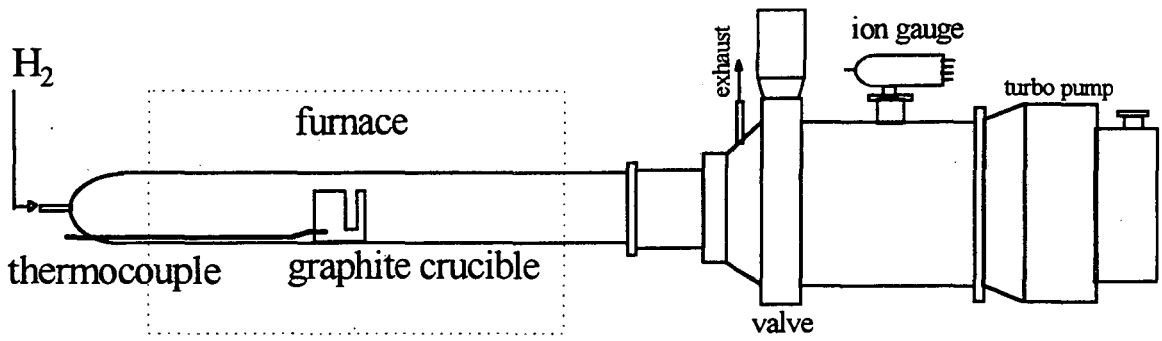

Fig. 2.15. Schematic of Ge LPE Growth Chamber

The furnace in which the growth takes place is 36" long to ensure a sufficiently long, flat temperature profile in the center. Silica baffles are spaced at 6" distances along the length of the silica tube with 3 baffles on the gas input side and 3 on the exit side. The exit baffle has an additional disc that holds the graphite crucible and allows insertion and removal of the crucible. The 52" silica tube[1] was configured in a simple design to allow easy cleaning with 5% HF. A 6 mm diameter silica tube protects the internal environment from the type K thermocouple that is inserted into the graphite crucible. All vacuum associated parts have been fabricated out of stainless steel and were cleaned with acetone and methanol. ISO flanges[2] were used as vacuum seals with viton o-rings[3]. A Varian

[1] Semiconductor grade GE 214 silica tubes from G.M. Associates, Oakland, CA.
[2] ISO-NW63 flanges from MDC Hawyard, CA
[3] From Bay Seal Co. Hayward, CA.

Turbo V-250 MacroTorr[4] pump has been used with a VAT[5] Series 20 high vacuum valve. The pumps base pressure was $2x10^{-7}$ torr and the system together reaches a base pressure of $1x10^{-6}$ torr. The turbo pump, vacuum ion gauge, and high vacuum valve are suspended on an aluminum base with wheels to allow access to the silica tube. Nupro regulating 4BMRG valves[6] were used to control the flow of Ar and H_2. A 0.1 μm filter was placed on the Ar inlet to remove particulates. A Nupro 4C poppet check valve[7] was used on the exhaust side to hold vacuum but open under 1/3 psi overpressure. With the check valve the system always runs under positive pressure. It was necessary to introduce a 1.5 μm filter upstream of the check valve to remove Pb vapor in the gas stream that condensed on the o-ring of the check valve. This particulate condensation prevented the check valve on the exhaust side from sealing under vacuum. After the check valve, a flow meter was positioned to monitor the gas exiting the system. The gas manifold was constructed with 304 SS tubing with VCR metal gasket butt welds at connection points. The VCR gaskets were stainless steel with a silver coating to prevent galling. The tubing was cleaned with acetone and methanol and heated under vacuum to degas residual impurities on the inner surface. Tubing at rotation points was connected with stainless steel bellows of 24" length to allow for tipping of the solution and movement of the vacuum system platform. Connection at the silica gas inlet was with a Cajon Ultra-Torr[8] elbow with viton o-rings.

---

[4] Varian 969-9007 Turbo pump, Lexington, MA.
[5] Vatterfly stainless 20040-PE04 valve, VAT Inc., Woburn, MA.
[6] SS-4BMRG-VCR metering valve from Oakland Valve and Fitting, Concord, CA.
[7] Nupro SS-4C-VCR-1/3 poppet check valve from Oakland Valve & Fitting, Concord, CA..
[8] Cajon Ultra-Torr SS-4-UT-9 from Oakland Valve & Fitting, Concord, CA.

Poco Graphite, Inc. machined and purified densified graphite (DFP-3-2)[9] crucibles with a high temperature (T > 1500 °C) and Cl_2 gas process to remove metallic impurities. Graphite crucibles, degassed in vacuum at 950°C in the growth chamber, were used to hold the growth materials. Ar gas (99.998%) was introduced at 950°C to clean the graphite surface after baking in vacuum. Pb solvents of 99.9999% purity were saturated with high-purity Ge under an atmospheric pressure of flowing H_2. Pb charges were prepared by removing PbO with dilute HNO_3, followed by a rinsing with distilled H_2O, dilute HCl, distilled H_2O, and finally distilled methanol. A N_2 jet was used to blow dry the Pb charge. The HCl was used to reduce the Cu concentration introduced by the HNO_3 solution. The effectiveness of this HCl treatment step was verified by comparing Cu concentrations in ultra-pure Ge substrates after LPE growths using different Pb etching solutions. Ge solute charges were cleaned by a 4:1 HNO_3:HF etch, distilled H_2O rinse, 4:1 HNO_3:HF etch, distilled H_2O rinse, 5% HF solution, and distilled H_2O rinse. Ge substrates were prepared by chemo-mechanical polishing with 7:3:1 H_2O: collodial silica (Syton):H_2O_2 to achieve an optically flat surface. Polished Ge surfaces have a flatness of less than 20 nm height change over 1 mm, which corresponds to a substrate radius of 25 meters. (Knowlton 1995) Substrate orientation was not actively controlled, but substrates were cut from crystals oriented in the [111] direction within approximately 0.2° estimated from the crystal mounting and cutting process. Before growth, substrates were solvent cleaned (kerosene ~70°C 3 min., acetone ~55°C 3 min., methanol 70°C 3 min.), etched 10 seconds with 20:1 HNO_3:HF, distilled H_2O rinse, 5% HF solution, distilled H_2O rinse, and

[9] Poco Graphite, Inc., Decatur, TX

rinsed with distilled methanol. Substrates were blown dry with a N_2 jet. The 10 second etch was added to remove any surface damage due to the chemo-mechanical polishing.

Growth materials were loaded into the graphite crucible and immediately inserted into the growth chamber. The chamber was sealed and pumped and purged twice with Ar gas(99.998% pure). The chamber was heated to 300°C and pumped to a vacuum of $3x10^{-6}$ torr to drive off any water vapor and to verify the integrity of the vacuum seals. The high vacuum valve was closed and ultra-pure H_2 from a Pd-diffusion cell was introduced at a flow rate ~0.6 L/min. The thermal growth cycle is shown in Fig. 2.16. The growth chamber was ramped to 650°C and held for 6 to 8 hours to dissolve the Ge charge into the Pb solvent. The temperature was reduced at a linear rate of ~0.3°C/min. At an undercooling of a 1-3°C, the solvent was tipped onto the substrate. When the chamber has reached a temperature of 340°C, the solvent was tipped off the substrate to terminate growth. H_2 gas was turned off and Ar introduced to purge the chamber. Residual Pb on the epilayer surface was removed with a 1:1 Acetic acid:H_2O_2 solution.

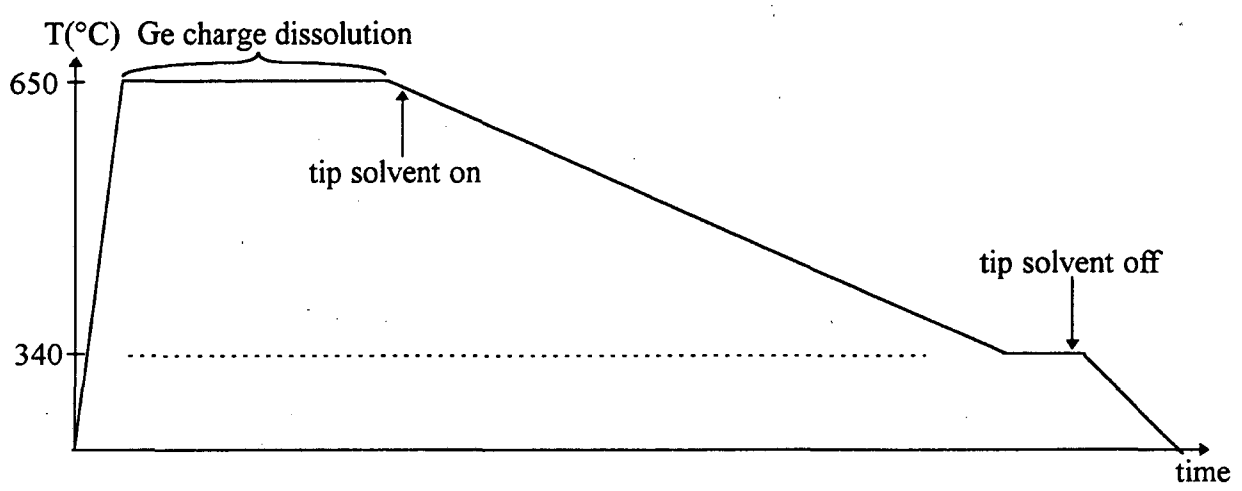

Fig. 2.16. Thermal growth cycle for Ge LPE epitaxy.

2.4 Epilayer Characterization

Epilayer thickness was determined with a Zeiss optical microscope to within ±2 μm. By comparing the focal distance of the epilayer to that of the substrate, the thickness was measured. A portion of the substrate was protected by a graphite clip during growth to allow the thickness measurement. Hall effect and resistivity were used for determining the residual impurity type, the free carrier concentration, and the Hall mobility. Hall effect measurements were performed at 77 K to characterize each epilayer. At 77 K, intrinsic carriers are negligible and the free carrier concentration is mainly due to shallow dopants. Those layers with low electrical impurities have been measured with Variable Temperature Hall Effect (VTHE) from 300 K to 5 K to determine majority and minority impurity concentrations and shallow level ionization energies. A more detailed description of Hall effect is given in Appendix A.

In order to identify the specific impurity or impurities present in the various layers a spectroscopic technique, Photothermal Ionization Spectroscopy (PTIS)(Lifshits and Ya Nad' 1965) was used. Briefly, the PTIS technique is based on a two step ionization process. In the first step, an electron (hole) bound to a donor (acceptor) is excited by a photon from its ground state into a bound excited state. A temperature is chosen such that phonons effectively assist ionization of the carrier from the bound excited state into the conduction (valence) band. The characteristic energies for the ground to bound excited state transitions identify the specific impurity with great accuracy (±3 μeV).(Kahn 1986) The photoexcitation is performed with a Fourier transform infrared spectrometer.(Bell 1972) A Michelson interferometer is used with a chopped IR mercury arc lamp. IR

photons travel through polished and evacuated brass light pipes to the sample. The ac signal is measured with a lock-in amplifier. The Fourier transform spectrometer is discussed in more detail in Appendix B. This method described so far only measures majority dopants. When band-edge light is shown onto the crystal free electrons and holes are generated.(Lifshits, et al. 1968) The free carriers are trapped by majority and minority impurities. These neutral acceptors (donors) generate free minority carriers through the PTIS process. The minority carriers decrease the conductivity by recombining with majority carriers in the sample creating negative peaks in the photoconductivity spectra. This technique has been well developed for identifying impurities in Ge.(Haller and Hansen 1974a) Further details on the PTIS technique are given in Appendix C.

A summary of the Ge epilayers grown by LPE and their 77K Hall effect results are in Appendix D. The characterization results for the Ge epilayers will be discussed in the next chapter.

The structural quality of the epilayers was determined by dislocation decoration etching and x-ray diffraction (XRD) measurements. The XRD rocking curves were recorded with a Siemens D5000 high resolution diffractometer.

3. Epitaxial Growth Experiments with Pb solvent

3.1 Structural Properties of Ge Epilayers

The Ge epilayers were characterized for their structural properties with several techniques. Preferential etching with a ferricyanide solution formed pits where dislocations intersect the (111) surface.(Holmes 1962) The dislocation density was determined by counting the triangular etch pits in a given area and multiplying by 4. This correction of four is performed because the dislocations counted only intersected one of the four (111) planes in the diamond cubic crystal and we assumed that the dislocation orientations are evenly distributed in all directions. Dislocation densities were found to lie between 200 to 500 cm^{-2}. Such densities are very similar to substrate dislocation densities. This result implies that substrate dislocations intersecting the surface are grown into the epilayer, but that no significant dislocation multiplication or nucleation takes place.

XRD θ–2θ scans only revealed the (111) peak, which means that the epilayers are single crystal or polycrystalline having textured orientation. XRD rocking curves confirmed that the epilayer were single crystal of high perfection. The epilayer (111) reflection had a full width half maximum (FWHM) of 21.5 arcsec shown in Fig. 3.1, while the substrate reflection had FWHM of 13.3 arcsec.

In comparison FWHM values for the best Si homoepitaxy are 16.5 arcseconds.(Dommann et al. 1995) The broadening of the observed rocking curve peak may originated from inhomogeneous strain defects, such as dislocations, solute strains, stacking faults, or curvature of the wafer. The extra broadening of 8 arcsec beyond the substrate peak width corresponds to a strain of $\sim 10^{-4}$.

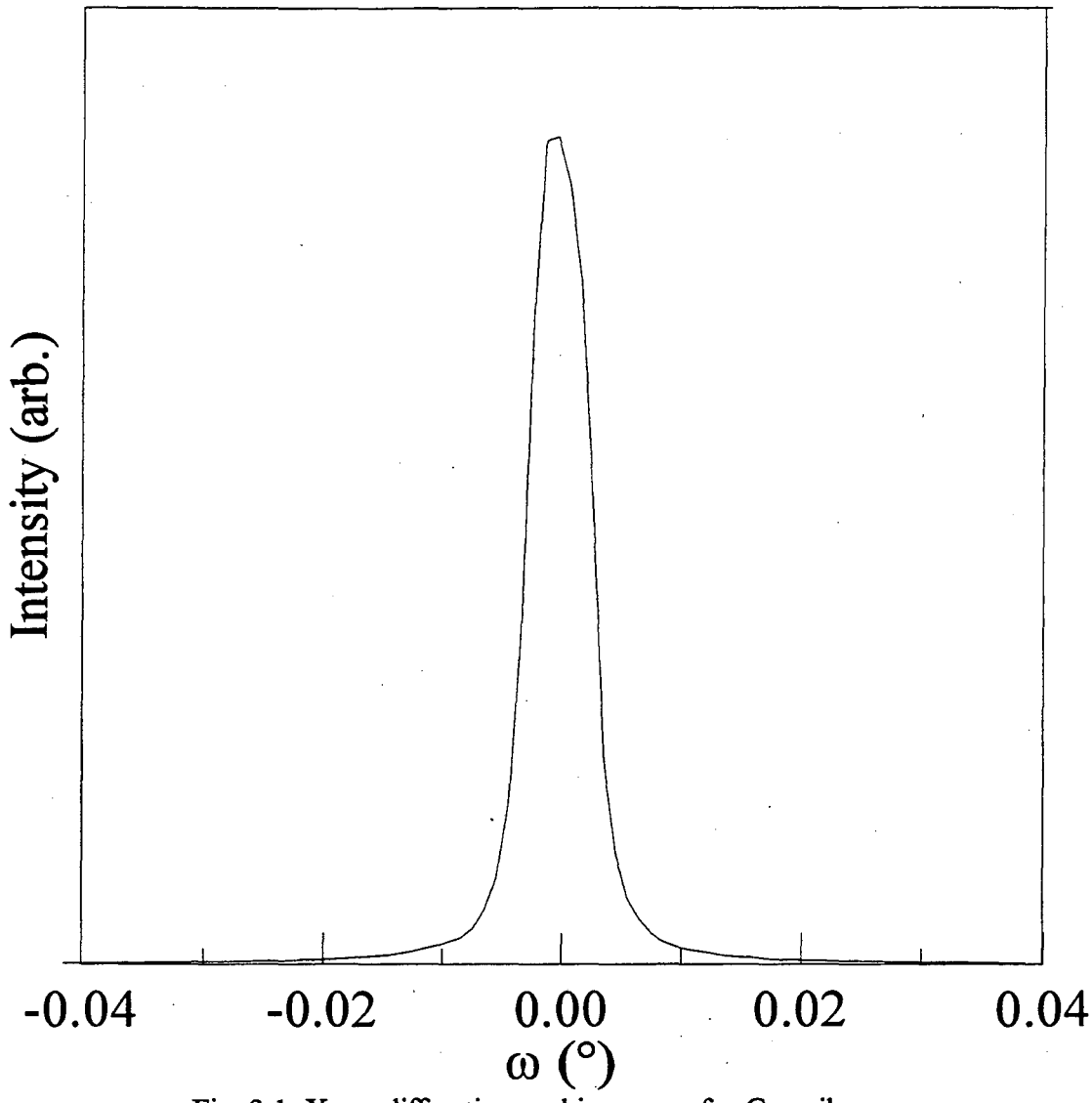

Fig. 3.1. X-ray diffraction rocking curve for Ge epilayer.

All of the previously listed defects have been excluded based on their concentrations, except for the curvature of the wafer. The bending of the wafer producing a strain of 10^{-4} corresponds to a radius of 109 meters, (Uschmann, et al. 1993) which is negligible and can be ignored for this application. Despite the observed broadening the epilayer can still be classified as high quality single crystal material. The minor structural imperfection was not anticipated to affect device performance.

3.2 Electrical and Optical Properties

Ge epilayers, grown from Pb solvents on high-purity substrates, have been characterized by variable temperature Hall effect and PTIS. In Fig. 3.2, the characteristic ground state to bound excited-state peaks identify the majority donors. They are phosphorus, bismuth, and antimony.

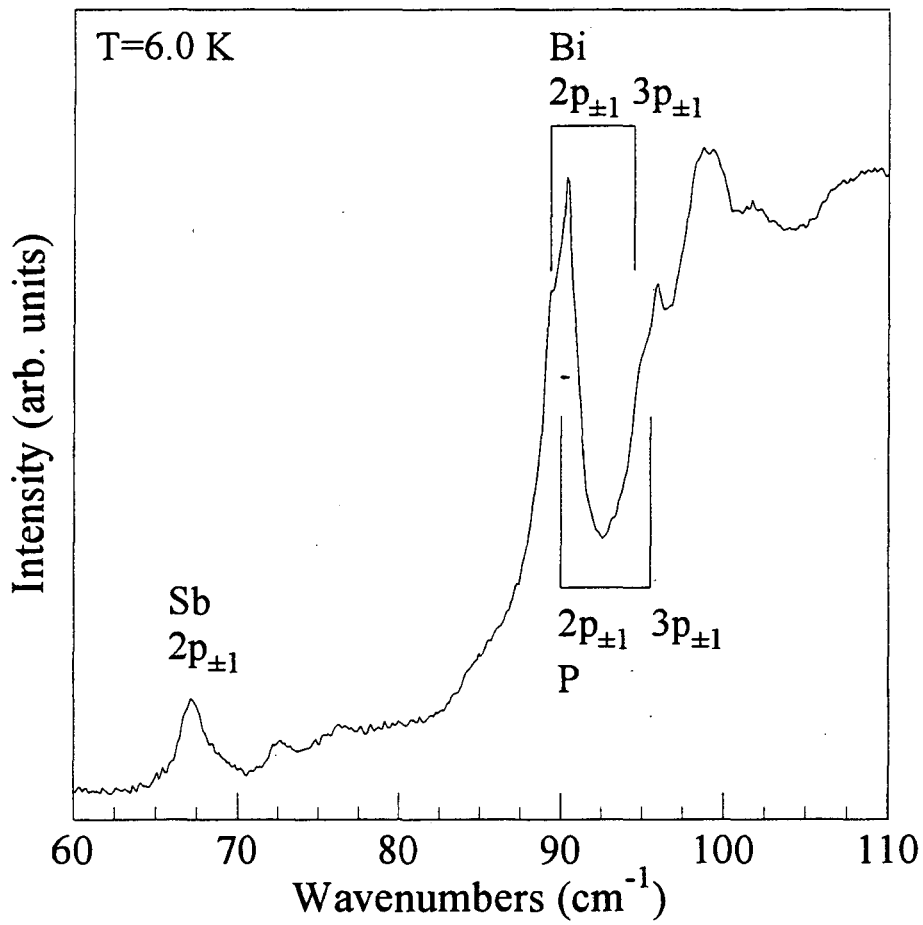

Fig. 3.2. PTIS of Ge epilayer grown from Pb(Alpha Aesar).

PTIS measurements detects only the impurities in the n-type epilayer, because it is electrically separated from the p-type substrate due to the formation of a depletion region at the epi-substrate interface(junction isolation). Through a series of carefully designed experiments using a number of crucibles and different Pb sources, the residual impurity

source has been determined to be the Pb solvent. Use of a silica crucible for Ge LPE resulted in the same contamination observed for growths in graphite crucible.

Five commercial sources of high purity Pb were investigated for LPE. The residual concentrations and the impurities from Ge epitaxial growth are summarized in Table 3.1. The separate identification of the phosphorus and bismuth PTIS lines was challenging, because their $2p_{\pm 1}$ lines lie only 0.56 cm^{-1} apart.(Ramdas and Rodriguez 1981) The presence of both P and Bi can be visually observed in Fig. 3.2 by marking the peak positions of the $2p_{\pm 1}$ and $3p_{\pm 1}$ lines.

Commercial Pb	Impurities in LPE Ge	N_D-N_A (cm^{-3})
Alpha Aesar[10] (99.9999%)	P, Sb, Bi	$8x10^{14}$
Aldrich[11] (99.9995%)	P, Sb, Bi	$4x10^{14}$
GFS Chemicals[12] (99.9999%)	P, Sb, As	$4x10^{15}$
Goodfellows[13](99.999%)	P, Sb, Bi	$8x10^{14}$
Cerac[14](99.9999%)	P, Sb, Bi	$4x10^{14}$

Table 3.1. Commercial High Purity Pb Sources.

The epilayers grown from Pb purchased from GFS chemical company, exhibited an As contamination which was high compared to the other commercial Pb sources. The PTI spectrum in Fig. 3.3 clearly shows the As lines which are not present in other spectra. This Pb from GFS was reported to have been zone refined for purification, but it turned out to be the least pure of all the commercial sources!

[10] Alpha Aesar, Stock #12511, Ward Hill, MA.
[11] Aldrich, Stock #26,593-4, Milwaukee, WI.
[12] GFS, Stock #A4107, Powell, OH.
[13] Goodfellows, Stock #PB006020, Berwyn, PA.
[14] Cerac, Stock #L-1133, Milwaukee, WI.

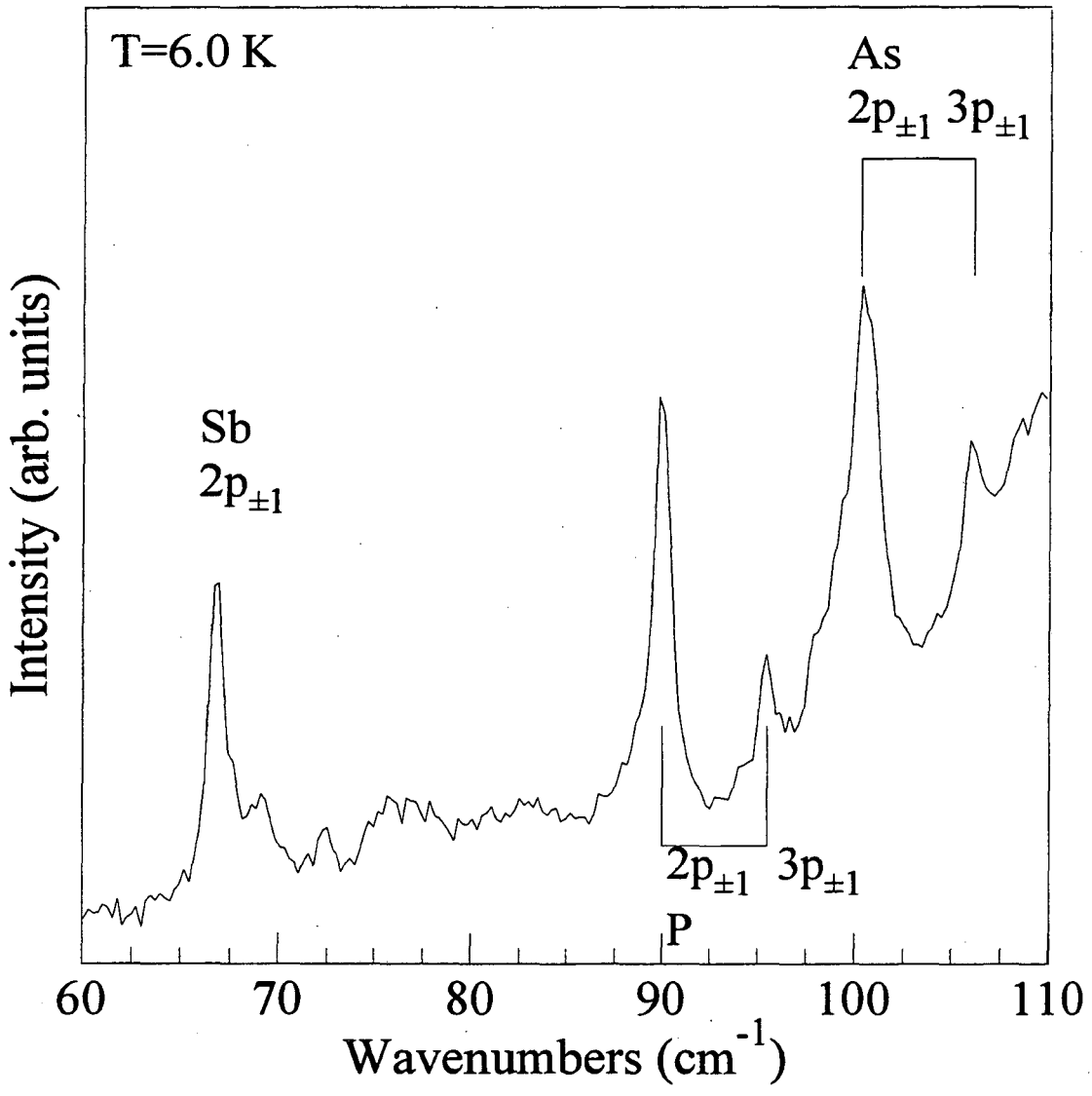

Fig. 3.3. PTIS of Pb (GFS) grown Ge epilayer #179.

The variable temperature Hall effect measurement shown in Fig. 3.4 gives a residual donor impurity concentration of $4x10^{14}$ cm^{-3} and minority acceptor impurity concentrations of $4x10^{12}$ cm^{-3}. As identified from PTIS, the LPE layer #180 contains three shallow donors with ground state energies of 12.88 meV for Bi, 12.81 meV for P, and 10.31 meV for Sb.(Reuszer and Fisher 1964) The theoretical fit is restricted to one majority donor impurity with an average donor binding energy of 12 meV. This may

explain the discrepancy between the fit and the data at the lowest temperatures, where the shallowest donor Sb dominates.

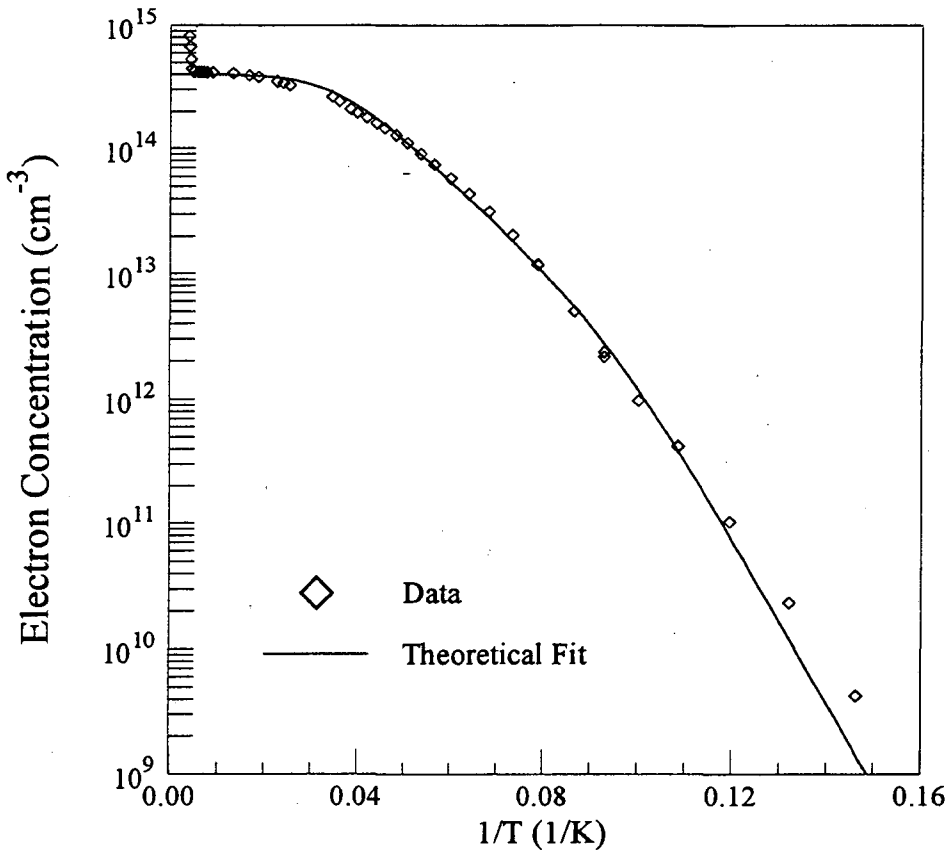

Fig. 3.4. Variable temperature Hall effect of LPE Ge layer #180.

From the value of the resistivity ρ and the free carrier concentration n, the mobility μ can be calculated for each of the measurements assuming a Hall factor of 1.

$$\mu = \frac{1}{ne\rho} \tag{3.1}$$

In Fig. 3.5 the Hall mobility of an epitaxial Ge layer is compared to bulk grown Ge of similar majority concentration $4\text{x}10^{14}$ Sb cm^{-3} and a minority concentration $5\text{x}10^{11}$ cm^{-3}. At low temperatures (T < 10 K), the drop in the epilayer's mobility is due to a larger

ionized impurity scattering caused by compensation which is higher than in the bulk Ge. At higher temperatures (T > 25 K), the epilayer mobility is lower than the bulk.

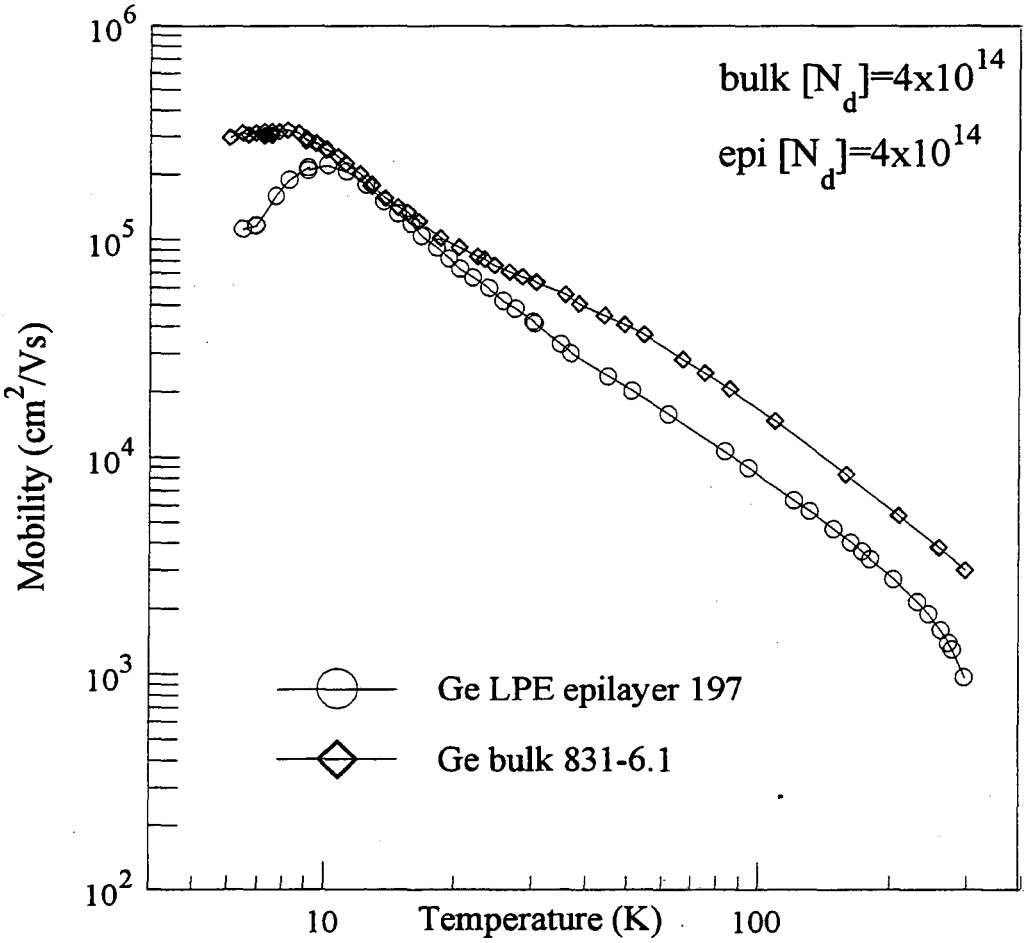

Fig. 3.5. Mobility vs. temperature for bulk and epitaxial Ge.

This same decrease in the epilayer mobility compared to bulk mobility of pure Ge is also evident in Fig. 3.6. A random distribution of Pb could deform the conduction band and increase scattering thus lowering the mobility.

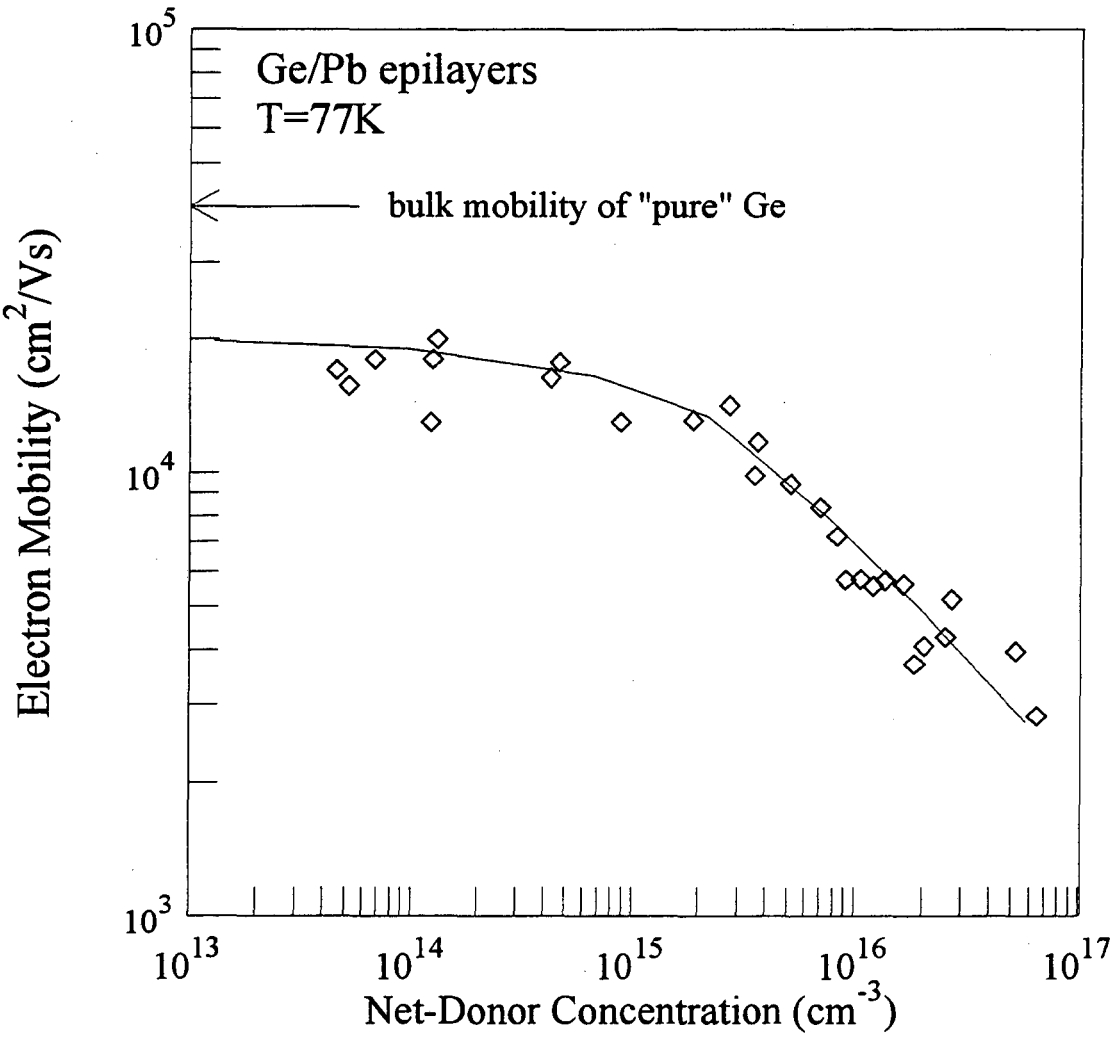

Fig. 3.6. Dependency of epilayer mobility on net-donor concentration.

Nathan et al. (1961) showed that the electron mobility drops by 50% at a hydrostatic pressure of 22 kbar. The covalent bond length for Pb is much larger than for Ge, inducing a local strain. The neighboring Ge atoms move away from the Pb substitutional atom and the more distant Ge atoms move less. Kraut and Harrison (1985) predicted the distortion and relaxation for isovalent substitutional impurities in tetrahedrally coordinated semiconductors and determined a Sn-Ge bond length of 0.256 nm for Ge:Sn. The covalent bond lengths of Sn (0.28 nm) and Pb (0.292 nm) are closer

to each other than to Ge (0.244 nm). An approximate Pb-Ge bond length of 0.26 nm was extrapolated from the Sn-Ge bond length. This results in a strain of 0.066 and a stress of 49 kbars, determined from the bulk modulus of 7.5×10^5 bars. The stress of 49 kbars shifts the conduction band by 150 meV locally near the Pb atom.(Balslev 1966) This deformation in the conduction band is much larger than thermal fluctuations, 4.3 meV, at 100 K and thus could scatter electrons and decrease the mobility as observed by Nathan et al. (1961).

In Fig. 3.6, we see the dependence of the mobility for many Ge epilayers on the net-donor concentration. The mobility values were calculated from the results of resistivity and Hall effect measurements performed at 77 K. The vertical spread in the mobility at a given concentration is representative of the fluctuations in crystalline quality assuming the compensation is low. This mobility dependence on net-donor concentration was obtained as epilayer purity improved due to continued growths and purification steps. These improvement are summarized in Fig. 3.7.

The first 98 epilayers were grown in a furnace tube purged with 4%H_2 & N_2 with Sn, Bi, and Pb solvents. A new growth chamber was designed and built by the author described in section 2.3 of this dissertation. Improvements between the two systems quickly lead to enhanced epilayer purity. Some of the improvements were caused by switching from 4% H_2 to 100% H_2, changing from a purged growth tube to a vacuum tight apparatus, addition of a vacuum system to degas growth materials, and using new commercially manufactured and purified graphite crucibles.

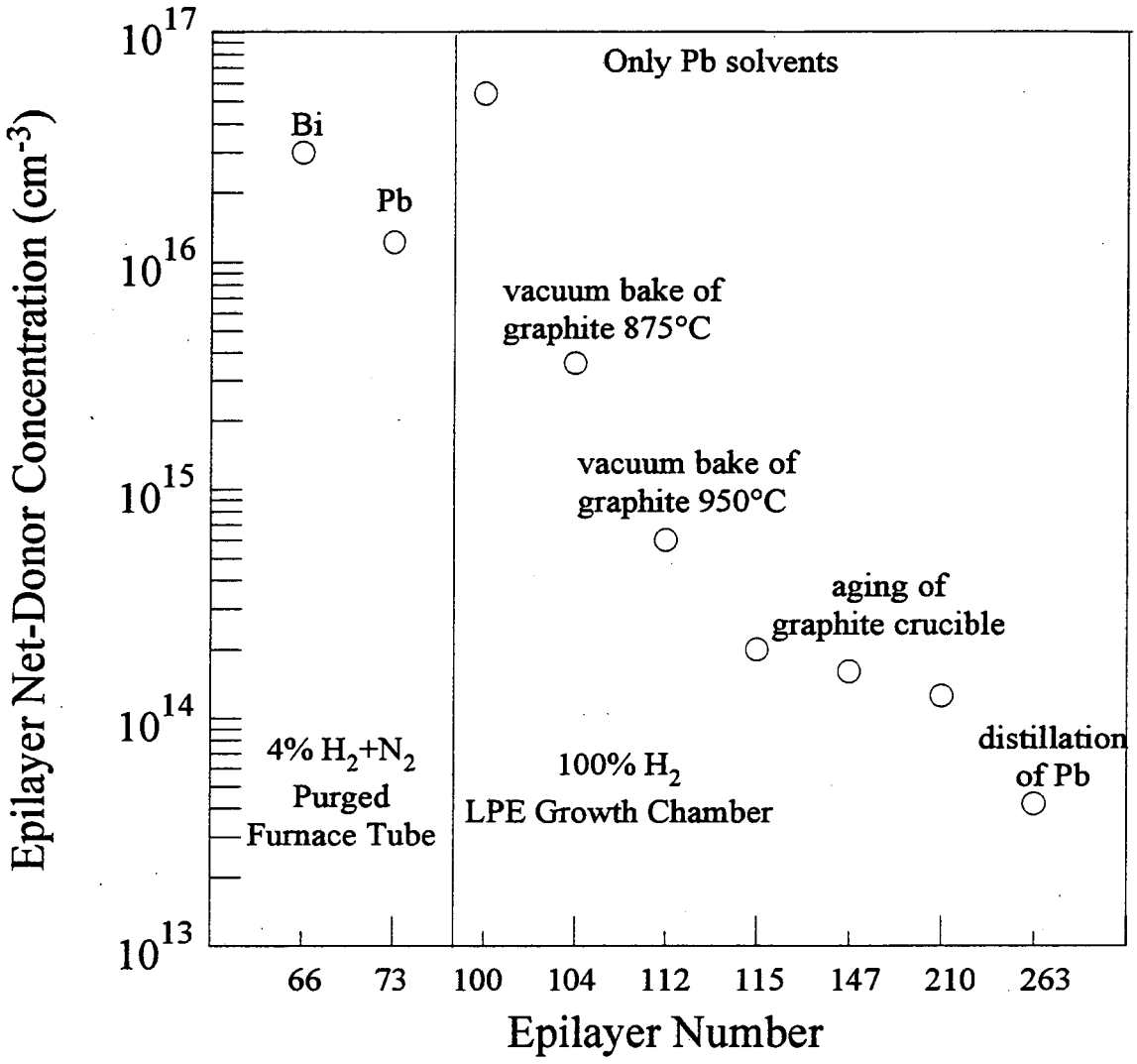

Fig. 3.7. Representation of improvements in epilayer impurity concentration.

Purification of the graphite crucible by vacuum baking at 950°C made the most dramatic improvements in the initial growths. For the growths 115 to 175, the crucible "aged" during which impurities were leached or driven out of the crucible. During this period, small improvements in the donor concentration and larger improvements in the acceptor impurity concentration were observed. The 77K Hall effect results on epilayers 100 through 150 alternated between n and p type. Epilayers 129 through 137 were

intentionally doped with Ga to fabricate p-type IR absorbing layers for BIB detectors. This effort was not successful, because the residual donor impurity concentration of ~$4x10^{14}$ cm^{-3} was too high. This Ga introduction to the crucible was slowly leached out over multiple growths and vacuum baking of the graphite crucible. The Ga concentration in the epilayers was monitored by performing variable temperature Hall effect (VTHE).

Epilayer #	Acceptor Concentration
125	$7x10^{13}$ cm^{-3}
180	$4x10^{12}$ cm^{-3}
197	$1x10^{12}$ cm^{-3}
208	$3x10^{11}$ cm^{-3}

Table 3.2. VTHE results on undoped Ge epilayers

In Table 3.2, the results of these VTHE measurements are summarized on undoped epilayers. Improvements can be seen for many growths runs over a period of time. Graphite growth crucibles were baked at 950°C for 8 hours at a time in vacuum ($1.5x10^{-6}$ torr) to remove all unintentional impurities. Between epilayer #100 and #270, the graphite crucible was vacuum baked 28 times resulting in an acceptor concentration as low as $3x10^{11}$ cm^{-3}. This improvement in the epilayer acceptor concentration is attributed not only to the many vacuum baking cycles of the crucible but also to the fact that the segregation coefficient for Ga is very close to unity. A high segregation coefficient leads to successful leaching of the Ga from the crucible. This result suggests that the commercial 99.9999% pure Pb is very low in acceptor impurities, but unfortunately still contains too many group V impurities.

3.3 Pb Purification for Ge LPE growth

3.3.1 Vaporization and Oxidation

Residual impurities in the Pb solvent dominated the epitaxial growth for nominally undoped Ge LPE growth runs. For this reason, purification of Pb was undertaken to remove the residual impurities before Ge crystal growth was performed. The first and simplest technique used to purify the Pb solvent was vaporization of the impurities.

Element	Vapor Pressure
Pb	$3x10^{-3}$ torr
Bi	$2x10^{-2}$ torr
Sb	$5x10^{-1}$ torr
P	$\sim 10^{+5}$ torr

Table 3.3. Vapor pressure of selected elements at 700°C.(Nesmeianov 1963)

From the PTIS results, the impurities were determined to be Sb, P, and Bi, all of which have vapor pressures higher than Pb in their pure state. The vapor pressures at 700°C are listed in Table 3.3 for the Pb and the major impurities in the high purity Pb. Pb solvents were baked at temperatures between 700 to 850 °C in H_2 prior to loading of the Ge charge and substrate. Epilayer purities only dropped from $4x10^{14}$ to $2x10^{14}$ cm^{-3}. The impurities do not evaporate, because their vapor pressure is dramatically suppressed due to their dilute presence in the solution ($X_i \sim 10^{-7}$). Raoult's law states that the vapor pressure P_i is reduced by the mole fraction of the impurities X_i compared to the pure state. Therefore, the impurities in solution have a lower vapor pressure than the Pb.

During metallurgical processing of Pb, the oxides of Sb, Bi, and As are known to rise to the surface at which time they are removed as slag. Using this knowledge, Pb solvents were heated to 850°C in Argon gas with a purity of 99.998%. The residual gas in

Ar is typically O_2 which was used to oxidize the impurities. The best epilayer purities dropped from $4x10^{14}$ to $1.2x10^{14}$ cm^{-3}, but the purification effect wasn't consistent. At 800°C, the diffusion coefficient for Sb in Pb is estimated to be $2x10^{-4}$ cm^2/s from the data in Fig. 2.8. In a 5 hour cycle at 800°C, Sb has a diffusion length $x = (Dt)^{1/2}$ 1.5 times greater than the distance across the solution, so the evaporation is not diffusion limited. My hypothesis is that in a dilute solution, very few of the impurities are at the surface. For every one impurity atom at the surface, there are $3x10^4$ impurities in the bulk of the solution. This moderate improvement in Pb purity prompted other methods to be tried to obtain larger purification.

3.3.2 Zone Refining

Zone refining appeared to be a suitable purification process to achieve efficient purification in our research laboratory. (Lawley 1968) A Ge zone refiner was converted for purification of Pb. Pb liquid is less dense than the Pb solid, which is the opposite for Ge. To accommodate for this difference, the zone refiner must be tipped in the opposite direction to prevent mass transport down the Pb bar, which can become significant over many passes. The angle θ at which the zone refiner is tipped depends on the length *l* of the molten zone, the height h of the solid and the ratio α of the density of the solid to that of the liquid.(Lawley 1968) For Pb, the ratio α is 1.066.

$$\theta = \frac{\tan^{-1}[2h(1-\alpha)]}{l} \tag{3.2}$$

Using equation 3.2 and 1 cm for h and 2 cm for *l*, θ becomes 3.8°. Experimentally, an angle of 1° to 2° resulted in a much more uniform bar. The GFS Pb was deemed the most

impure and therefore the most likely candidate for experimental purification. Zone refining was performed in a graphite crucible in silica under a 10% H_2 in N_2 atmosphere with a movable 5 kW radio-frequency (RF) heater. Approximated 50 passes were performed with a zone width of approximately 1 inch on a bar of 24 inches. Pb was cut from the head end and also one-third down the bar. Ge epilayers were grown from the selected Pb. The 77K Hall effect measurements revealed minute improvement in the residual impurity concentration from $4x10^{15}$ to $1.8x10^{15}$ cm^{-3}.

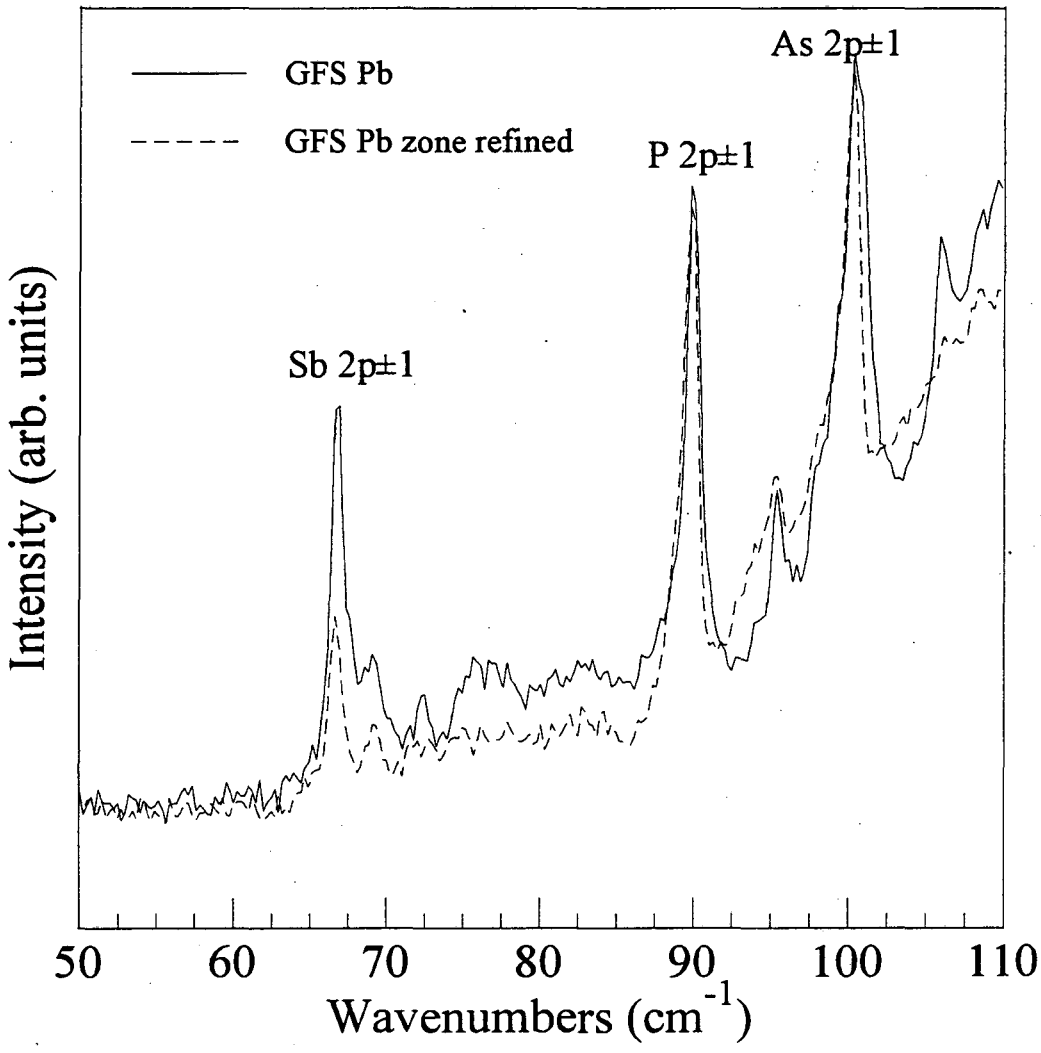

Fig. 3.8. LPE epilayers grown from GFS Pb with and without zone refining.

The PTIS of these epilayers in Fig. 3.8 reveals that the P and As concentrations did not change, but the Sb dropped by a factor of 2. This result was discouraging, therefore other purification techniques were attempted. The low amount of segregation may be due to segregation coefficients being near unity. As an example, the segregation coefficient of Sn in Pb was reported to be 0.75 in the literature.(Rodway and Hunt 1991) From phase diagrams, Sb and Bi segregation coefficients are calculated to be near unity, 0.4 and 0.6 respectively. Only As should have a low segregation coefficient approximately 0.01, but we see from the PTIS results that the As did not segregate either. It is also possible that with these high vapor pressure impurities recontamination occurs through the gas phase.

Limited segregation may also be due to poor mixing of the molten zone, such that impurities do not redistribute from the enriched solute layer, of thickness δ, at the solid-liquid interface. Due to the low melting point of Pb, the molten zone was only slightly higher in temperature than the solid, thus leaving a relatively viscous molten zone. The effective segregation coefficient is affected by the freezing rate, f, and the solute diffusion coefficient, D. The effective segregation coefficient approaches unity with a low solute diffusion or a large freezing rate as shown in equation 3.3.(Burton, et al. 1953)

$$k = \frac{k_o}{k_o + (1 - k_o)e^{-f\delta/D}} \tag{3.3}$$

These poor results for zone refining encouraged us to use a different purification technique.

3.3.3 Distillation

Distillation of Pb was first attempted in a sealed silica ampoule (Fig. 3.9) evacuated to a pressure of 10^{-5} torr and exposed to a temperature gradient. The hottest end with the source Pb was heated to 1000°C with a 20°C temperature drop at the furthest end of the ampoule about 25 cm away. This temperature gradient was deemed too low and a gradient of 100°C over 25 cm was used.

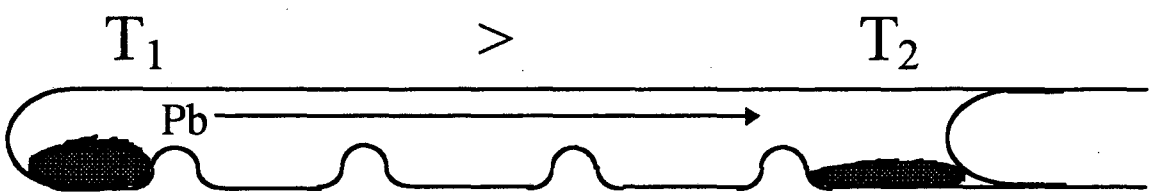

Fig. 3.9. Schematic of Pb Distillation in silica ampoule.

About half of the 50g of Pb (Cerac) was transported from the hot to cold end in approximately 100 hours. 10 g of Ge was added to further dilute the impurities in the source Pb. To reclaim the condensed Pb for use, the ampoules were cracked and placed in 49% HF solution to dissolve the silica off of the Pb. The condensed Pb was used in growing Ge epilayers and Hall effect measurements were performed at 77 K. The epilayer purity dropped from 4×10^{14} cm^{-3} achieved with the commercially available Pb to approximately 5×10^{13} cm^{-3}.

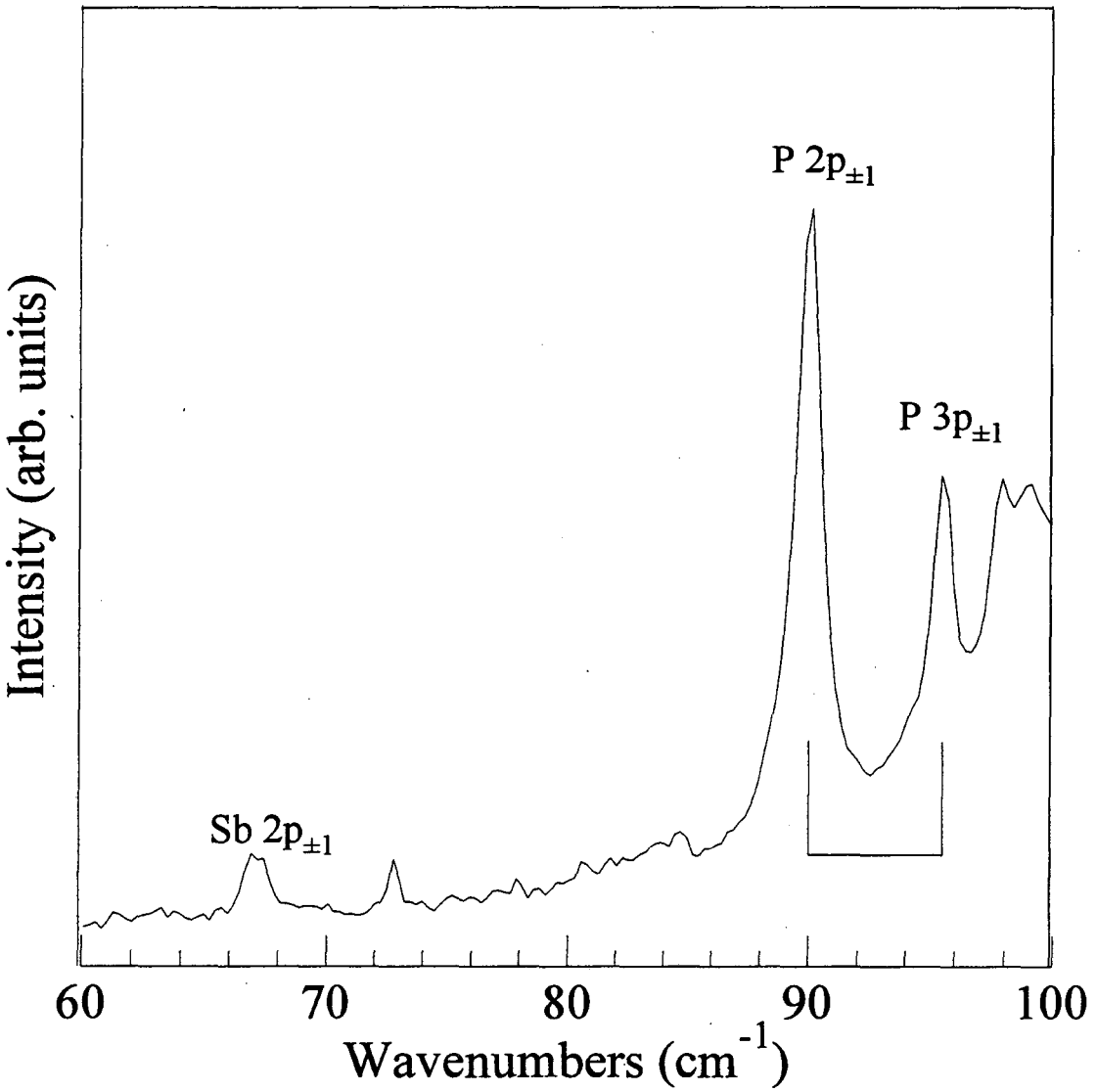

Fig. 3.10. PTIS of Ge epilayer #264 grown from Pb distilled in silica ampoule.

In Fig. 3.10, the PTIS measurement revealed that the Bi and Sb had been significantly reduced and that mainly the P contamination remained. Fig. 3.11 shows variable temperature Hall effect of Ge epilayer #264, which verified the low donor concentration, but revealed a rise in the acceptor concentration. It is possible that extensive handling resulted in acceptor impurity contamination.

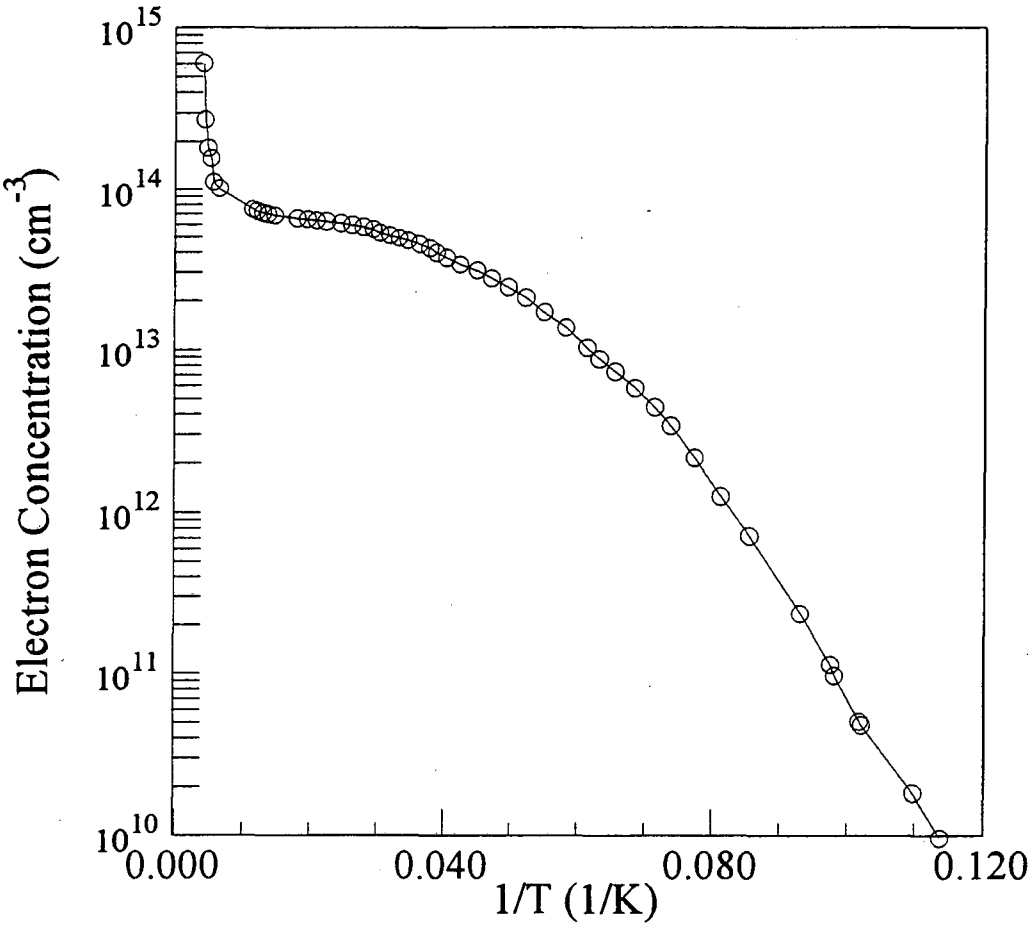

Fig. 3.11. Variable temperature Hall effect of LPE #264
N_D=3x10^{13} cm^{-3}, N_A~5x10^{12} cm^{-3}.

The long heating time and the time required to dissolve the silica from the Pb, prompted streamlining of the purification process such that many distillations could be accomplished to further improve the purity. Graphite was a much better material for condensing of Pb because of the lack of adhesion. The graphite components were machined and purified by baking in vacuum at 1000°C at a pressure of 1.5x10^{-7} torr. A schematic of the process is shown in Fig. 3.12. Pb (Cerac) was loaded into the left most graphite growth crucible and evaporated at 1000°C. The furthest to the right vessel was at 700°C±20°C and condenses the Pb. This container was machined to a very close fit

with the silica tube to prevent contaminating the turbo pump with Pb vapor. A silica rod was used to brace the right most container such that it does not slide during pumping of the chamber. The middle graphite cylinder was added to prevent condensation on the front face of the catch vessel, which had previously deposited Pb onto the silica tube. The Pb charge (~50 g) was loaded and was evaporated at approximately at 0.8 grams of Pb per minute at 1000°C.

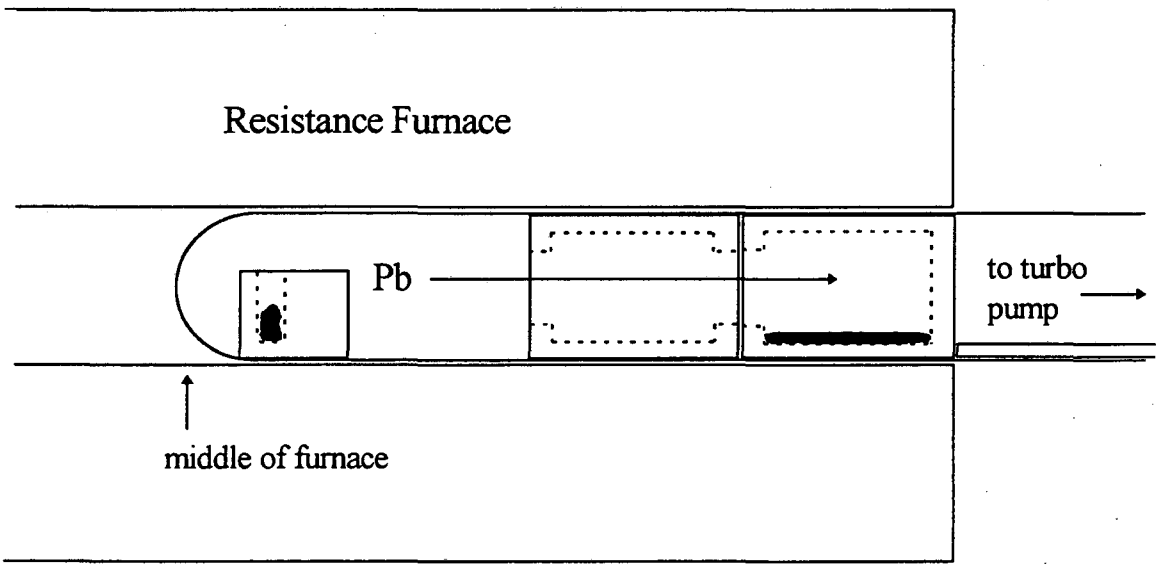

Fig. 3.12. Schematic of Pb distillation with graphite condensation receptacle.

Ge was used in the source end as a gettering and dilution agent. With the furnace at 950°C, the Pb transport rate was 0.55 grams of Pb per minute, and at 900°C, the Pb transport rate dropped to 0.4 grams of Pb per minute. Ge epilayers produced from twice distilled Pb had an impurity concentration of 7.6×10^{13} cm^{-3}. Collection with the catch basin moved deeper into the furnace, thus staying at a higher temperature, resulted in higher epilayer purities of 5×10^{13} cm^{-3}. At this higher temperature, the catch basin was out

of sight and we were unable to determine the temperature with a pyrometer. The higher purity may be attributed to less condensation of impurities at higher temperatures.

3.4 Impurity Segregation Study

To gain more information regarding purity control and to control doping from the liquid phase, segregation coefficients from the solvent to the epilayer have been measured. The Pb solvent was intentionally doped with Ga and a p-type Ge epilayer was grown from this solution. Hall effect was performed on the epilayer to determine the Ga concentration. The Gallium segregation coefficient has been determined at a concentration in Ge of 1.3×10^{17} cm^{-3} to be k=1.8. This segregation coefficient agrees with the deviation from the other impurities as predicted in section 2.1.4, even though the magnitude was not correct. This result implies that Ge epilayer growth is extremely susceptible to Ga contamination. Pb-Ga alloys were developed to dope epilayers for segregation coefficient measurements and for p-type BIB detectors.

Sb is an ideal dopant for n-type BIB detectors, because Sb has one of the shallowest binding energies 10.31 meV in Ge.(Reuszer and Fisher 1964) The Pb solvent was intentionally doped with 12.4 mg Sb giving a concentration of 7.7×10^{19} cm^{-3} in the liquid. The concentration of Sb in Ge was 2.4×10^{18} cm^{-3} leading to an effective segregation coefficient of 0.03. This segregation coefficient is nearly identical to the prediction in section 2.1.3. Due to the very small amounts needed to achieve appropriate Sb dopant concentrations in the 10^{16} cm^{-3} range, a master doping alloy of Pb and Sb was fabricated.

3.5 Master Doping Alloy

Initial epilayer impurity concentrations required for blocking layer formation were not achieved with Ge epilayers, but minority impurity concentrations were sufficiently low for the fabrication of doped IR absorbing layers. To achieve an impurity concentration of 10^{16} cm^{-3} in the Ge epilayers, 0.08 mg of Sb are needed to be added to 12 g of Pb solvent. This amount was unrealistic to add in a reproducible manner, so a master doping alloy of Pb and Sb had to be fabricated.

Master Pb-Sb alloys were fabricated with Sb concentrations near 0.2 at %. The first alloys were allowed to cool slowly. The dopant concentrations in subsequently grown epilayers fluctuated, which implied the Sb had segregated non-uniformly in the alloy, due to the eutectic at 17.5 at % Sb and 252°C.(Asktakala, et al. 1981) This led us to rapidly quenched the subsequent alloys.

A Pb-Sb(0.197 at. %) alloy was prepared in a graphite crucible inside a silica ampoule under 1/3 atm of H_2 gas. The alloy was homogenized at 700°C for 22 hours and quenched into ethylene glycol. The resulting growths had a segregation coefficient of approximately 0.03 at a 2.4×10^{16} cm^{-3} concentration in Ge. Fluctuations in Sb concentrations in the epilayers turned out to be due to Sb evaporating from the solvent during the growth process. Growths runs performed with longer dissolution times produced epilayers of lower Sb concentration. This evaporation effect was not reproducible between growth runs, such that it could be accounted for. This evaporation effect forces us to adjust our segregation coefficient estimates. To reduce evaporation in the future, epilayers should be grown at 600°C rather than 650°C. This should lower the

vapor pressure of Sb from 0.32 torr to 0.1 torr. (Nesmeianov 1963) Other techniques would include the use of a graphite cover on the crucible to reduce the evaporation further.

4. BIB Detector Fabrication and Characterization

4.1 Fabrication

Ge BIB detectors were produced in two types of configurations. The simpler technique was to grow epilayers as pure as possible on 10^{16} cm^{-3} doped substrates. The second technique was to grow doped epilayers in the 10^{16} cm^{-3} range on substrates of 10^{12} to 10^{13} cm^{-3} range. For this second technique, either Pb-Sb or Pb-Ga alloys were used to dope the epilayer from the liquid phase. The substrates which were used as blocking layers had to be mechanically thinned to within 40 to 80 μm of the IR absorbing layer. Due to problems with measurements of the epilayer thickness, blocking layer thickness were not necessarily optimum. To remove the substrate carefully, samples were first lapped with an Al_2O_3 #1900 grit slurry and then chemo-mechanically polished with 7:3:1 H_2O: collodial silica (Syton):H_2O_2 to achieve an optically flat surface parallel to the epilayer.

At this stage, degenerately doped contacts were formed by ion implantation for both techniques. To obtain p-type contacts, both sides were implanted with 33 keV $1x10^{14}$ B^+ ions /cm^2 and 50 keV $2x10^{14}$ B^+ ions/cm^2 at room temperature. The implanted contacts were activated by annealing at 330°C for 30 minutes. For n-type contacts, both sides were implanted with 40 keV $2x10^{14}$ P^+ ions/cm^2 and 100 keV $4x10^{14}$ P^+ ions/cm^2 at -167°C to form an amorphous layer. The n-type contact was activated through solid phase epitaxy by annealing at 450°C for 2 hours. The implanted layers were metalized with 40 nm Pd followed by 400 nm Au. On the blocking layer side, only half of the surface was metallized, to allow for illumination studies through the implanted contact.

The metal layers on the Ge detector were reacted at 300°C for 30 minutes to consume any surface oxide. Devices were cut to 1x2 mm^2 and etched to remove residual saw damage.

During a period when ion implants were not readily available, an alternative alloyed contact was developed. The contact was based on alloying with Sb as the sample was processed through the Ge-Au eutectic. A complete description of this process is given in Appendix F. Detectors with alloyed contacts were illuminated from the side.

4.2 Characterization

Ge far infrared BIB detectors were characterized using 3 main criteria. Detectors were evaluated for their spectral response, their responsivity at a specific frequency (110 cm^{-1}), and their dark current. Spectral response and dark current evaluations were used as the initial characterization tools to decide whether a responsivity measurement would be of added value. The detector characterization technique is described in Appendix E.

4.3 Performance

The first Ge BIB detector with extended spectral response was fabricated in the purged furnace tube under a forming gas 4% H_2 & 96% N_2 atmosphere. The success of this detector prompted the building of the Ge LPE growth chamber in which all other detectors were fabricated. At the time this detector was produced, undoped epilayer impurity concentrations ranged between $1x10^{15}$ to $2x10^{15}$ cm^{-3}. This concentration was too high for blocking layer requirements. Therefore, instead of growing blocking layers a $2.2x10^{16}$ cm^{-3} Sb doped IR absorbing layer was grown on a pure 10^{12} cm^{-3} As doped substrate. After growth the substrate layer was polished down to ~60 μm and implanted with P^+ ions to form metallic doped contacts as described previously. At low bias, the

spectral response of the Ge BIB detector in Fig. 4.1 mainly originates from the As doped blocking layer. Arsenic has an ionization energy of 14.2 meV which corresponds to a spectral onset of 114 cm^{-1}. At high bias, the electric field increases in the blocking layer and penetrates into the IR absorbing layer doped with Sb. Sb has an ionization energy of 10 meV (80 cm^{-1}) at low concentration. At the higher doping concentration the ionization energy decreases to 7.4 meV (60 cm^{-1}).

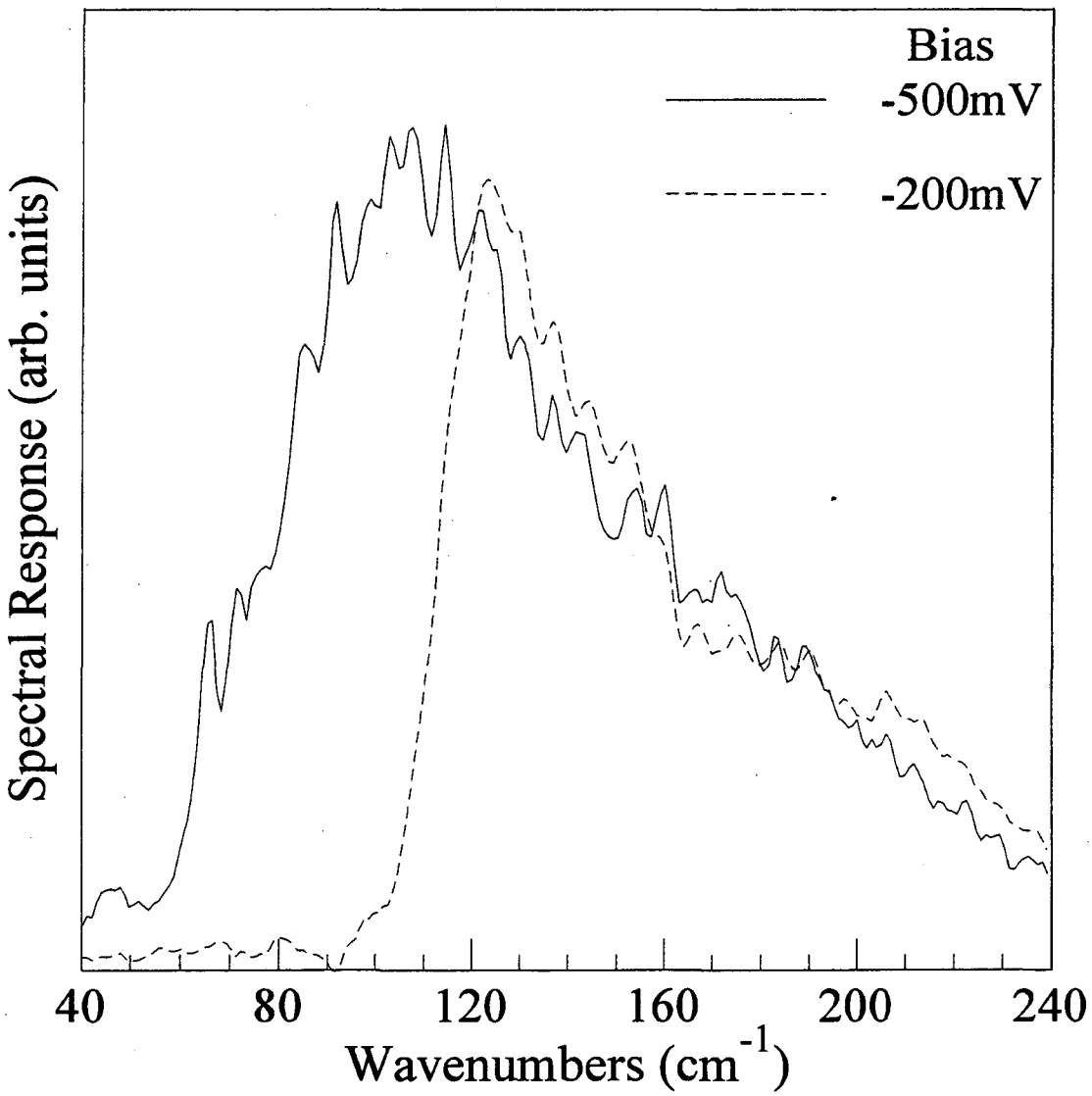

Fig. 4.1. The spectral response of BIB detector fabricated from LPE 91 measured at 2.0 K.

The two peaks on the onset of the BIB detector are located close to transitions $3p_o$ (76.4 cm^{-1}) and $2p_{\pm1}$ (69.4 cm^{-1}) states of Sb, but may also be due to internal reflection fringes as seen near the top of the detector response between 80 and 120 cm^{-1}.

The dark current of the BIB detector from LPE 91, shown in Fig. 4.2, displays the expected asymmetric current-voltage dependence. The dark current measurement at low biases is limited by the resolution of the amplifier circuit, approximately 10^{-14} A.

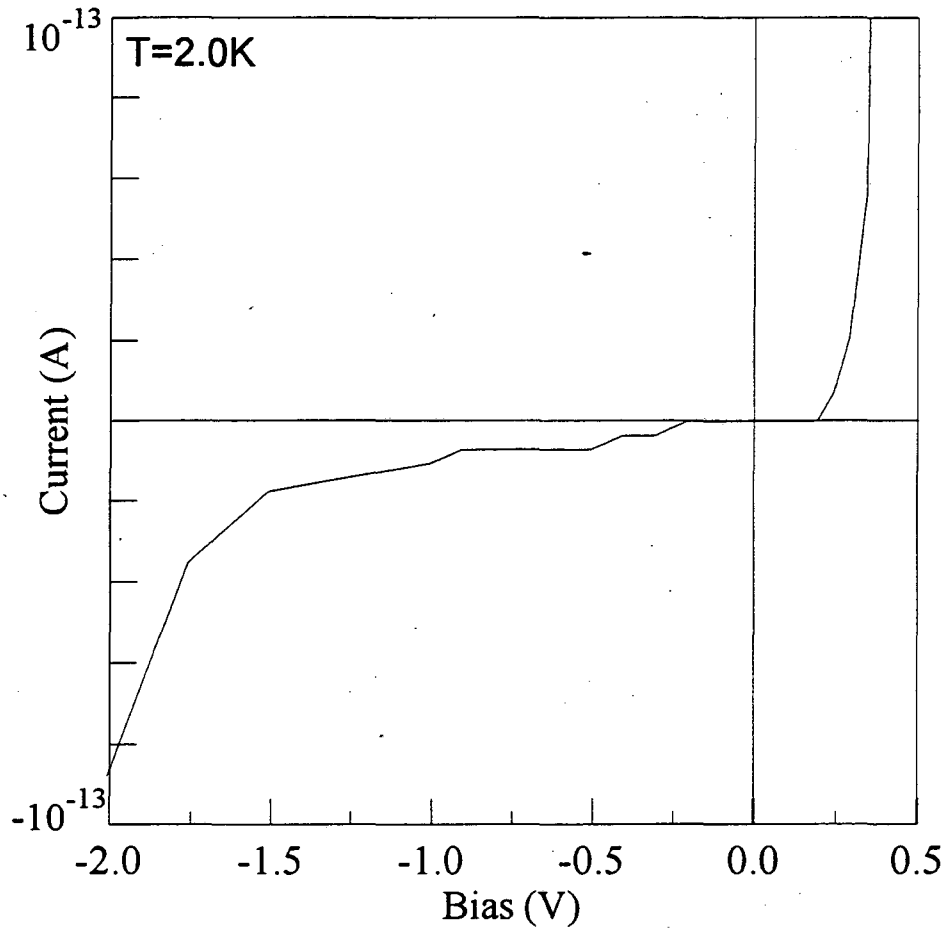

Fig. 4.2. Asymmetric I-V curve of BIB detector fabricated from LPE 91.

The responsivity of this detector was measured to be 1.2×10^{-3} A/W at 110 cm^{-1} with a 15 cm^{-1} bandwidth at a photon power of 4.5×10^{-12} W on the detector. The relatively low

responsivity was most likely caused by a high residual acceptor concentration ~10^{13} cm^{-3} in the IR absorbing layer. This acceptor concentration limits the absorption depletion width to approximately 1 μm. This poor responsivity was improved by decreasing this minority acceptor concentration and increasing the absorption volume.

During the first growths in the Ge LPE chamber, it was not clear whether the residual dopants were donors or acceptors after the "aging" process of the crucible. The 77 K Hall effect results on epilayers were alternating between n and p type, but at the time, the epilayers were believed to be p-type due the successful use of In-Ga contacts for p-type Ge. Based on this observation, Ge epilayers were grown as blocking layers on Ge:Ga substrates for p-type BIB detectors.

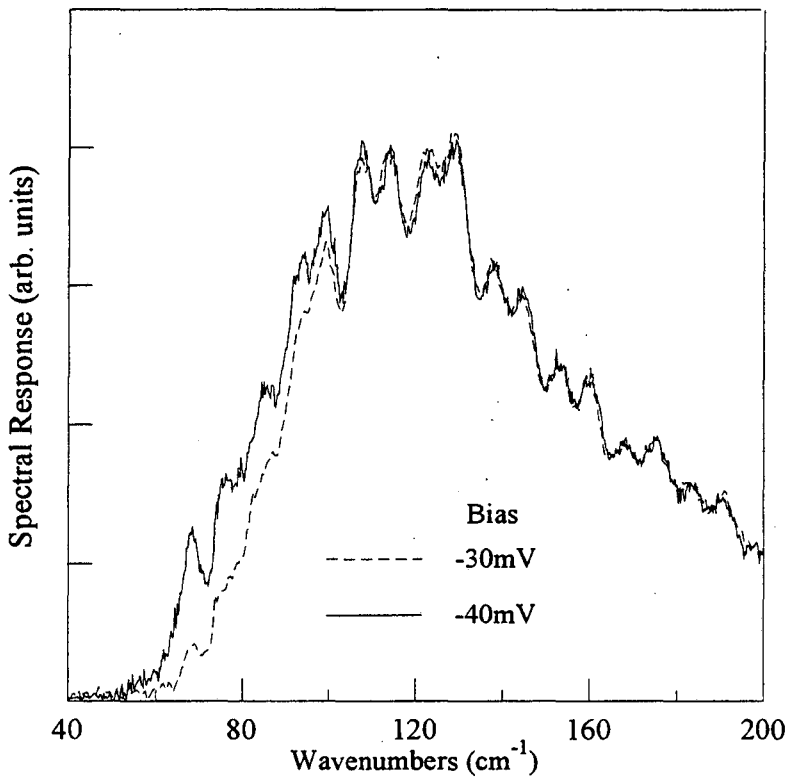

Fig. 4.3. Ge 737-9.0 BIB detector [Ga]=2x10^{16} cm^{-3} with 8 μm LPE 127 as the blocking layer.

The BIB detector in Fig. 4.3, showed some extended response to approximately 65 cm^{-1}, but because of high compensation and high dopant concentrations near 10^{14} cm^{-3} in the blocking epilayer, the dark current was extremely large at small biases, $4x10^{-11}$ A at -0.1 V bias.

Again based on the assumption that the residual impurities were mainly p-type, Ge epilayers were grown with Ga doping to fabricated p-type IR absorbing layers on lightly doped p-type substrates, crystal #410-6.8. LPE epilayer #132 BIB was Ga doped $7x10^{16}$ cm^{-3}, but exhibited very poor low wavenumber response, as shown in Fig. 4.4.

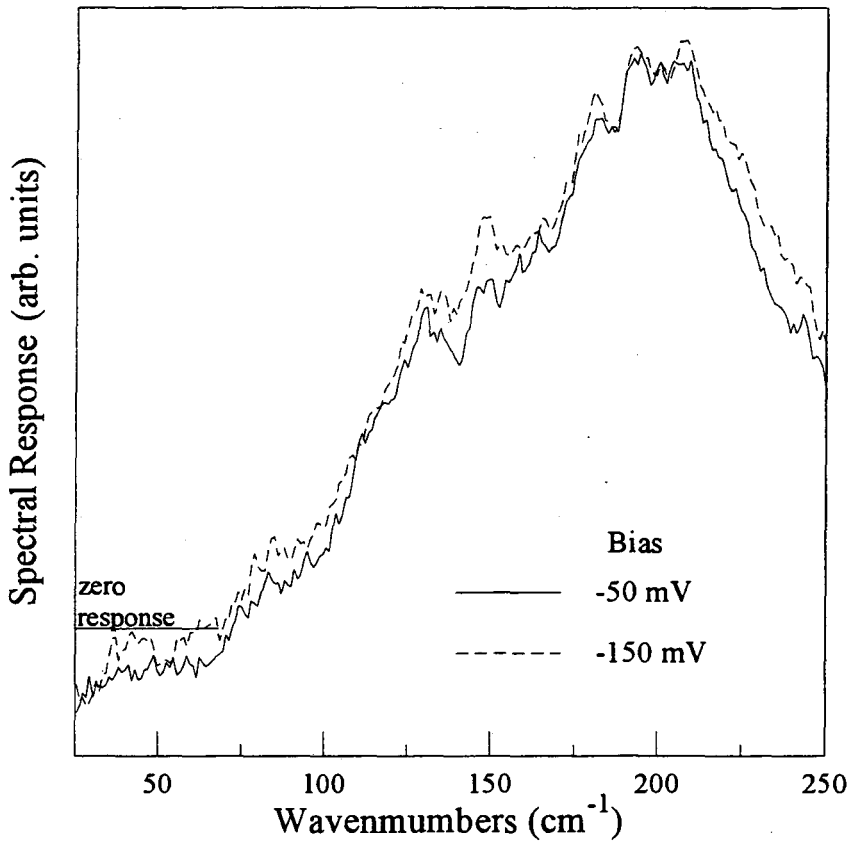

Fig. 4.4. BIB detector with epilayer LPE 132 [Ga]=$7x10^{16}$ cm^{-3} and 94 μm blocking layer of substrate 410-6.8. Measurement performed at T=1.3 K.

This poor response was most likely due to a minority donor concentration in the 10^{14} cm^{-3} range in the IR absorbing epilayer, thus limiting the depletion to 0.03 μm at -150 mV bias.

After the graphite crucible had been purified many times, the background acceptor concentration had dropped and the residual dopants in the epilayer growth were only due to the Pb solvent. At this point, epilayers were grown on Sb doped substrates cut from crystals #867 and #868. These crystal were doped at the seed end with $1.5x10^{16}$ and $5x10^{16}$ Sb cm^{-3} respectively and had an acceptor concentration around 10^{12} cm^{-3} inferred from previous Ge crystals grown in the same Czochralski growth chamber.(Czochralski 1918)

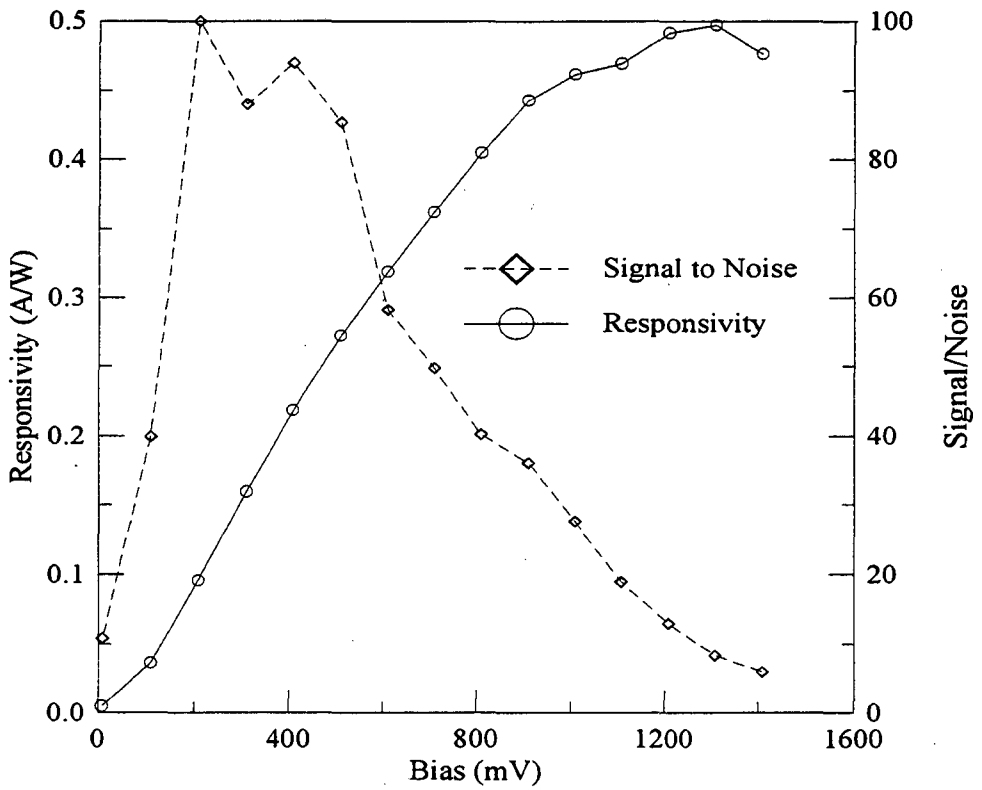

Fig. 4.5. Ge:Sb BIB detector with LPE 161 as the blocking layer. The IR absorbing layer was cut from 867-7.0 [Sb]=$1.5x10^{16}$ cm^{-3}. This measurement was performed at 1.35 K.

The spectral response and dark current of the BIB device fabricated from LPE 161 was not optimized showing a response out to 75 cm^{-1} and dark current of $4x10^{-12}$ A at -0.1 V bias. This detector did exhibit a significant improvement of the responsivity at 110 cm^{-1} in Fig. 4.5. Near the peak in signal to noise, the responsivity approached 0.2 A/W. This higher responsivity and lower acceptor concentration suggests a depletion width of around 5 μm at a bias of -400 mV. A large portion of the noise was most likely Johnson noise, as observed from the large dark currents.(Bratt 1977)

It had been suggested that since conventional Ge photoconductors operate optimally near a doping concentration of $1x10^{14}$ cm^{-3}, a blocking layer could operate at the same concentration. However, the poor dark current properties obtained with blocking layers doped to 10^{14} cm^{-3} prompted the production of the BIB detector through this secondary fabrication process described in section 4.1. The fact that the residual dopants were mainly donors and that the acceptor concentration lied in the 10^{11} cm^{-3} range, also inspired this secondary fabrication process of growing the IR absorbing layer.

The next generation BIB detectors were based on epilayers grown as the IR absorbing layer. In this case minority acceptor concentrations had to be less than 10^{12} cm^{-3} to obtain large depletion layers. Previous Gallium doped epilayers #129 to #137 had contaminated the growth crucibles, but continued improvements in the growth process brought the Ga concentration down as low as $3x10^{11}$ cm^{-3}.

This improvement in the epilayer acceptor concentration is attributed to many purification steps. The result again suggests that the commercial 99.9999% pure Pb is very low in acceptor impurities. The improvement in the epilayer acceptor concentration

has allowed growth of infrared absorbing layers with low compensation. The material improvement has lead to noticeable improvements in responsivity and signal to noise.

The Ge BIB detector fabricated from LPE 200 was the most successful detector. It performed well in all 3 of the main criteria. The IR absorbing epilayer was 50 μm thick doped to ~10^{16} cm^{-3} with Sb. The substrate blocking layer 738-16.5 was As doped $3x10^{13}$ cm^{-3} with a thickness of 85 μm.

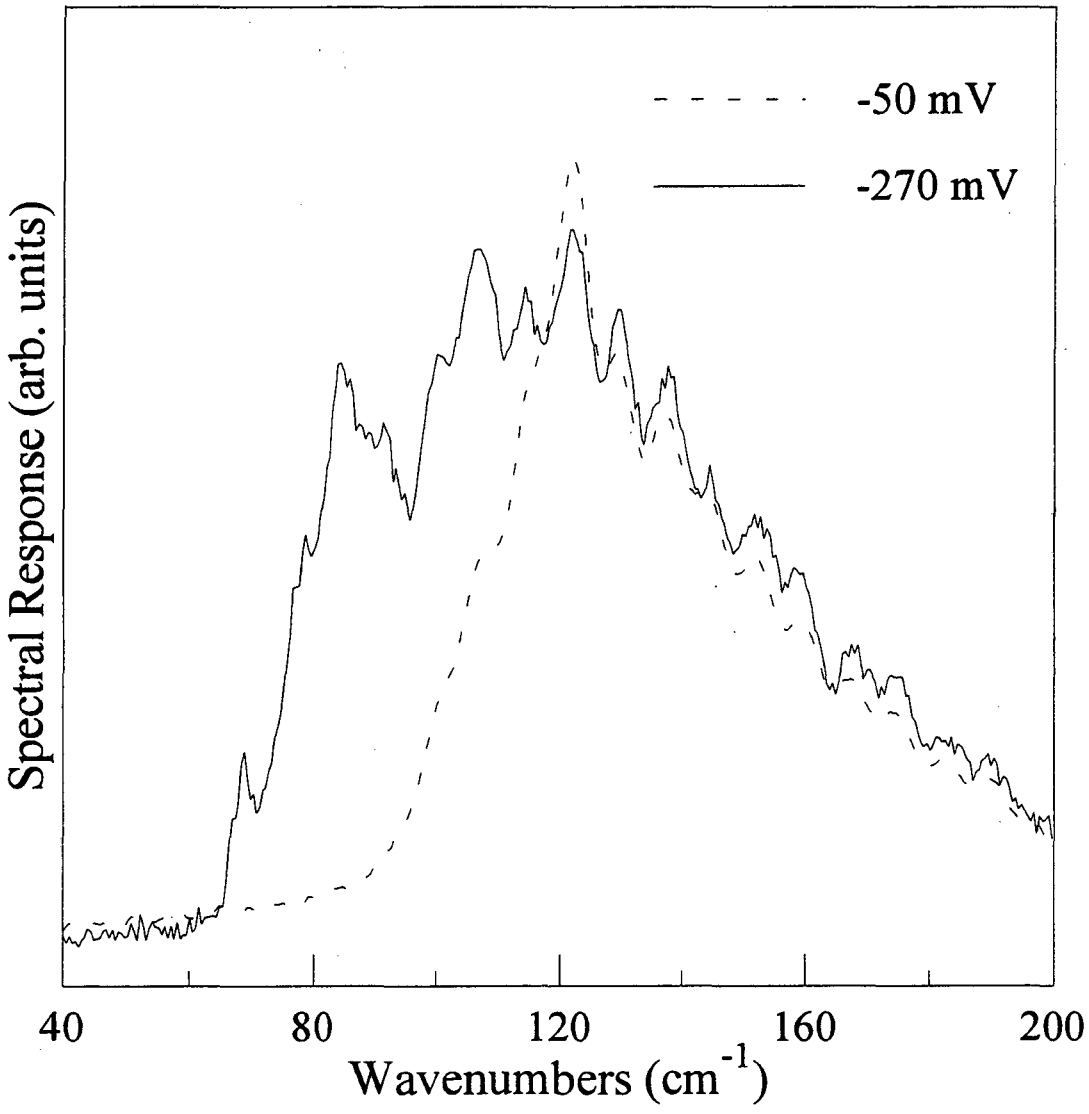

Fig. 4.6. Spectral response of Ge BIB detector produced from LPE 200 at 2.0 K.

This detector exhibited both an improved low wavenumber response shown in Fig. 4.6 and high responsivity measured at 111 cm^{-1} in Fig. 4.8. At low bias, the spectral response of the Ge BIB detector in Fig. 4.6 mainly comes from the As doped blocking layer, similar to the BIB detector response in Fig. 4.1. At high bias, the Sb in the IR absorbing layer dominates the photoresponse with an ionization energy of 65 cm^{-1}.

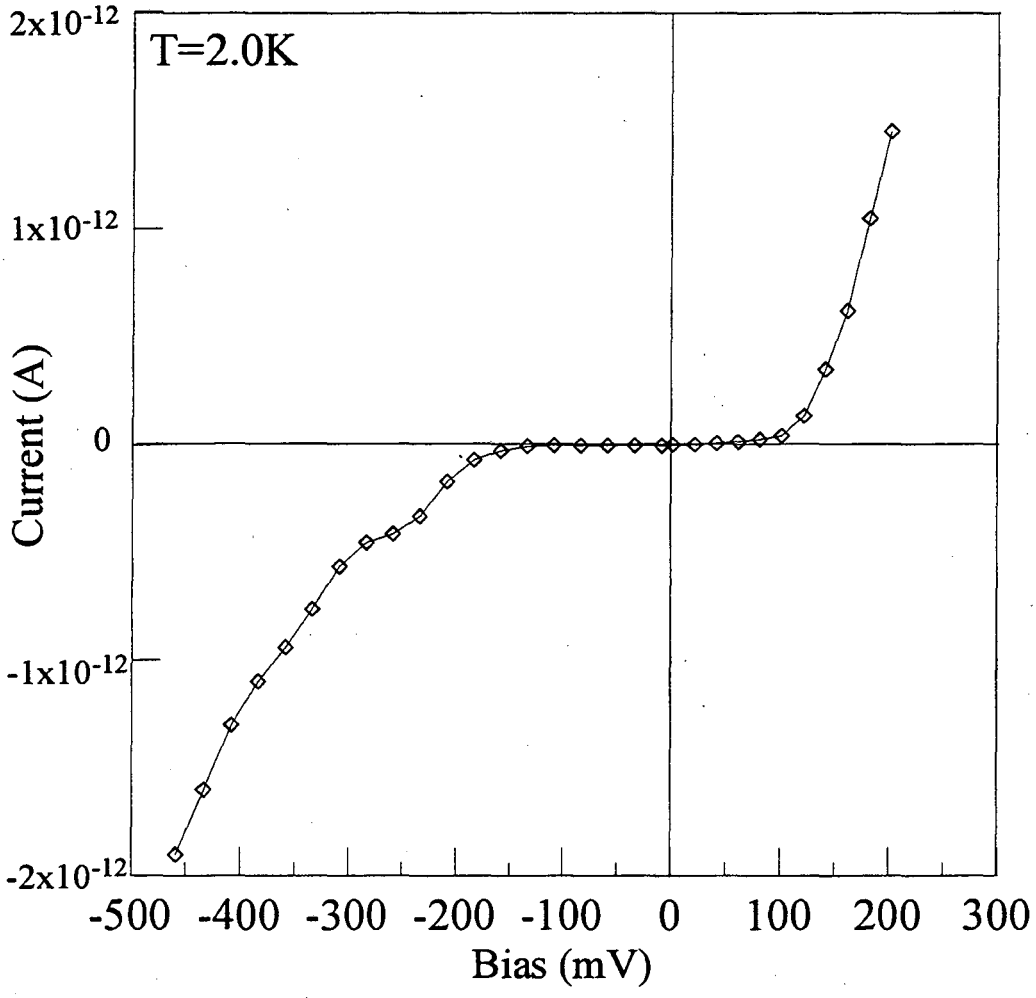

Fig. 4.7. I-V for Ge BIB made from LPE 200.

The dark current in Fig. 4.7 was not as low as had been observed for previous detectors. This was attributed to the higher doping $3x10^{13}$ cm^{-3} in the blocking layer. At the time this

detector was produced, the working hypothesis was that Cu acceptors became activated in the blocking layer, converting the blocking layer from n-type to p-type. Therefore, the substrate had a higher dopant concentration than in the ideal case.

At 650°C where the LPE growth takes place, the Cu substitutional solubility in Ge is 10^{14} cm^{-3}. (Hall and Racette 1964) It was later determined that Cu contamination in ultra-pure Ge substrates was reduced to approximately 10^{12} cm^{-3} while growing from a Pb solution. The Pb strongly getters the Cu during the growth process.

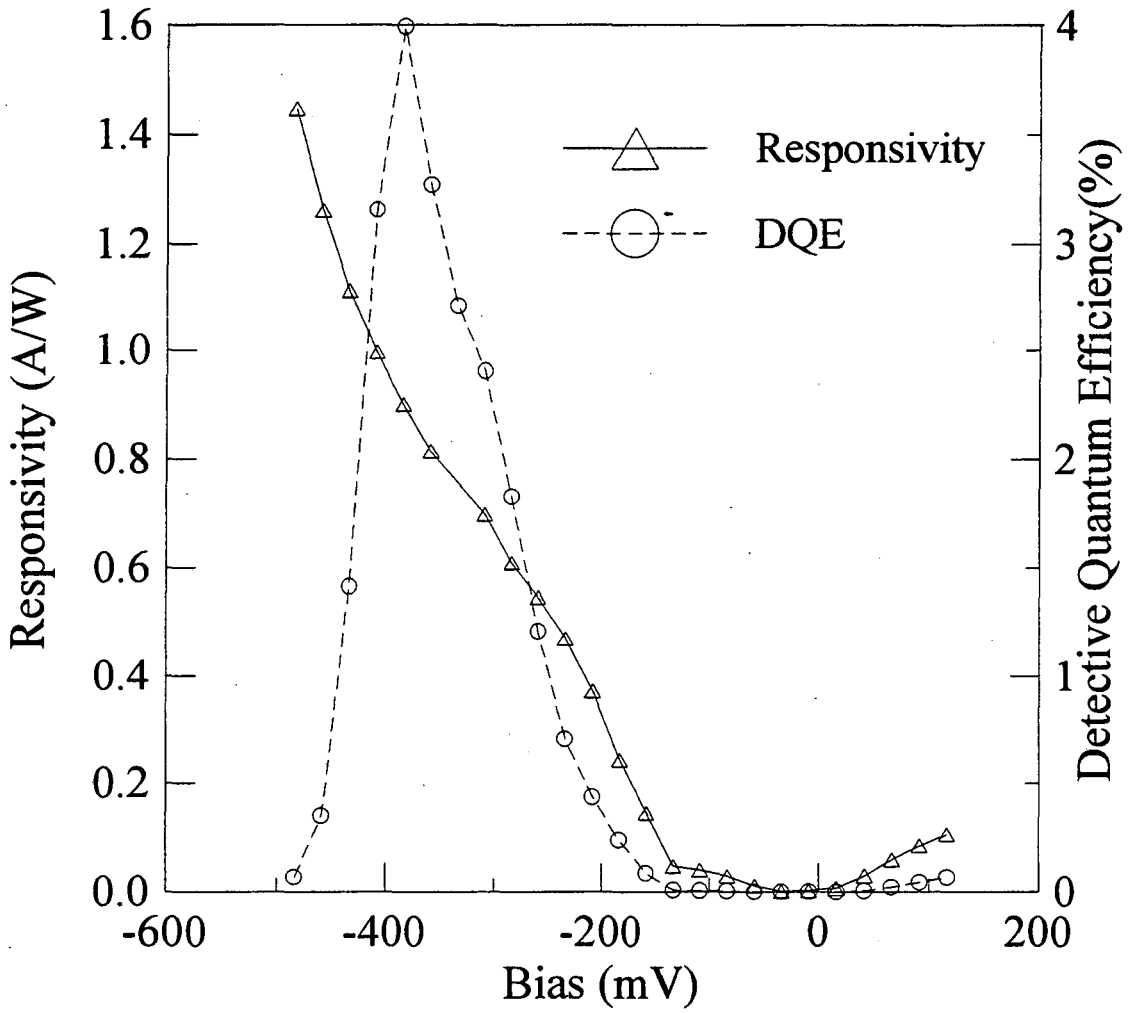

Fig. 4.8. Responsivity and DQE for Ge BIB from LPE 200 at 2K.

Cu suppression in n-type epilayers was also kept to at least $3x10^{11}$ cm^{-3} based on VTHE measurements on LPE epilayers. These results are summarized in Table 3.2. Other researchers have determined that at 650 °C, the segregation coefficient of Cu between molten Pb and solid Ge is $3x10^{-6}$.(Thurmond and Logan 1956)

The responsivity of the Ge BIB detector made from LPE 200 reaches nearly 1 A/W at the peak Detective Quantum Efficiency (DQE). The 4.0% DQE peak is very comparable to values of Ge:Ga bulk photoconductors which can range from 1.5 to 4.5 % for a single pass absorption geometry.(Beeman and Haller 1994) The DQE for a Ge:Ga 1 mm^3 detector in an integrating cavity reaches 4.8% at ν=111 cm^{-1}. The noise level for this detector also corresponded to a NEP of $4.0x10^{-16}$ $W/Hz^{1/2}$ at the signal to noise peak.

This BIB detector achieved a responsivity comparable to a Ge:Ga photoconductor that has an absorption volume of 1 mm^3, thus making the BIB detector radiation hard by a factor of 20. These Ge detectors have clearly achieved the radiation hardness characteristics expected from a BIB detector.

4.4 Optimization

Improvement in the reduction of minority acceptor dopant concentrations led to further improvements in the responsivity. Continued reduction in the minority impurity concentration would still improve the BIB detectors. Reduction of the dopant concentration in the blocking layer was shown to reduce the dark current. Devices with blocking epilayers of impurity concentrations of $2x10^{14}$ cm^{-3} were extremely leaky with high noise and poor photoresponse. When Sb doped epilayers were grown on bulk $3x10^{13}$ cm^{-3} doped substrates for blocking layers, the device started to work properly and the dark

current was in the 10^{-12} A range at peak responsivity. With blocking layers doped to $1x10^{12}$ cm^{-3}, the dark current dropped further into the 10^{-13} to 10^{-14} A range. The risk with such a low n-type blocking layer concentration is that Cu activation may convert the layer to p-type. A p-type blocking layer on a n-type IR absorbing layer would create a large offset between the bands that would require larger voltage biases to be applied. Growths with 10^{12} cm^{-3} blocking layers must be performed at lower temperatures possibly as low as 600 °C.

N. Haegel has performed modeling on Ge BIB detectors.(N.M. Haegel, to be published) This model takes into account the charge neutrality equation, the full continuity equation, and diffusion and drift effects. The results show that blocking layers must have an impurity concentration equal to or less than 10^{13} cm^{-3}. Modeling on a blocking layer of 10^{14} cm^{-3} impurity concentration has shown to collapse the electric field in the device.(Haegel 1997) These modeling results appear to agree with our experimental dark current measurements on the Ge BIB detectors that have been tested.

The maximum electric field which can be applied to the blocking layer of a BIB device is limited by the electric breakdown of the detector. The relationship for the E field distribution is derived in Appendix G from Poisson's equation. In Fig. 4.9, the E field distribution through the device was calculated for Ge BIB detector fabricated from epilayer #200. From this simple calculation, the maximum E field was determined to be 41 V/cm which is very large for a Ge photoconductor at low temperature. Researchers have shown breakdown voltages for Ge:Ga bulk photoconductors are near 2.0 V/cm at 3.0 K.(Beeman and Haller 1994)

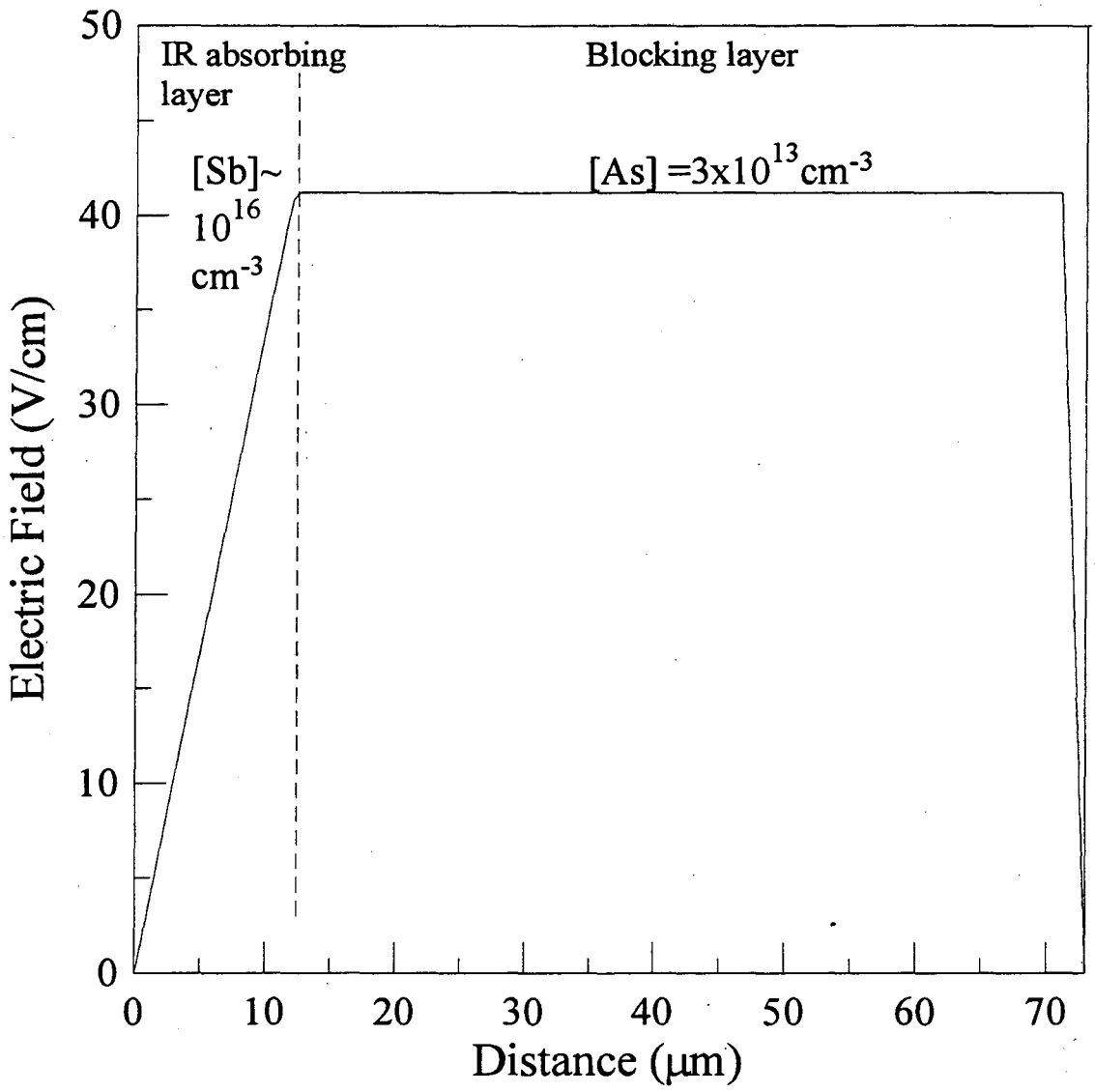

Fig. 4.9. Theoretical electric field distribution for Ge BIB 200 at -375 mV bias where the peak in signal to noise occurs.

To observe the role that excited states of IR absorbing layer dopants play in the low wavenumber response, an experiment was performed to observe the broadened excited states. A BIB detector was fabricated from LPE 233 with a IR absorbing epilayer of 48 μm and a Sb doping concentration of 2.4x10^{16} cm^{-3}. The substrate blocking layer

was cut from 738-14.5 with an As concentration of $1x10^{13}$ cm^{-3} and was polished to within 72 μm of the IR absorbing layer.

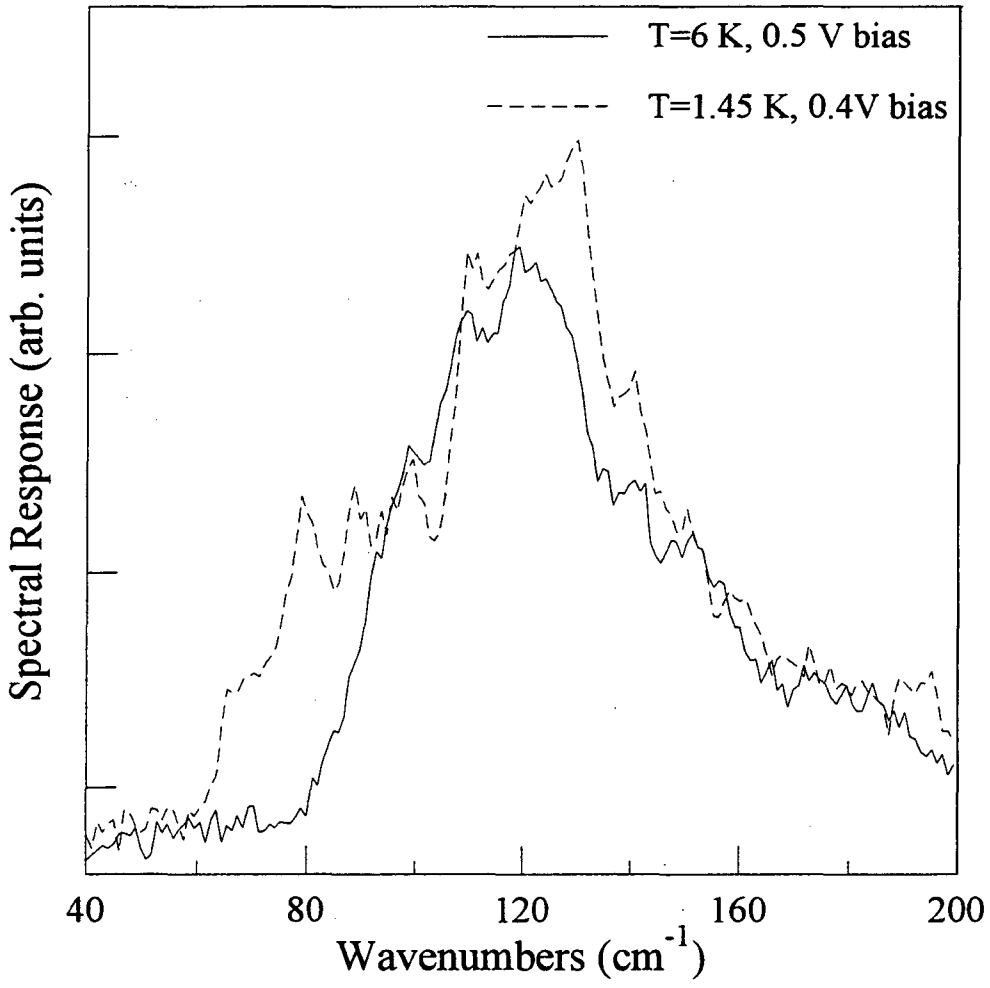

Fig. 4.10. Spectral response of Ge BIB fabricated from LPE 233 tested at both T=1.45 K and 6.0K.

At 1.45 K, the BIB detector exhibited a response to 60 cm^{-1} as seen in Fig. 4.10. At 6.0 K, the BIB detector responded a frequencies greater than 80 cm^{-1}. The difference in the observed response is attributed to the freezing out of the low ionization energy states that respond at 1.45 K. At 6 K, these energy states are no longer populated. Neither of the two measurement gave rise to any of the sharp bound excited state

transitions reported for p-type BIB detectors in the literature. (Watson and Huffman 1988)

4.5 Future Studies

Future work should include optimization of Pb purification for fabrication of high purity epilayers. Only after the process to grow pure blocking layers with impurity concentrations less than 10^{13} cm^{-3} has been developed, can other aspects of Ge BIB detectors be fully explored.

One of these aspects yet to be fully studied is the low wavenumber onset as a function of the IR absorbing layer doping concentration. Future work should include the systematic variation of this concentration to determinate if the reduction of the onset frequency response can be controlled reproducibly. Sb and As doped Si BIB detectors have shown a reduction in ionization energy of around 28% and 22% at concentrations of $3.6x10^{17}$ and $5x10^{17}$ cm^{-3} respectively.(Huffman, et al. 1992; Reynolds, et al. 1989) Ge:Sb BIB detectors have exhibited a reduction in ionization energy from 80 to 60 cm^{-1} at a concentration of $3x10^{16}$ cm^{-3}. This corresponds approximately to a 25% reduction. Ge BIB detectors have achieved the same success as Si BIB detectors in this respect. Other researchers have shown response as low as 50 cm^{-1} (Watson and Huffman 1988; Wu, et al. 1991), but it is not clear that 50 cm^{-1} can be achieved reproducibly.

5. Summary and Conclusion

This research has shown that epilayers with residual impurity concentrations of $5x10^{13}$ cm^{-3} can be grown by producing the purest Pb available in the world. These epilayers have extremely low minority acceptor concentrations, which is ideal for

fabrication of IR absorbing layers. The Pb LPE growth of Ge also has the advantageous property of gettering Cu from the epilayer and the substrate. Epilayers have been grown with intentional Sb doping for IR absorption on lightly doped substrates. This research has proven that properly working Ge BIB detectors can be fabricated from the liquid phase as long as pure enough solvents are available. The detectors have responded at proper wavelengths when reversed biased even though the response did not quite reach minimum wavenumbers. Optimization of the Sb doping concentration should further decrease the photoionization energy of these detectors. Ge BIB detectors have been fabricated that respond to 60 cm^{-1} with low responsivity. Through reduction of the minority residual impurities, detector performance has reached responsivities of 1 A/W. These detectors have exhibited quantum efficiency and NEP values that rival conventional photoconductors and are expected to provide a much more sensitive tool for new scientific discoveries in a number of fields, including solid state studies, astronomy, and cosmology.

Appendix A: Hall Effect

The basics of Hall effect are reviewed in this appendix. More detailed descriptions have been published by others.(Putley 1960; Beer 1980) Free carriers traveling in a magnetic field **B** experience a Lorentz force F_L given by

$$F_L = q\,(\mathbf{v}\mathrm{x}\mathbf{B}) \tag{A1}$$

where **v** is the velocity of the carrier of charge q. E.H. Hall (1879) observed the generation of a voltage V_H perpendicular to the current I_x and the magnetic induction direction B_z. This effect in a bar of material is schematically illustrated in Fig. A1. Carriers are deflected in the direction of F_y and accumulate on one side of the bar thus generating an electric field

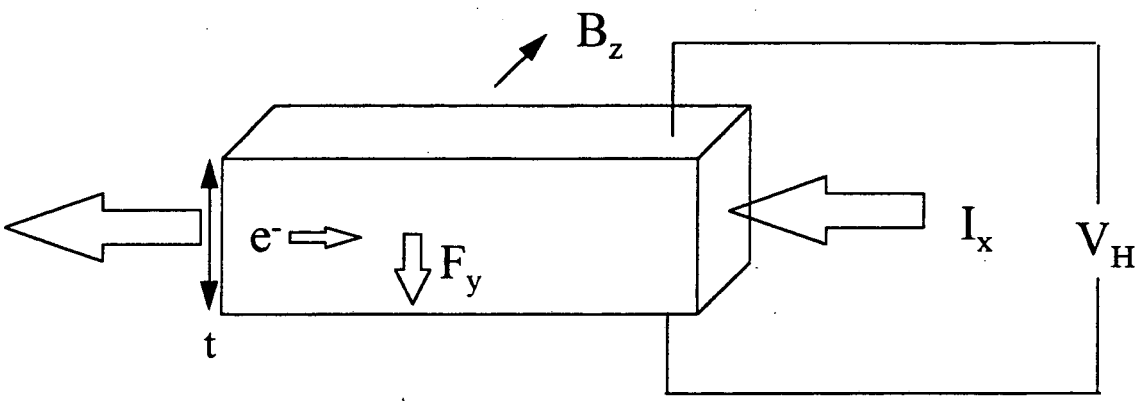

Fig. A1 Schematic of Hall effect in a bar of material

and the measurable Hall voltage V_H. It can be found from balancing the Lorentz force with the Hall field force that the Hall coefficient R_H is

$$R_H = \frac{tV_H}{I_x B_z} = \frac{1}{nq} \tag{A2}$$

where n is the free carrier concentration and t is the thickness of the sample. The carrier concentration can now determined from these experimental parameters. It is found that equation A2 is not accurate and the so called Hall factor r_H has been added to correct for this deviation. In general , $R_H=r_H/nq$, where r_H varies between 0.5 to 2 depending on the scattering mechanisms that are dominant. The Hall factor r_H approaches unity for the condition of $\mu B>1$, where μ is the mobility given in m^2/Vs and B is in units of Tesla.(Beer and Wilardson 1958) This is satisfied at large magnetic inductions and large mobilities.

Variable temperature Hall effect (VTHE) leads to one of the most useful techniques. Besides measuring the majority carrier type and concentration, the majority dopant ionization energies and minority dopant concentrations can be determined as well. If a resistivity measurement is also performed, the mobility can be determined. In VTHE for a n-type semiconductor, as the temperature is lowered, electrons begin to "freeze-out" onto donor sites. "Free carrier statistics" is used to determine the free carrier concentration.(Blakemore 1987) This process of freezing out can be described by the probability that a donor of energy E_D is occupied at temperature T.

$$N_D - N_A = \frac{N_D}{1 + 0.5\exp(\frac{E_D - E_F}{kT})} + n \qquad \text{(A3)}$$

The first term on the right hand side of equation A3 is the total number of donors occupied by electrons. N_D is the total donors and N_A is the total acceptor concentration. E_F is the Fermi level energy and n is the number of electrons excited into the conduction band. The Fermi level dependence can be removed due to its relationship to the density of states N_C and n.

$$n = \frac{1}{2}(\phi + N_A)([1 - \frac{4(N_D - N_A)}{(\phi + N_A)^2}]^{1/2} + 1) \tag{A4}$$

$$\text{with } \phi = \frac{1}{2} N_C \exp(\frac{E_D}{kT}) \tag{A5}$$

Equation A4 allows fitting of freeze-out curves and the determination of N_D, N_A and E_D as a function of temperature. This solution is valid for a single donor and acceptor. A system with a double donor is a more complicated problem and is not covered in this work. An example of a single level "freeze-out" curve is shown in Fig. A2.

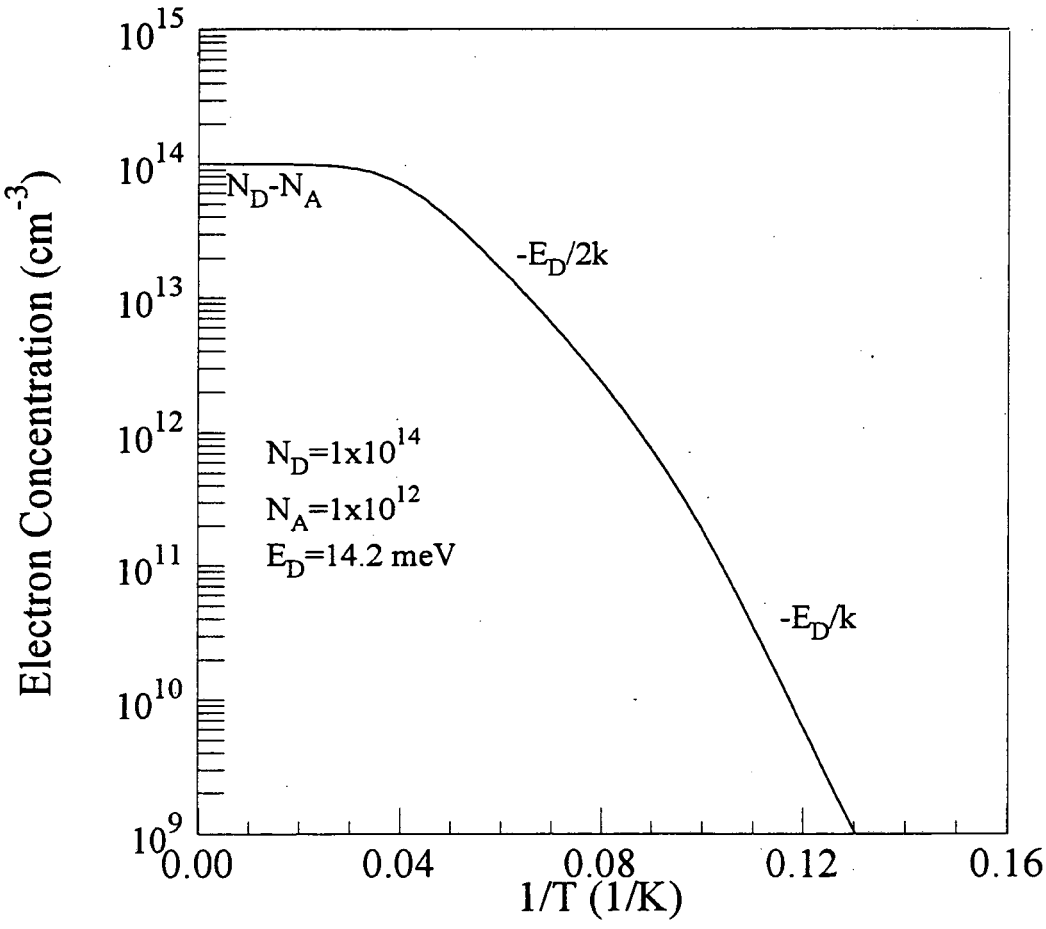

Fig. A2. Theoretical Fit for Ge:As freeze-out.

In the VTHE freeze-out curve, the minority dopant concentration corresponds to the free carrier concentration at the transition point of the half slope $-E_a/2k$ to the full slope $-E_a/k$ regime, but it is much more accurate to calculate and fit the experimental points, especially for highly compensated samples.

Samples were prepared for the van der Pauw configuration (van der Pauw 1958). Hall effect measurements require a current source, a volt meter, and an electromagnet. The Hall effect measurement system is automated by an IBM 286 computer. Samples are mounted on a cold finger in a Lakeshore CT-210 continuous flow liquid helium cryostat which allows cooling down to approximately 4.5 K. Care must be taken in stabilizing the temperature before each measurement. Applied currents can range from 10^{-2} to 10^{-9} A and Hall measurement were performed at 0.3 Tesla. The applied current was adjusted to maximize the Hall voltage generated, but at the same time not to heat the sample. At low temperatures, $T < 30$ K, resistive heating of the sample must be kept below 10 nW to prevent the sample temperature from being disturbed by the resistivity and Hall measurement.

Appendix B: Fourier Transform Far Infrared Spectroscopy

A far infrared Fourier transform spectrometer has been used for PTIS characterization of Ge LPE epilayers and of the spectral response of Ge BIB detectors. A schematic of the basic Michelson interferometer is shown in Fig. B1. The spectrometer has 4 different mirrors, a parabolic mirror M_p, a fixed mirror M_f, a movable mirror M_m and a off-axis paraboloid M_{op}. The light from the source S forms a parallel 4 inch diameter beam after reflection off the parabolic mirror. The light travels through the beam splitter BS and which splits the incoming light into two beams. One beam is reflected by a fixed mirror and the other by the movable mirror. The two beams are sent back to the BS where they recombine. The movable mirror can be used to change the path length of one beam. The difference in path length of the two beams causes some wavelengths to interfere constructively and some destructively.

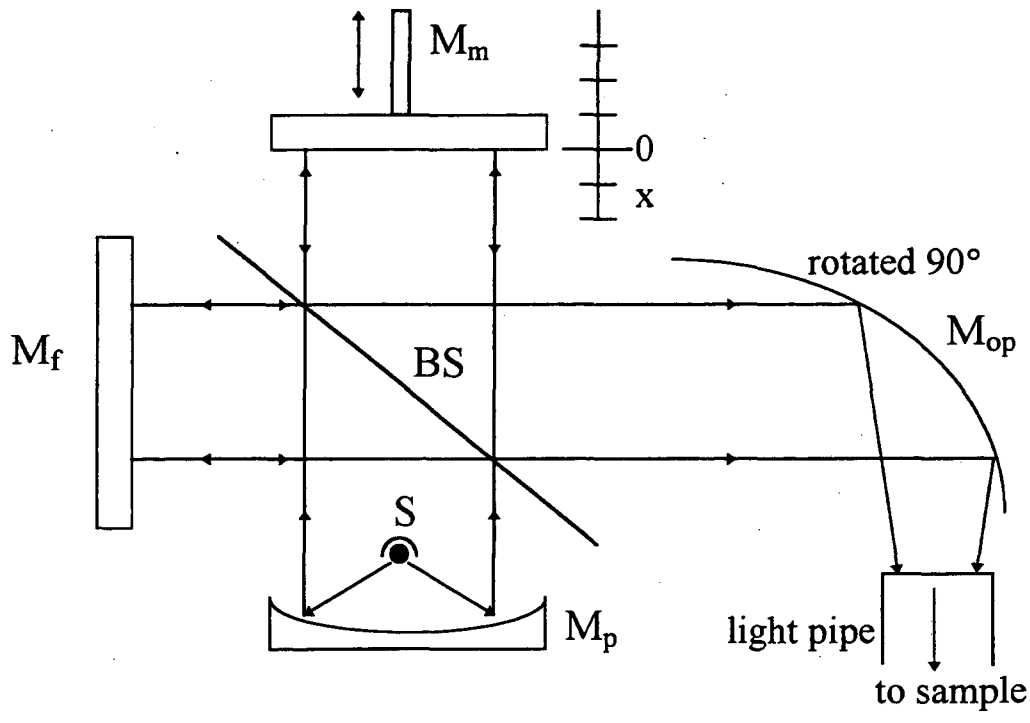

Fig. B1. Schematic of Fourier Transform Spectrometer.

The changing interference produces a cosine modulation of each wavelength component in the beam. The intensity of the exit beam represents an interferogram. A Fourier transformation of the interferogram is numerically performed and yields the spectrum.

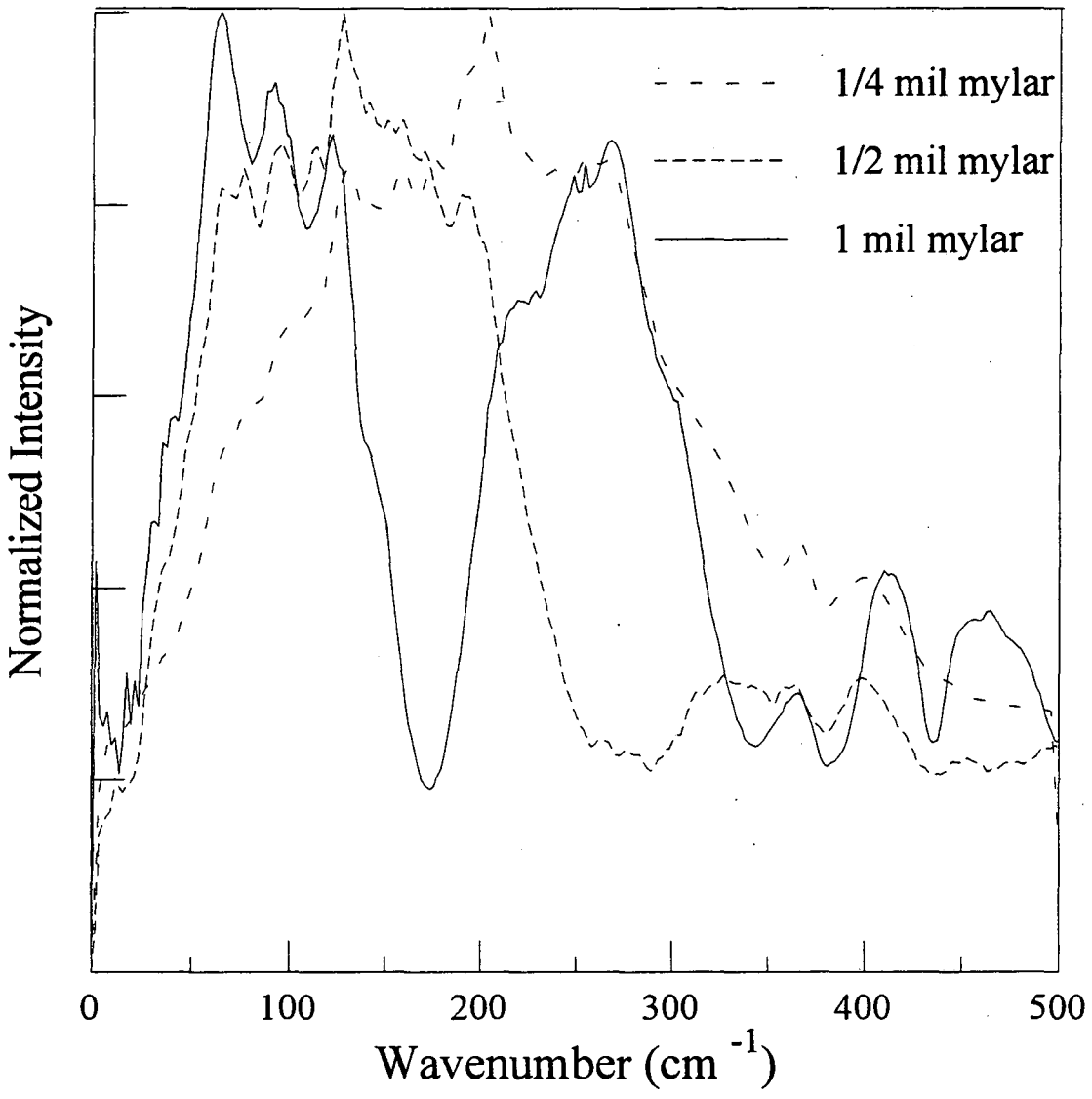

Fig. B2 Instrument response of beam splitters in Far Infrared Fourier Transform Spectrometer recorded with a Golay cell.

The far infrared Fourier transform spectrometer operates from 0 to 500 cm^{-1} with a 1/4 mil mylar beam splitter. The instrument response is shown up to 500 cm^{-1} in Fig. B2

measured at 14.3 Hz chopping frequency with a Golay cell. The instrument response at smaller wavenumbers can be improved by using a thicker beam splitter. The 1/2 mil beam splitter has about half the efficiency at 50 cm^{-1} compared to the 1 mil beam splitter. By using a 1 mil thick mylar beam splitter, the instrument gain can be maximized at low wavenumbers around 50 cm^{-1}, which is the region of interest for a working Ge BIB detector. The interferometer is evacuated to 0.1 militorr in order to eliminate water vapor and CO_2 absorption and to reduce microphonic noise. The far IR source is a mercury arc lamp with ~50% of the IR output originating in the arc and the remaining 50% from the hot silica envelope. Outside the interferometer the far IR light is guided out through polished brass "light" pipes that are evacuated to 30 militorr to remove interference from absorption. For epilayer PTIS measurements, the output of the spectrometer is channeled into the PTIS sample holder. An 8 mil thick black polyethylene filter was placed in the light path to eliminate above Ge band gap light and transmit only the far IR light. For BIB detector measurements, the light enters the IR Labs dewar through a polyethylene window, travels through the liquid nitrogen cooled aperture and the liquid helium cooled aperture to the detector. In all the BIB detector measurements the FTIR detector is the BIB device and its output signal forms the interferogram.

Appendix C: Photothermal Ionization Spectroscopy

Photothermal Ionization Spectroscopy (PTIS) is a two step process consisting of exciting a carrier from its ground state into a bound excited state following thermal ionization. A temperature is chosen such that sufficient phonons are present to excite the carrier into the conduction or valence band. The photoconductivity signal is measured with a lock-in amplifier referenced to the light chopper frequency. The characteristic ground state to bound excited state lines identify the chemical impurities present in the semiconductor.

For these measurements, a pyrex liquid helium cryostat with a liquid nitrogen cooled shield was used. Samples were inserted into an exchange gas sample holder, Fig. C1, to allow measurements at and above 4.2K.

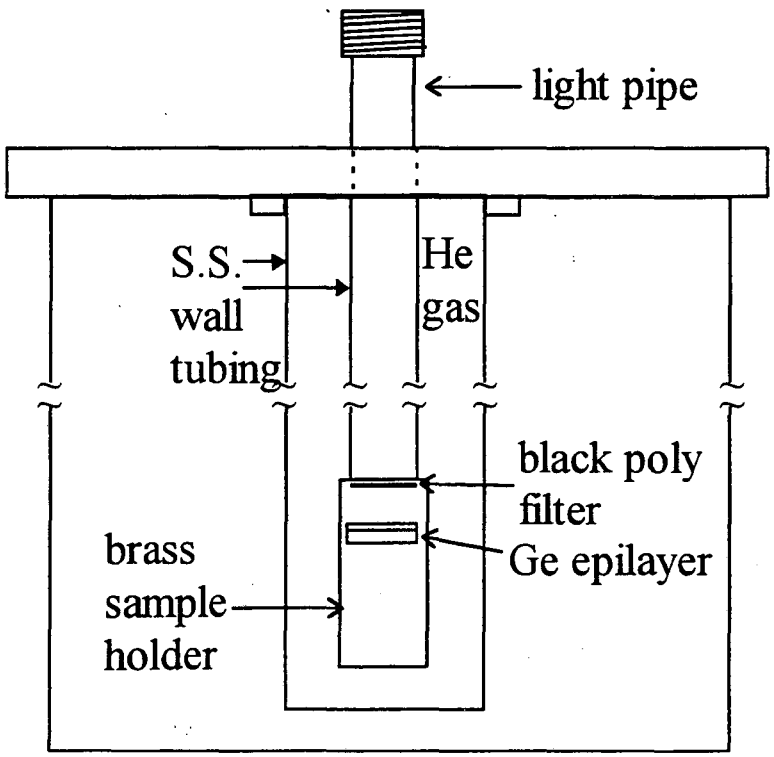

Fig. C1 Schematic of exchange gas sample holder.

The sample space is first pumped out and then back filled with a small amount of He gas for a thermal link to the liquid helium. A heater resistor is imbedded into the brass sample holder along with a temperature sensing resistor. By balancing the heater input power with the thermal link (i.e. He pressure), temperatures between 4.2 to 20 K can be achieved. Samples are exposed to chopped far infrared light through a cold 8 mil black polyethylene filter in the brass sample holder. Photoconductive response of the sample is measured with two coaxial wires to reduce 60 Hz noise pickup. An infrared LED is mounted in the brass sample holder to allow dc illumination of above band gap light for identification of minority dopants. (Lifshits and Ya Nad' 1965) This technique is well developed for identifying impurities in Ge.(Haller and Hansen 1974b)

Appendix D: Epilayer Growth Results

Crystal	Substrate & Orientation	Growth Conditions	Hall Effect (cm^{-3})	Comments
100	739-11.8 (111)	655°C 3.5hr., 650°C to 565°C 85 min.	$n=5.4x10^{16}$	t~10μm
101	739-11.8 (111)	655°C 7hr., 650°C to 350°C 15hr.	$n=4.6x10^{15}$	t~15μm
102	739-11.8 (111)	655°C 6hr., 650°C to 350°C 15hr.	$p=1x10^{15}$	t~40μm
103	739-11.8 (111)	655°C 14.5hr., 650°C to 470°C 9hr.	$p=6x10^{14}$	t~12μm
104	739-11.8 (111)	655°C 8hr., 650°C to 350°C 15hr.	$p=3.6x10^{15}$	t~35μm
105	739-11.8 (111)	655°C 6.5hr., 650°C to 350°C 15hr.	$p=8.0x10^{14}$	t~30μm
106	742-7.0 (100)	655°C 8hr., 650°C to 350°C 15hr.	$p=2x10^{16}$	t~25μm
107	739-11.8 (111)	655°C 8hr., 650°C to 350°C 15hr.	$p=1.3x10^{15}$	t~15μm
108	739-11.8 (111)	655°C 17.5hr., 650°C to 350°C 4hr.	$p=3.6x10^{15}$	t~20μm
109	822-7.3 (100)	655°C 14hr., 650°C to 350°C 4hr.	$p\sim10^{18}$	t~25μm
110	822-7.3 (100)	655°C 14hr., 650°C to 350°C 15hr.	not meas.	sample broke
111	822-7.3 (100)	655°C 8hr.,660°C 30min, 650°C to 375°C 14hr.	$p=1.6x10^{14}$	t~40μm
112	739-11.8 (111)	655°C 6.5hr.,660°C 30min, 650°C to 350°C 15hr	$n=6x10^{14}$	t~50μm
113	822-7.3 (100)	655°C 7hr.,655°C 30min, 650°C to 350°C 15hr.	not meas.	tipping problem
114	739-11.8 (111)	655°C 6.5hr., 658°C 20min, 12hr. to 350°C	not meas.	tipping problem
115	731-8.2 (311)	655°C 5hr., 658°C 20min, 12hr. to 350°C	$n=2x10^{14}$	t~15μm
116	739-11.8 (111)	655°C 8hr., 658°C 20min, 12hr. to 340°C	not. meas.	
117	737-9 (111)	655°C 5.5hr., 658°C 20min, 12hr. to 340°C	$n=1.2x10^{14}$	CV meas.
118	739-11.8 (111)	655°C 7.5hr., 658°C 20min, 12hr. to 340°C	not. meas.	H_2 ran out

119	731-8.2 (311)	655°C 7hr., 658°C 20min, 12hr. to 340°C	n=3.8x10^{13}	t~41μm
120	731-8.2 (311)	655°C 7hr., 658°C 20min, 12hr. to 340°C	p=4.8x10^{13}	t~22μm
121	739-11.8 (111)	655°C 7hr., 658°C 20min, 12hr. to 340°C	p=1.6x10^{14}	CV meas.
122	738-8.5 (111)	655°C 7hr., 658°C 20min, 12hr. to 340°C	p=5x10^{16}	Ga contaminant
123	737-9 (111)	655°C 6.5hr., 658°C 20min, 12hr. to 340°C	not meas.	BIB subst.
124	738-8.5 (111)	655°C 7hr., 658°C 20min, 12hr. to 340°C	p=1x10^{15}	t~25μm
125	573-6.5 (100)	655°C 7hr., 658°C 20min, 12hr. to 340°C	p=1x10^{14}	t~40μm
126	738-8.5 (111)	655°C 5hr., 658°C 20min, 12hr. to 340°C	p=8x10^{13}	t~5μm
127	737-9 (111)	655°C 7hr., 658°C 20min, 12hr. to 340°C	N/A	doped substrate
128	738-8.5 (111)	655°C 5hr., 658°C 20min, 12hr. to 340°C	p=2x10^{14}	t~17μm
129	738-8.5 (111)	655°C 6.5hr., 658°C 20min, 12hr. to 340°C	p=1x10^{17}	Ga doped t~58μm
130	738-8.5 (111)	655°C 6.5hr., 658°C 20min, 12hr. to 340°C	not meas.	
131	822-7.3 (100)	655°C 5hr., 658°C 20min, 12hr. to 350°C	p=10^{13}	
132	410-6.8 (111)	655°C 6.5hr., 658°C 20min, 12hr. to 340°C	p~7x10^{16}	Ga doped, t~56μm
133	410-6.8 (111)	655°C 6.5hr., 658°C 20min, 12hr. to 340°C	not meas.	
134	410-6.8 (111)	655°C 6.5hr., 658°C 20min, 12hr. to 340°C	p=5.2x10^{16}	Ga doped t~32μm
135	410-6.8 (111)	655°C 6.5hr., 658°C 20min, 12hr. to 340°C	p=2.6x10^{16}	Ga doped t~70μm
136	410-6.8 (111)	655°C 6.5hr., 658°C 20min, 12hr. to 340°C	p~6.6x10^{16}	Ga doped
137	410-6.8 (111)	655°C 6.5hr., 658°C 20min, 12hr. to 340°C	p~7x10^{16}	Ga doped
138	410-7.0 (111)	675°C 7hr., 678°C 20min, 12hr. to 350°C	n=3.4x10^{14}	t~60μm
139	822-7.3 (100)	665°C 6.5hr., 668°C 20min, 12hr. to 340°C	n=4x10^{13}	t~25μm

140	410-7.0 (111)	665°C 6.5hr., 668°C 20min, 12hr. to 340°C	n=5.8x10^{14}	t~50μm
141	410-7.0 (111)	665°C 6.5hr., 668°C 20min, 12hr. to 340°C	n=4.8x10^{15}	t~50μm
142	410-7.0 (111)	670°C 6.5hr., 673°C 20min, 12hr. to 340°C	not meas.	
143	573-6.3 (100)	670°C 3hr., maximum thermal cool to 340°C	not meas.	pyramid growth (111) faceting
144	573-6.3 (100)	665°C 6.5hr., 668°C 20min, 12hr. to 340°C	not meas.	pyramid growth (111) faceting
145	410-7.0 (111)	665°C 6.5hr., 668°C 20min, 12hr. to 340°C	n=1.5x10^{14}	t~50μm
146	410-7.0 (111)	665°C 6.5hr., 668°C 20min, 12hr. to 340°C	n=1.7x10^{14}	t~40μm
147	410-7.0 (111)	665°C 3.5hrs., 3.5 hrs thermal cool to 380°C	n=1.6x10^{14}	t~27μm
148	410-7.0 (111)	665°C 5hrs., 3.5 hrs thermal cool to 383°C	not meas.	t~27μm
149	410-7.0 (111)	660°C 3.5 hrs., 3.5 hrs thermal cool to 370 °C	n=1.2x10^{14}	t~37μm
150	410-7.0 (111)	600°C 3.25 hrs., 3.5 hrs. thermal cool to 380°C	p=1.3x10^{14}	t~20μm
151	410-7.3 (111)	675°C 6.5 hr., 678°C 20min., 15hr. to 340°C	not meas.	t~70μm
152	410-7.3 (111)	675°C 6.5 hr., 678°C 20min., 15hr. to 340°C	not meas.	
153	410-7.0 (111)	550°C 4hrs, thermal cool to 340°C	not meas.	dissolved subs.
154	410-7.0 (111)	550°C 4hrs, thermal cool to 340°C	not meas.	
155	410-7.0 (111)	665°C 6.5hrs, 668°C 20 min, 15 hrs to 340°C	n=4x10^{15}	t~85μm
156	410-7.0 (111)	665°C 3hrs, thermal cool 4hrs to 385°C	n=1.8x10^{15}	t~52μm
157	410-7.0 (111)	665°C 5hrs, thermal cool to 340°C	n=1.6x10^{15}	t~40μm
158	410-7.0 (111)	665°C 3.5hrs, thermal cool to 370°C	n=1.4x10^{15}	t~35μm
159	410-7.0 (111)	665°C 4.5hrs, thermal cool to 380°C	n=5.6x10^{14}	t~30μm
160	867-7.0 (111)	665°C 7hrs, 668°C 20 min 15 hrs to 340°C	N/A	doped substrate

161	867-7.0 (111)	500°C 4hrs, thermal cool to 350°C 2.75 hrs.	N/A	doped substrate
162	410-7.0 (111)	665°C 3hrs, thermal cool to 350°C 4.5 hrs.	$n=5.6x10^{14}$	t~40μm
163	867-7.0 (111)	550°C 5hrs, thermal cool to 360°C 4.25 hrs.	N/A	doped substrate
164	410-7.2 (111)	665°C 4hrs, thermal cool to 420°C 3 hrs.	$n=7x10^{14}$	t~30μm
165	410-7.2 (111)	665°C 3.5hrs, thermal cool to 346°C 4.66 hrs.	$n=8x10^{14}$	t~32μm
166	868-7.8 (111)	540°C 3.25hrs, thermal cool to 336°C 3.66 hrs.	N/A	doped substrate t~17μm
167	867-12.7 (111)	540°C 3.75hrs, thermal cool to346°C 3.33 hrs.	N/A	doped substrate t~15μm
168	410-7.2 (111)	665°C 3.5hrs, thermal cool to 344°C 4.5 hrs.	$n=6.8x10^{14}$	t~42μm
169	410-7.2 (111)	665°C 3.66hrs, thermal cool to 412°C 3 hrs.	not meas.	
170	410-7.2 (111)	665°C 3.5hrs, thermal cool to 355°C 4.5 hrs.	$n=9.2x10^{14}$	t~17μm
171	573-6.3 (100)	665°C 3.25 hrs, thermal cool to 360°C 4.5 hrs.	not meas.	
172	410-7.2 (111)	625°C 3hrs, thermal cool to 323°C 5 hrs.	$n=6x10^{16}$	Bi solvent t~50μm
173	410-7.2 (111)	665°C 2.5hrs, thermal cool to 427°C 3.25 hrs	$n=8x10^{14}$	quartz crucible t~30μm
174	410-7.2 (111)	665°C 6.25hrs, 668°C 20 min, 15hrs to 340°C	$n=9.2x10^{14}$	t~23μm
175	410-7.2 (111)	400°C 2hrs vacuum, 665°C 4.5 hr H_2,15hr to 340°C	$n=5.6x10^{14}$	t~60μm
176	410-7.2 (111)	450°C 2.5hr vacuum, 665°C 5hr H_2, 15hr 340°C	$n=3.6x10^{14}$	t~65μm
177	410-7.2 (111)	665°C 6.5hr, 668°C 20 min, 15 hrs to 340°C	$n=1x10^{16}$	t~95μm
178	410-7.2 (111)	665°C 6.5hr, 668°C 20 min, 15 hrs to 340°C	$n=3.8x10^{15}$	t~48μm
179	410-7.2 (111)	665°C 5hr, 668°C 20 min, 15 hrs to 340°C	$n=4.4x10^{15}$	t~50μm
180	410-7.0 (111)	665°C 6hr, 668°C 20 min, 15 hrs to 340°C	$n=2.8x10^{14}$	t~55μm
181	410-7.0 (111)	665°C 6hr, 668°C 20 min, 15 hrs to 340°C	$n=2.4x10^{14}$	t~45μm

182	410-7.4 (111)	665°C 6.5hr, 668°C 20min,15hrs to 340°C	n=2.4x10^{14}	t~55μm
183	867-10.2 (111)	665°C 2.6hr, thermal cool to 400°C	N/A	doped substrate
184	410-7.4 (111)	665°C 6.5hr, 668°C 20min,15hrs to 340°C	n=1.4x10^{14}	45μm, Pb baked in H_2 then Ar
185	739-11.8 (111)	850°C 4hrs, 15hrs to 340°C	n=1x10^{14}	t~185μm
186	410-7.4 (111)	665°C 6.5hr, 668°C 20min,15hrs to 340°C	n=2.4x10^{14}	t~69μm
187	410-7.4 (111)	665°C 5hr, 668°C 20min,15hrs to 340°C	p=4x10^{16}	t~16μm contam. zone refined Pb
188	410-7.4 (111)	665°C 6.5hr, 668°C 20min,15hrs to 340°C	n=1.1x10^{16}	t~20μm
189	739-11.8 (111)	660°C 6.5hr, 663°C 20min,15hrs to 340°C	n=1.8x10^{15}	t~80μm
190	739-11.8 (111)	660°C 6.5hr, 663°C 20min,15hrs to 340°C	n=2.4x10^{14}	t~80μm
191	410-7.4 (111)	660°C 6.5hr, 663°C 20min,15hrs to 340°C	n=9.8x10^{14}	t~45μm
192	738-8.7 (111)	665°C 6.5hr, 668°C 20min,15hrs to 340°C	n=6x10^{15}	t~67μm
193	738-8.7 (111)	665°C 4.5hr, 668°C 20min,15hrs to 340°C	n=8x10^{17}	t~40μm, Sb dopant added
194	738-8.7 (111)	665°C 6hr, 668°C 20min,15hrs to 340°C	n=5.2x10^{16}	t~30μm, Sb dopant added
195	738-8.7 (111)	665°C 6hr, 668°C 20min,15hrs to 340°C	n=5.2x10^{16}	Sb dopant added
196	410-7.4 (111)	665°C 6.5hr, 668°C 20min,15hrs to 340°C	n=6.2x10^{14}	t~65μm
197	410-7.4 (111)	665°C 6hr, 668°C 20min,15hrs to 340°C	n=2.6x10^{14}	t~26μm
198	410-7.4 (111)	650°C 3hrs, thermal cool to 386°C 2.75 hrs	not meas.	
199	738-16.5 (111)	665°C 14hrs, 10hrs to 340°C	n=8x10^{14}	t~41μm
200	738-16.5 (111)	640°C 6 hrs. 642°C 10 min, 15hrs to 340°C	not meas.	t~50μm, Sb doped
201	738-16.5 (111)	640°C 6.5hrs, 642°C 10 min, 10 hrs to 340°C	n=1.3x10^{17}	t~50μm, Sb doped
202	738-16.5 (111)	615°C 6.5hrs, 618°C 10 min, 10 hrs to 340°C	n=1x10^{16}	t~30μm, Sb doped

203	738-16.5 (111)	615°C 6.5hrs, 618°C 10 min, 10 hrs to 340°C	$n=2.6x10^{16}$	t~18μm, Sb doped
204	410-7.4 (111)	660°C 6.5hr, 663°C 10min,10hrs to 340°C	$n=9x10^{14}$	t~27μm
205	410-7.2 (111)	660°C 6.5hr, 663°C 10min,10hrs to 340°C	$n=5.8x10^{14}$	t~30μm
206	410-7.2 (111)	660°C 6.5hr, 663°C 10min,10hrs to 340°C	$n=2.4x10^{14}$	t~30μm
207	410-7.6 (111)	660°C 7hr, 663°C 10min,10hrs to 340°C	$n=4x10^{14}$	t~38μm
208	410-7.0 (111)	660°C 6.5hr, 663°C 10min,12hrs to 340°C	$n=2.0x10^{14}$	t~37μm, Pb oxidized prev.
209	738-14.3 (111)	660°C 2hr, 600°C 5hr, 12hrs to 340°C	$n=8.2x10^{14}$	t~34μm
210	738-14.3 (111)	600°C 6.5hr, 603°C 20min,12hrs to 340°C	$n=1.2x10^{14}$	t~14μm
211	410-7.6 (111)	600°C 6.5hr, 603°C 20min,12hrs to 340°C	$n=1.4x10^{14}$	t~24μm
212	738-14.3 (111)	600°C 6.5hr, 603°C 20min,12hrs to 340°C	$n=1x10^{17}$	t~14μm, Sb doped
213	738-14.3 (111)	610°C 6.5hr, 613°C 20min,12hrs to 340°C	$n=5x10^{16}$	t~17μm, Sb doped
214	738-14.3 (111)	600°C 6.5hr, 603°C 20min,12hrs to 340°C	not meas.	
215	738-14.3 (111)	600°C 6.5hr, 603°C 20min,12hrs to 340°C	not meas.	substrate dissolved
216	739-11.8 (111)	660°C 6hrs, 12hrs to 340°C	HCl treated Pb	substrate $p=4.6x10^{11}$
217	739-11.8 (111)	660°C 6hrs, 12hrs to 340°C	not meas.	t~18μm
218	739-11.8 (111)	660°C 6hrs, 12hrs to 340°C	HNO_3 treated Pb	substrate $p=8.4x10^{11}$
219	738-14.3 (111)	660°C 6.5hr, 12hrs to 340°C	HCl treated Pb	substrate $n=1.4x10^{13}$
220	738-14.3 (111)	650°C 6.5hr, 12hrs to 340°C	not meas.	substrate dissolved
221	738-14.3 (111)	650°C 6.5hr, 12hrs to 340°C	$n=7.2x10^{15}$	t~46μm, Sb doped
222	738-14.4 (111)	650°C 6hrs, 12hrs to 340°C	$n=1.6x10^{16}$	t~36μm, Sb doped
223	738-14.4 (111)	650°C 6.5hr, 12hrs to 340°C	$n=4x10^{16}$	t~43μm, Sb doped

224	738-14.4 (111)	650°C 6.5hr, 12hrs to 340°C	n=5.2x10^{16}	t~30μm, Sb doped
225	738-14.4 (111)	650°C 6.5hr, 12hrs to 340°C	not meas.	t~6μm, tip late
226	738-14.4 (111)	650°C 6hrs, 12hrs to 340°C	n=5.4x10^{15}	t~45μm, Sb doped
227	738-14.4 (111)	650°C 6.5hr, 12hrs to 340°C	n=1.8x10^{16}	t~40μm, Sb doped
228	738-14.4 (111)	650°C 6.5hr, 12hrs to 340°C	n=7.4x10^{15}	t~32μm
229	738-14.4 (111)	650°C 6.5hr, 12hrs to 340°C	n=1x10^{16}	t~43μm, Sb doped
230	738-14.5 (111)	650°C 6.5hr, 12hrs to 340°C	n=3.8x10^{16}	t~48μm, Sb doped
231	738-14.5 (111)	650°C 6.5hr, 12hrs to 340°C	n=3.4x10^{16}	t~44μm, Sb doped
232	738-14.5 (111)	650°C 6.5hr, 12hrs to 340°C	n=2.2x10^{16}	t~44μm, Sb doped
233	738-14.5 (111)	650°C 6.5hr, 12hrs to 340°C	n=2.4x10^{16}	t~48μm, Sb doped
234	738-14.5 (111)	650°C 5.25hr, 12hrs to 340°C	n=1.2x10^{17}	t~66μm, Sb doped
235	738-14.5 (111)	650°C 7hrs, 12hrs to 340°C	n=1.4x10^{16}	t~44μm, Sb doped
236	738-14.5 (111)	650°C 6.5hr, 12hrs to 340°C	n=2.8x10^{16}	t~42μm, Sb doped
237	738-14.5 (111)	650°C 6.5hr, 12hrs to 340°C	n=1x10^{17}	t~60μm, Sb doped
238	738-14.5 (111)	650°C 6.25hr, 12hrs to 340°C	n=9.6x10^{15}	t~48μm, Sb doped
239	738-14.6 (111)	650°C 6.5hr, 12hrs to 340°C	n=1.2x10^{17}	t~42μm, Sb doped
240	738-14.6 (111)	650°C 6.5hr, 12hrs to 340°C	n=7.8x10^{15}	t~46μm, Sb doped
241	738-14.6 (111)	650°C 6.5hr, 12hrs to 340°C	n=2.2x10^{16}	t~42μm, Sb doped
242	738-14.6 (111)	650°C 6.5hr, 12hrs to 340°C	n=1x10^{17}	t~32μm, Sb doped
243	738-14.6 (111)	650°C 6.5hr, 12hrs to 340°C	n=4x10^{17}	t~65μm, Sb doped
244	738-14.6 (111)	650°C 6.5hr, 12hrs to 340°C	n=2.2x10^{16}	t~44μm, Sb doped

245	738-14.6 (111)	650°C 6.5hr, 12hrs to 340°C	$n=3.6x10^{16}$	t~60μm, Sb doped
246	738-14.6 (111)	650°C 6.5hr, 12hrs to 340°C	$n=7x10^{16}$	t~52μm, Sb doped
247	739-11.9 (111)	750°C 5.5hr, 1hr 550°C 12hrs to 340°C	$n=8x10^{15}$	t~24μm
248	739-11.9 (111)	750°C 5.5hr, 1hr 550°C 12hrs to 340°C	$n=2.4x10^{14}$	t~28μm
249	739-11.9 (111)	750°C 5.5hr, 1hr 550°C 12hrs to 340°C	$n=4.0x10^{14}$	t~26μm
250	739-11.9 (111)	750°C 4.5hr, 1hr 550°C 12hrs to 340°C	$n=3x10^{14}$	t~39μm
251	739-11.9 (111)	750°C 5.5hr, 1hr 550°C 12hrs to 340°C	$n=3.8x10^{14}$	t~35μm
252	739-11.9 (111)	750°C 5.5hr, 1hr 550°C 12hrs to 340°C	$n=1.6x10^{14}$	t~36μm
253	739-11.9 (111)	825°C 5.5hr, 1hr 550°C 12hrs to 340°C	$n=4.8x10^{13}$	t~19μm
254	410-7.6 (111)	825°C 5.5hr, 1hr 550°C 12hrs to 340°C	$n=1x10^{14}$	t~20μm
255	410-7.6 (111)	695°C 6hrs, 12hrs to 340°C	$n=4.5x10^{15}$	t~55μm
256	410-7.6 (111)	690°C 6hrs, 12hrs to 340°C	$n=6.2x10^{15}$	t~55μm
257	410-6.5 (111)	650°C 6hrs, 12hrs to 340°C	$n=1.8x10^{13}$	t~26μm
258	410-6.5 (111)	650°C 6.5hrs, 12hrs to 340°C	$p=6x10^{13}$	t~20μm
259	410-6.5 (111)	700°C 6hrs, 12hrs to 340°C	$n=6x10^{13}$	t~32μm
260	410-6.5 (111)	700°C 6hrs, 12hrs to 340°C	$n=1x10^{14}$	t~18μm
261	867-10.2 (111)	650°C 5.5hrs thermal cool to 340°C	N/A	t~15μm, doped substrate
262	867-10.2 (111)	650°C 5.5hrs thermal cool to 340°C	N/A	t~13μm, doped substrate
263	410-6.5 (111)	725°C 6hrs, 12 hrs to 340°C	$n=4.2x10^{13}$	t~41μm
264	410-6.5 (111)	750°C 6hrs, 12 hrs to 340°C	$n=4.6x10^{13}$	t~50μm
265	410-6.5 (111)	700°C 6hrs, 12 hrs to 340°C	$n=9.6x10^{13}$	t~30μm

266	410-6.5 (111)	700°C 6hrs, 12 hrs to 340°C	$n=1.1x10^{14}$	t~25μm
267	410-6.5 (111)	750°C 6hrs, 12 hrs to 340°C	$n=7x10^{14}$	t~55μm
268	410-6.5 (111)	665°C 6hrs, 12 hrs to 340°C	$n=7.6x10^{13}$	t~40μm
269	410-6.5 (111)	750°C 6hrs, 12 hrs to 340°C	not meas.	dissolved substrate
270	410-6.5 (111)	650°C 6hrs, 12 hrs to 340°C	$n=1.7x10^{14}$	t~32μm
271	410-6.5 (111)	675°C 6hrs, 12 hrs to 340°C	$n=1.4x10^{14}$	t~52μm
272	739-11.9 (111)	675°C 6hrs, 12 hrs to 340°C	$n=1.2x10^{14}$	t~30μm
273	739-11.9 (111)	675°C 6hrs, 12 hrs to 340°C	$n=9.2x10^{13}$	t~22μm
274	739-11.9 (111)	675°C 6hrs, 12 hrs to 340°C	not meas.	dissolved substrate
275	739-11.9 (111)	675°C 7hrs, 12 hrs to 340°C	$p=5x10^{13}$	t~20μm
276	739-11.9 (111)	675°C 6hrs, 12 hrs to 340°C	$n=5x10^{13}$	t~17μm

Appendix E: Spectral Response and Responsivity Measurements

Ge BIB detector measurement were performed in a Infrared Labs HD-3 Helium[15] dewar on a cold stage that can be adjusted from 4.2 K to 1.3 K by pumping on the liquid He reservoir, thus reducing the vapor pressure which lowers the boiling point of the liquid helium. Ge BIB detectors were mounted on sapphire wafers for electrical insulation. The sapphire was attached to a brass cold finger that was electrically isolated from the copper cold plate by a thin Kapton foil.

I-V measurements were performed by applying a bias voltage to the detector and measuring the current via the voltage drop over a feedback resistor of approximately 10^{10} Ω. The range of the detector current which can be measured lies between 10^{-9} and 10^{-14} A with the 10^{10} Ω feedback resistor. A schematic of the transimpedance amplifier circuit with a matching pair of cold JFETs in Fig. D1. The external operational amplifier OP07 is used for its low offset. A shutter in the IR Labs dewar allows the device to be shielded from all external radiation. With the shutter closed, the detector is surrounded only by the liquid helium blackbody radiation.

For spectral response measurements, Ge BIB detectors were exposed to far infrared radiation through a cold 8 mil black polyethelyene filter. For responsivity, signal to noise, and NEP measurements, a second filter was added. Detectors were exposed through a notch filter centered at 111 cm^{-1} with a width of 15 cm^{-1} with a transmission of 2%. The AC infrared signal was generated by chopping between blackbodies of 300 K and 77 K. This results in a peak to peak signal of 10^8 photons per second impacting a 1

[15] Model HD-3 Infrared Laboratories, Inc., Tucson, AZ.

mm^2 detector. These calculations are based on diffraction limited conditions of the optical geometry of the IR labs dewar. The calculation takes into account the distance between the various apertures, the distance from the detector to the final cold aperture, the cold aperture size, the narrow band filter's transmission, the filter bandwidth, and the absorbing area of the detector.

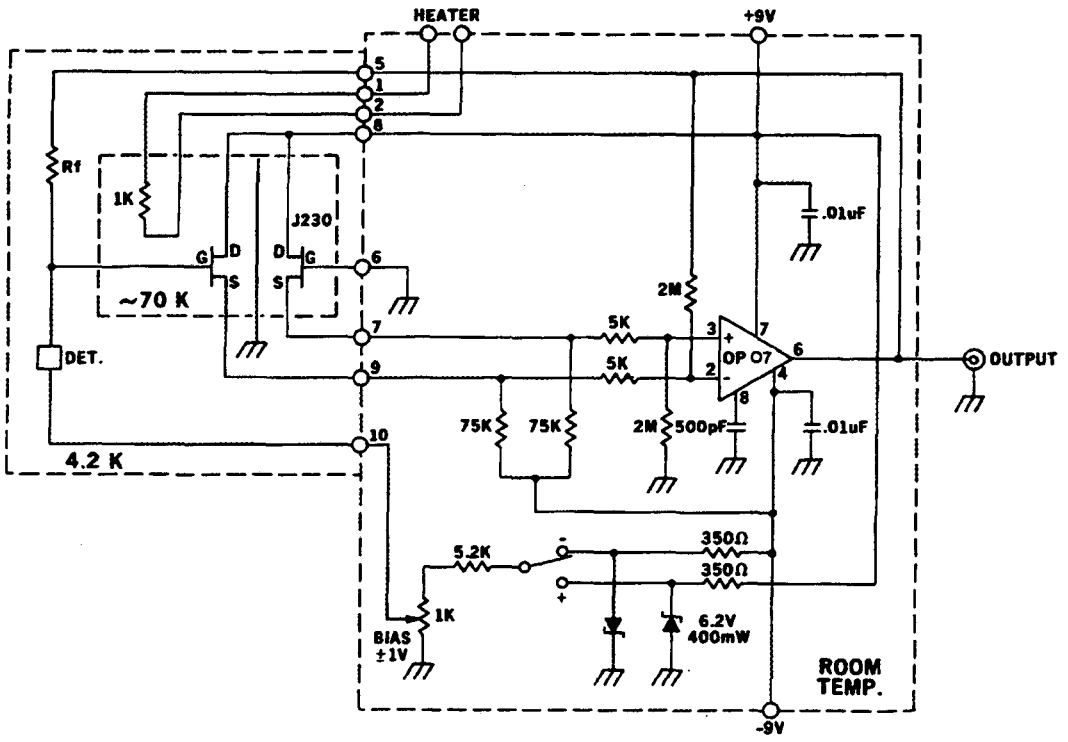

Fig. E1. Schematic of Transimpedance Amplifier.

Appendix F: N-type Alloy Contact

To facilitate Ge BIB detector production, a thin film alloy contact to n-type Ge was developed. This alloying process used the Ge-Au eutectic at 361°C to dissolve Ge into the liquid Au thin film while incorporating a dopant in the reaction. As the sample cools, the Ge regrows incorporating with the chosen dopant, Sb in this case. Pd is used to lower the surface tension, such that Au wets the Ge surface.

Ge crystal #831 Sb doped to $2x10^{14}$ cm^{-3} was used for testing the contact scheme. A wafer 1 mm thick, 8 mm wide and 13 mm long was dipped in 5% HF for 30 seconds, rinsed with distilled H_2O, and dried with N_2. It was loaded into the e-beam evaporator and pumped to $3x10^{-6}$ torr. The metal layers were evaporated in the following sequence: 10 nm Pd, 10 nm Sb, and 200 nm Au. The metal was evaporated onto 4 mm by 8 mm pads with a 5 mm clear space between the pads.(Figure F1)

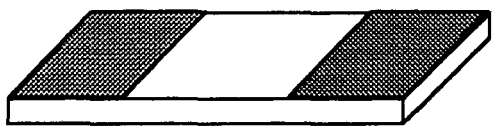

Fig. F1. Sketch of measurement geometry.

Three separate samples were prepared and annealed in the rapid thermal annealing (RTA) oven at 300°C, 380°C, and 420°C for 30 seconds to react the metals with the Ge. The samples annealed at 380°C and 420°C displayed a morphology change indicative of heating to above the eutectic temperature.

Each of the three samples was shielded from light by aluminized mylar, immersed into a liquid He dewar and the resistance between contacts was measured. The alloyed

contacts worked on all three of the samples and their resistance values are summarized in Table F1.

Annealing temperature	Resistance (GΩ)
300°C	2
380°C	0.3
420°C	0.2

Table F1. Resistance values between Pb-Sb-Au alloyed contacts at 4.2 K.

A photoconductive detector was fabricated from the same material and tested for signal and noise levels at 111 cm^{-1} under low background conditions. At 2.0 K, the detector was at the bottom of the noise floor at 2 $\mu V/Hz^{1/2}$ and displayed a signal to noise ratio of 10^3. This performance can only be achieved with excellent Ohmic contacts.

Appendix G: Electric Field in a BIB Detector

The electric field of a reverse biased BIB detector can be calculated using Poisson's equation for the voltage drop across the depletion region and the blocking layer.

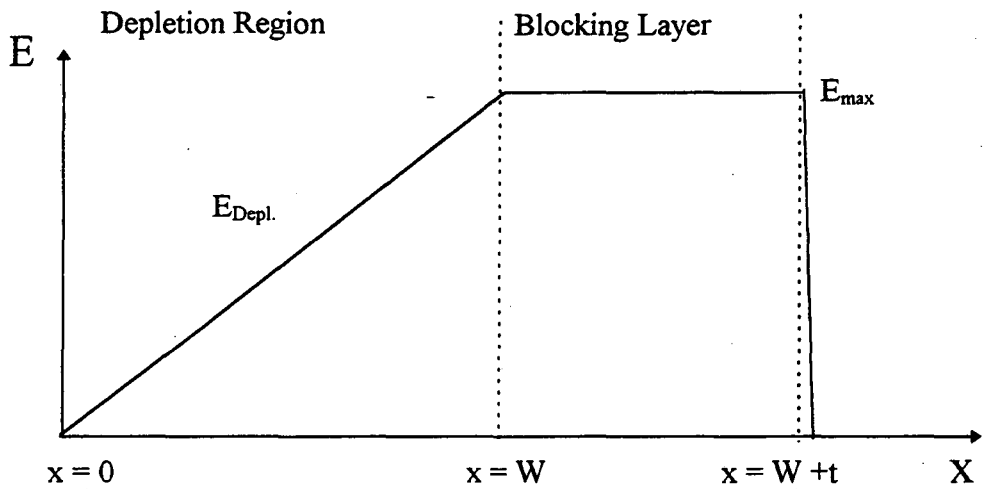

Fig. G1. Electric Field versus position through the BIB device.

The blocking layer has a constant electric field, E_{max}. $E_{Depl.}$ is the electric field in the depletion region at position x (cm), t is the blocking layer thickness, and V_a is the applied voltage. V_{bi} is the built-in voltage. It is the diffusion potential due to the difference in doping of the blocking layer and IR absorbing layer. To solve relationship G1, we use $E_{Depl.} = E_{max}$ when x = W.

$$E_{\max}t + \int_0^W \left(\frac{E_{\max}}{W}\right) x dx = V_a - V_{bi} \qquad \text{(G1)}$$

$$E_{\max}t + \frac{E_{\max}W}{2} = V_a - V_{bi} \qquad \text{(G2)}$$

This allows us to calculate the electric field in the blocking layer.

$$E_{\max} = \frac{V_a - V_{bi}}{t + \frac{W}{2}} \tag{G3}$$

Electric breakdown in a BIB detector is due to the large electric field in the blocking layer, so low doping in the blocking layer is of the utmost importance.

Again using Poisson's equation for E field and space charge, E_{max} can be determined in terms of the space charge N_a present in the IR absorbing layer due to minority dopants.

$$E_{\max} = \frac{eN_a W}{\varepsilon\varepsilon_o} \tag{G4}$$

By eliminating E_{max} and solving for W, we achieve equation 1.15 given by Petroff and Stapelbroek.

$$\frac{1}{2}W^2 + tW - \frac{(V_a - V_{bi})\varepsilon\varepsilon_o}{eN_a} = 0 \tag{G5}$$

$$W = \sqrt{\left[\frac{2\varepsilon\varepsilon_o(V_a - V_{bi})}{eN_a} + t^2\right]} - t \tag{1.15}$$

7. References

S. Ashtakala, A.D. Pelton, and C.W. Bale, *Bull. Alloy Phase Diagrams* **2**(1), (1981).

M.G. Astles, *Liquid Phase Epitaxial Growth of III-V Semiconductor Materials and Their Device Applications*, (IOP Publishing Ltd., Bristol, 1990).

I. Balslev, *Phys. Rev.* **143**, 636 (1966).

E. Bauser and H.P. Strunk, *J. Crys. Growth* **69**, 561 (1984).

E. Bauser in *Crys. Growth of Electronic Materials*, edited by E. Kaldis, (No.-Holland Physics Publ., Amsterdam, 1985).

E. Bauser in *Handbook of Crys. Growth*, edited by D.T.J. Hurle, (Elservier Science, Amsterdam 1994), p. 880.

J.W. Beeman and E.E. Haller, *Infrared Physics* **35**, 827 (1994).

J.W. Beeman, W.L. Hansen, O.D. Dubon, and E.E. Haller, *Infrared Physics* **37**, 715 (1996).

A.C. Beer and R.K. Willardson, *Phys. Rev.* **110**, 1286 (1958).

A.C. Beer, in *The Hall Effect and its Applications,* C.L. Chien and C.R. Westgate, Eds. (Plenum Press, New York, 1980), p. 229.

R.J. Bell, *Introductory Fourier Transform Spectroscopy* (Academic Press, New York, 1972).

J.S. Blakemore, *Semiconductor Statistics*, (Dover Publications, New York, 1987).

P.R. Bratt, in *Semiconductors and Semimetals*, edited by R.K. Willardson and A.C. Beer (Academic Press, New York, 1977), p. 39.

J.A. Burton, R.C. Prim, and W.P. Slichter, *J. Chem. Phys.* **21**, 1987 (1953).

B.D. Culity, *Elements of X-ray Diffraction*, (Addison-Wesley, Reading, MA, 1978), p. 510.

J. Czochralski, *Z. Phys. Chemie* **92**, 219 (1918).

P.P. Debye and E.M. Conwell, *Phys. Rev.* **93**, 693 (1954).

A. Dommann, N. Herres, H.R. Deller, H.U. Nissen, D. Kruger, R.E. Pixley, and J. Ramm, *J. Phys. D.* **28**, A144 (1995).

N.M. Haegel. *Performance and Materials Aspects of Ge:Be and Ge:Ga Photoconductors for Far Infrared Detection* (M.S. thesis UCB, 1983 unpublished; LBL report #16694).

N.M. Haegel, private communication (1997).

E.H. Hall, *Amer. J. Maths.* **2**, 287 (1879).

R.N. Hall and J.H. Racette, *J. Appl. Phys.* **35**, 379 (1964).

R.N. Hall, *Proc. IRE* **40** (11), 1512 (1952).

E.E. Haller, *Infrared Physics* **25**, 257 (1985).

E.E. Haller and W.L. Hansen, *IEEE Trans. Nucl. Sci.* **NS-21**, No. 1, 279 (1974a).

E.E. Haller and W.L. Hansen, *Solid State Comm.* **15**, 687 (1974b).

E.E. Haller, W.L. Hansen, and F. Goulding *IEEE Trans. Nucl. Sci.* **NS-22**, No. 1, 127 (1975).

E.E. Haller, M.R. Hueschen, and P.L. Richards, *Appl. Phys. Lett.* **34**, 495 (1979).

P.J. Holmes, *The Electrochemistry of Semiconductors* (Academic Press, London, 1962), p. 370.

J.J. Hsieh, *J. Crys. Growth* **27**, 49 (1974).

J.E. Huffman, A.G. Crouse, B.L. Halleck, T.V. Downes, and T.L. Herter, *J. Appl. Phys.* **72**, 273 (1992).

A. Immorlica and B. Ludington, *J. Crys. Growth.* **51**, 131 (1981).

H.F. John, *J. Electrochem. Soc.* **105**, 741 (1958).

J.M. Kahn, *Hydrogen-Related Acceptor Complexes in Germanium* (Ph.D. thesis UCB, 1986 unpublished; LBL report #22652).

P.H. Keck and J. Broder, *Phys. Rev.* **90**, 521 (1953).

K. Kijima, N. Miyamoto, and J. Nishizawa, *J. Appl. Phys.* **42**, 486 (1970).

W.B. Knowlton, *Structural and Phonon Transmission Study of Ge-Au-Ge Eutectically Bonded Interfaces* (M.S. thesis UCB, 1995 unpublished; LBL report #37582).

K. Konuma, E. Czech, I. Silier, and E. Bauser, *Appl. Phys. Lett.* **63,** 205 (1993).

E.A. Kraut and W.A. Harrison, *J. Vac. Sci Technol.* **B3** (4), 1267 (1985).

K. Kumar and M. Tagaki, *Japan J. Appl. Phys.* **16**, 957 (1977).

A. Lawley, "Zone Refining," *Techniques of Materials Preparation & Handling*, (Interscience Publishers, New York, 1968), p. 845.

T.M. Lifshits and F. Ya Nad', *Sov. Phys. - Dokl.* **10**, 532 (1965).

T.M. Lifshits, N.P. Likhtman and V.I. Sidorov, *Sov. Phys.-J.Exper.Theor. Phys. Letter* 7, 2076 (1968).

M.P. Lutz, *Development of Ultra Pure Germanium Epi Layers for Blocked Impurity Band Far Infrared Detectors* (Ph.D. thesis UCB, 1991 unpublished, LBL report #30822).

N.F. Mott and W.D. Twose, *Advances in Physics* **10**, 111 (1971).

M.I. Nathan, W. Paul, and H. Brooks, *Phys. Rev.* **124**, 391 (1961).

H. Nelson, *RCA Review* **24**, 603 (1963).

A.N. Nesmeianov, *Vapor Pressure of the Chemical Elements* (Elsevier, Amsterdam, 1963).

R.W. Olesinski and G.J. Abbaschian, *Bull. Alloy Phase Diagrams* **5**, No.4 (1984).

C.S. Olsen, *Advanced Far Infrared Detectors and Double Donor Studies in Ge*, (M.S. Thesis UCB, 1994 unpublished; LBL report #36619).

S. Pasquier, G. Sirman, C. Meny, A. Murray, M. Griffin, P. Ade, L. Essalch, J. Galibert, and J. Leotin, *Proc. SPIE* **2211**, 634 (1994).

L.J. van der Pauw, *Philips Res. Rep.* **13**, 1 (1958).

M.D. Petroff and M.G. Stapelbroek, unpublished report, IRIS Specialty Group on IR Detectors (1984).

M.D. Petroff and M.G. Stapelbroek, unpublished report, IRIS Specialty Group on IR Detectors (1985).

G. Pilbratt, *Infrared Physics* **35**, 407 (1994).

E.H. Putley, *The Hall Effect and Related Phenomena* (Butterworths, London, 1960).

Lord Rayleigh, *Scientific Papers*, **6** (Cambridge Univ. Press, Cambridge, 1916), p. 432.

J.H. Reuszer and P. Fisher, *Phys. Rev.* **135**, A1125 (1964).

D.B. Reynolds, D.H. Seib, S.B. Stetson, and T. Herter, *IEEE Trans. Nucl. Sci.* **NS-36**, 857 (1992).

G.H. Rieke, M.W. Werner, R.I. Thompson, E.F. Becklin, W.F. Hoffman, J.R. Houck, F.J. Low, W.A. Stein, and F.C. Witteborn, *Science* **231**, 807 (1986).

F. Rosenberger and H.G. Riveros, *J. Chem. Phys.* **60**, 668 (1974).

C.S.Rossington, *Germanium Blocked Impurity Band Far Infrared Detectors,* (Ph.D. thesis UCB, 1988 unpublished; LBL report #25394).

A.K. Roy and R.P. Chahabra, in *CRC Handbook of Chemistry and Physics*, edited by D.R. Lide (Boca Raton, CRC Press 1995), p. 6-207.

R.H. Saul and D.D. Roccasecca, *J. Electrochem. Soc.* **20**, 1128 (1973).

N. Sclar, E. Burstein, W.J. Turner, and J.W. Davisson, *Phys. Rev.* **91**, 215 (1953).

N. Sclar, *Infrared Physics* **16**, 435 (1976).

B.I. Shklovskii and A.L. Efros, *Electronic Properties of Doped Semiconductors* (Springer-Verlag, Berlin, 1984).

W.G. Spitzer, F.A. Trumbore, and R.A. Logan, *J. Appl. Phys.* **32** 1822 (1961).

G.E. Stillman C.M. Wolfe, and J.O. Dimmock, in *Semiconductors and Semimetals*, edited by R.K. Willardson and A.C. Beer (Academic Press, New York, 1977), p. 169.

C.D. Thurmond and M. Kowalchik, *Bell Syst. Tech. J.* **39**, 169 (1960).

C.D. Thurmond and R.A. Logan, *J. Phys. Chem.* **60**, 591 (1956).

W.A. Tiller, *J. Crys. Growth* **2**, 69 (1967).

F.A. Trumbore, *J. Electrochem. Soc.* **103**, 597 (1956).

F.A. Trumbore, *Bell Sys. Tech. J.* **39**, 205 (1960).

W.W. Tyler, *J. Phys. Chem. Solids* **8**, 59 (1959).

I. Uschmann, E. Förster, K. Gäbel, G. Hölzer, and M. EnBlen, *J. Appl. Cryst.* **26**, 405 (1993).

K.M. van Vliet, *Appl. Opt.* **6**, 1145 (1967).

D.M Watson and J.E. Huffman, *Appl. Phys. Lett.* **52**, 1602 (1988).

I.C. Wu, J.W. Beeman, P.N. Luke, W.L. Hansen, and E.E. Haller, *Appl. Phys. Lett.* **58**, 153 (1991).

I.C. Wu, *Far-Infrared Germanium Photodetectors by Ion Implantation* (Ph.D. thesis UCB, 1993 unpublished).

D.I. Wynne, *Liquid Phase Epitaxial Growth of GaAs,* (M.S. thesis UCB, 1997 unpublished; LBL report #40929)

A. van der Ziel, *Fluctuation Phenomena in Semiconductors,* (Academic Press, New York 1959).

Ernest Orlando Lawrence Berkeley National Laboratory
One Cyclotron Road | Berkeley, California 94720

Prepared for the U.S. Department of Energy under Contract No. DE-AC03-76SF00098